

NORTHWESTERN UNIVERSITY

**Development and Validation of a Liquid
Composite Molding Model.**

A DISSERTATION

SUBMITTED TO THE GRADUATE SCHOOL
IN PARTIAL FULFILLMENT OF THE REQUIREMENTS

for the degree

DOCTOR OF PHILOSOPHY

Field of Theoretical and Applied Mechanics

By

John Michael Bayldon

EVANSTON, ILLINOIS
June 2007

© Copyright by John Michael Bayldon 2007
All Rights Reserved

ABSTRACT

Development and Validation of a Liquid Composite Molding Model.

John Michael Bayldon

In composite manufacturing, Vacuum Assisted Resin Transfer Molding (VARTM) is becoming increasingly important as a cost effective manufacturing method of structural composites. In this process the dry preform (reinforcement) is placed on a rigid tool and covered by a flexible film to form an airtight vacuum bag. Liquid resin is drawn under vacuum through the preform inside the vacuum bag. Modeling of this process relies on a good understanding of closely coupled phenomena. The resin flow depends on the preform permeability, which in turn depends on the local fluid pressure and the preform compaction behavior.

VARTM models for predicting the flow rate in this process do exist, however, they are not able to properly predict the flow for all classes of reinforcement material. In this thesis, the continuity equation used in VARTM models is reexamined and a modified form proposed. In addition, the compaction behavior of the preform in both saturated and dry states is studied in detail and new models are proposed for the compaction behavior.

To assess the validity of the proposed models, the shadow moiré method was adapted and used to perform full field measurement of the preform thickness during infusion, in addition to the usual

measurements of flow front position. A new method was developed and evaluated for the analysis of the moiré data related to the VARTM process, however, the method has wider applicability to other full field thickness measurements.

The use of this measurement method demonstrated that although the new compaction models work well in the characterization tests, they do not properly describe all the preform features required for modeling the process. In particular the effect of varying saturation on the preform's behavior requires additional study.

The flow models developed did, however, improve the prediction of the flow rate for the more compliant preform material tested, and the experimental techniques have shown where additional test methods will be required to further improve the models.

ACKNOWLEDGMENTS

I would like to thank Professor IM Daniel for consistently steering me in the right direction, not despairing at the wrong paths I took, and helping me find my way back when I took them.

I would like to thank Dr JJ Luo, and Dr JM Cho for answering both important and ridiculous questions with equal patience.

I would like to thank my thesis committee, Professors, N Patankar, H Espinosa, and J Cao, for their advice and assistance.

The work described in this thesis was funded by the Office of Naval Research through Dr Ignacio Perez, and I am extremely grateful for the opportunity he provided for me to carry out this research on a topic I enjoy so much.

I am also grateful to Trevor Schenck, for although the experiments he carried out and the data he collected were not used in this thesis, he carried out a large number of preform compaction experiments for me during the Summer of 2005, and the data he collected helped shape the experiments which ultimately were used.

This thesis is dedicated to

Jane

Without Whom It Could Not Have Been Contemplated

Table of Contents

1	Introduction.....	17
1.1	Background.....	17
1.2	Objectives and Organization.....	18
1.3	Experimental Validation.....	19
2	The Vacuum Assisted Resin Transfer Molding (VARTM) Process	20
2.1	Origins.....	20
2.2	General Principles of the VARTM process	24
2.3	Darcy’s Law, Permeability and the Effect of Preform Compaction.....	25
2.3.1	Definition of Darcy Velocity	26
2.3.2	Effect of Compaction on Permeability	30
2.3.3	Measurement of Permeability.....	31
2.4	Areas of Model Development.....	32
2.5	Areas of Experimental Development.....	33
3	Preform Compaction.....	34
3.1	Introduction.....	34
3.2	Compaction Process Behavior	34
3.2.1	Model Development.....	37
3.3	The Compaction Process in VARTM.....	42
3.3.1	Reference State and Definition of Strain	42

3.3.2	Compaction Pressure	43
3.4	Proposed Model	45
3.4.1	Reloading from Partial Unloading.....	47
3.4.2	Unloading from Partial Loading.....	49
3.4.3	Effect of Saturation on Compaction in Dual Scale Preforms	50
3.4.4	The Effect of Varying Saturation on Behavior	50
4	Experimental Evaluation of Preform Compaction.....	52
4.1	Materials	52
4.2	Preliminary Evaluation of Basic Preform Parameters	52
4.2.1	Poisson's Ratio for Plain Weave Fabric under Transverse Compression.....	53
4.2.2	Effect of Lubricating Fluid on Preform Compaction.....	56
4.3	Experimental Evaluation of Proposed Compaction Model	60
4.3.1	Comparison with Experimental Results.....	63
4.3.2	Compaction Model Conclusions.....	72
5	Flow modeling	74
5.1	Background.....	74
5.2	Notation and Volume Averaging theorems	74
5.3	Definition of Volume Elements	75
5.3.1	Integral Averaging Theories	76
5.4	Mass Balance (Continuity)	79

	9
5.5	Macroscopic Momentum Equation..... 81
5.5.1	Final Form of Governing Equation..... 82
5.6	Sink Term Derivation 83
5.7	Computational Implementation 85
5.8	Discretization 87
5.8.1	1-D fixed mesh..... 87
5.8.2	Updating the Tow Saturation 90
5.8.3	Thickness Term..... 91
5.8.4	Non-Linearity..... 95
5.8.5	Time Step Calculation..... 96
5.9	Model Output 97
5.9.1	Convergence 97
5.9.2	Model Results 98
6	Experimental Methods 103
6.1	Shadow Moiré..... 103
6.1.1	Basic Moiré Theory 103
6.1.2	Takasaki/Meadows Geometry for Shadow Moiré 106
6.1.3	Phase Wrapped Images and Image Unwrapping 109
6.1.4	Single Image Unwrapping 115
6.1.5	Statistical Separation of Phases 117
6.1.6	Experimental Validation 119

6.1.7	Trial Data	122
6.1.8	Unwrapping VARTM data	124
6.1.9	Effectiveness of the Statistical Technique	125
6.2	Optical Measurement of Preform Saturation	126
6.2.1	Basic Model	127
6.2.2	Saturation	130
6.3	Saturation Measurements.....	131
6.4	Moiré Flow Experiments	132
6.4.1	Permeability model.....	133
6.5	Results.....	135
6.5.1	Plain Weave	135
6.5.2	Continuous Filament Mat	137
6.5.3	Thickness Change Discrepancy	138
7	Summary, Conclusions, and Recommendations for Future Work.....	140
7.1	Preform Compaction.....	140
7.2	VARTM Flow Modeling	140
7.2.1	Experimental Methods.....	141
7.3	Conclusions.....	141
7.4	Recommendations for Future Work.....	142
8	References.....	143

List of Tables

Table 1 Preform Compaction Stages	45
Table 2 Plain Weave Fabric Properties.....	52
Table 3 CFM Random Mat Properties.....	52
Table 4 Cross-Head Rates for Compaction of Continuous Filament Mat	62
Table 5 Parameters Used for Envelope Curves for Plain Weave	64
Table 6 Parameters Used for Envelope Curves for Continuous Filament Mat (CFM, OCF8610).....	66
Table 7 Possible Result Sets for Changes in Surface Height.....	118
Table 8 Data Used for Algorithm Evaluation Trials.....	122
Table 9 Permeability Constants for Carman-Kozeny Relationship.....	133

List of Figures

Figure 2-1 Diagram of Marco Composite Manufacturing Method (1960) [6].	20
Figure 2-2 Plain Weave Fabric and Continuous Filament (Random) Mat	22
Figure 2-3 Typical VARTM set-up	24
Figure 2-4 Basis of Flow Models for VARTM	26
Figure 3-1 Layer Nesting	35
Figure 3-4 Van Wyk Model Basis	38
Figure 3-5 Gutowski Compaction Model [16, 17].	39
Figure 3-7 Schematic of the Modified Loading and Reloading Model	48
Figure 3-8 Unloading after Partial Loading.	49
Figure 3-9 Saturation Behavior, Dry and Wet Showing Possible Transitional Behavior for Saturation while Unloading	51
Figure 4-1 Plain Weave Fabric under Compression, (a) Unloaded and (b) Compressed to Approximately 50% of the Original Thickness.	53
Figure 4-2 Load vs Volume Fraction for 99 Ply Columnar Stack of Plain Weave Glass Fabric .	54
Figure 4-3 Axial and Transverse Strains in Fabric Subject to Transverse Compression	55
Figure 4-4 In-Plane vs Through Thickness Strain under Through Thickness Compression for Plain Weave Fabrics	56
Figure 4-5 Flow Model for Compaction Tests	57
Figure 4-6 Effect of Compaction Speed on Measured Load	58

Figure 4-7 Plot of Preform Properties Parameter L against Thickness Parameter 59

Figure 4-8 Test Jig, Load Cell and Linear Voltage Displacement Transducer 61

Figure 4-9 Schematic of Partial Unloading and Partial Reloading Cycles..... 62

Figure 4-10 Loading and Unloading Envelopes for Dry Plain Weave (7500 style)..... 65

Figure 4-11 Loading and Unloading Envelopes for Wet Plain Weave (7500 style) 65

Figure 4-12 Loading and Unloading Envelopes for Unlubricated (dry) Continuous Filament Mat
..... 67

Figure 4-13 Loading and Unloading Envelopes for Lubricated (wet) Continuous Filament Mat 67

Figure 4-14 Behavior of Dry (Unlubricated) Plain Weave on Reloading after Partial Unloading68

Figure 4-15 Behavior of Wet(Lubricated) Plain Weave Fabric on Reloading from Partial
Unloading..... 69

Figure 4-16 Behavior of Dry (Unlubricated) Plain Weave on Unloading from Partial Loading . 69

Figure 4-17 Behavior of Dry (Unlubricated) Continuous Filament Mat on Reloading after Partial
Unloading..... 70

Figure 4-18 Behavior of Wet (Lubricated) Continuous Filament Mat on Reloading after Partial
Unloading..... 71

Figure 4-19 Behavior of Dry (Unlubricated) Continuous Filament Mat on Unloading after Partial
Loading 71

Figure 4-20 Behavior of Wet (Lubricated) Continuous Filament Mat on Unloading after Partial
Loading 72

Figure 4-21 Schematic of Unloading Curves for Unloading from 1atm and 5atm Compaction.. 73

Figure 5-1 Multi-Scale Structure of Unit Cell.....	75
Figure 5-3 RVE Sub-element Notation.....	77
Figure 5-4 Tow Infiltration Model.....	84
Figure 5-5 Node Line Terminology [45]	86
Figure 5-6 1-D Static Element	87
Figure 5-7 Convergence Plot Showing Error in Flow Time against Element Size	98
Figure 5-8 Pressure Profiles for Resin Flow in Plain Weave Fabric	99
Figure 5-9 Pressure Profiles for Flow in Continuous Filament Mat.....	99
Figure 5-10 Thickness Profiles Showing Saturation Effect in Plain Weave	100
Figure 5-11 Model Flow Front Position Results For Plain Weave.....	101
Figure 5-12 Model Flow Front Positions for Continuous Filament Mat.....	102
Figure 6-2 Moiré Images of 16 ply Plain Weave (left) and 4 Ply CFM (right) using 100 lines/inch Grating	104
Figure 6-3 Shadow Moiré Image of Calibration wedge	105
Figure 6-4 General Geometry for Shadow Moiré.....	107
Figure 6-5 Filtered Image of Wedge with Low Frequency Variation Removed.....	111
Figure 6-6 Intensity Plots Along Wedge Steps.....	111
Figure 6-7 Phase Wrapped Height Map of Step Wedge.....	112
Figure 6-8 Unwrapped Lines from the Phase Wrapped Step Wedge Dataset	113
Figure 6-9 Intensity Image and Phase Wrapped Image of Segment of CFM Material	114

Figure 6-10 Surface Profile of Continuous Filament Mat Generated using Ghiglia Algorithm [59]..... 114

Figure 6-11 Functions of Surface Height w Used in Shadow Moiré Analysis..... 115

Figure 6-12 Histogram of Data Points from a Shadow Moiré Image of a Region of a VARTM Process (Probability density function shown as smooth black curve)..... 119

Figure 6-13 Shadow Moiré Setup for Recording Surface Morphology During VARTM Process 120

Figure 6-14 Images Showing Effect of Added Noise to Fringe Patterns Generated from a Simulated Spherical Surface..... 123

Figure 6-15 Error in Calculated \mathcal{Z} along a Sample Line..... 123

Figure 6-16 Variation in Measurement Error as a Function of Noise 124

Figure 6-17 Moiré Images of Continuous Filament Mat(a) and Plain Weave Fabric(b)..... 124

Figure 6-18 Plot of Measured Thickness Change in Preform during VARTM Processing 125

Figure 6-19 Schematic of Light Path through Fiber Preform..... 127

Figure 6-20 Light Attenuation vs Areal Weight of Glass Fibers in Preform 129

Figure 6-22 Saturation Measurements on Plain Weave Glass..... 131

Figure 6-23 Permeability vs Fiber Volume Fraction (reproduced by permission J Opperer[66]) 134

Figure 6-24 Carman-Kozeny Equation Fit for CFM (OCF8610)..... 134

Figure 6-25 Location of Flow Front as a Function of Time Predicted by Using Various Thickness Models, and Measured Experimentally for Plain Weave Glass 136

Figure 6-26 Location of Flow Front as a Function of Time Predicted by Using Various Thickness Models, and Measured Experimentally for Continuous Filament Mat	137
Figure 6-27 Comparison of Thickness Changes to Model Plain Weave	138
Figure 6-28 Thickness Profiles at Various Times During Infusion of Continuous Filament Mat, Measured by Shadow Moiré.	139

1 Introduction

1.1 Background

The structural components of most biological systems are composite; bone in vertebrate animals, wood and softer structures in plants, even the exoskeleton materials and shells of invertebrates. Humans have manufactured composite materials from natural fibers using matrices of available materials since prehistoric times [1, 2]. Since the development of man-made fibers and resins composite materials have been used in increasingly highly stressed and critical structures, and high quality composites are now common in applications ranging from sports through to defense aircraft. The high costs associated with these high performance composites have steadily reduced, as increased production volumes have lead to lower prices for the raw fibers and resins, and manufacturing technologies have evolved to reduce the dependence on highly skilled manual labor. Some of the processes now being applied to the most critical structures in aerospace have evolved from fairly crude processes where the operator's skill was sufficient to ensure adequate quality. This simple approach, while entirely sufficient for parts which are low cost and which will not be critical to a primary structure, is insufficient for the engineering of more critical or expensive structures.

One important class of processes for composite manufacture is liquid composite molding (LCM). These processes involve infiltrating a dry fiber preform, placed on a mold, with a liquid resin, and then curing the resin. Resin Transfer Molding (RTM) has already developed as a high quality manufacturing system during the 1980s and significant efforts were made to understand and model

the process [3]. An important development of this process, Vacuum Assisted Resin Transfer Molding (VARTM), which is described in detail in Chapter 2, is now being applied to aircraft and other high quality structures, and therefore there is an increased interest in modeling this process. This thesis proposes several significant improvements in the modeling of the VARTM process, and in the methods which can be used for experimental validation of such models.

1.2 Objectives and Organization

The primary aim of this thesis is to show that proper modeling of the VARTM process requires a thorough understanding of the process of preform deformation under compressive loading, together with a model which directly includes this deformation process. In Chapter 2 the process is described along with the basic transport phenomena required to develop a flow model for the process. Chapter 3 discusses the current state of the art in modeling preform compaction, and proposes a new model for preform compaction, especially for the compaction of the preform from intermediate loading states, and the effect of preform saturation on the compaction behavior. Chapter 4 describes a set of experimental tests which were used to characterize the preform used in the thesis and to validate the model proposed in Chapter 3. Chapter 5 discusses the governing equations for the flow model, and the control volume finite element method used in modeling the VARTM behavior. In Chapter 5 a volume average continuum mechanics model originally proposed by Pillai [4] for RTM is extended to cover the unique aspects of VARTM, and in the extended form becomes a more general description applicable to all LCM processing methods. Chapter 6 describes the experimental methods developed in the course of the thesis to allow full field measurements of the preform thickness during processing using a shadow moiré method, and

to measure the preform saturation using a transmitted light method. Chapter 7 then compares the experimental results for two preform materials with the model variations discussed in Chapter 5.

1.3 Experimental Validation

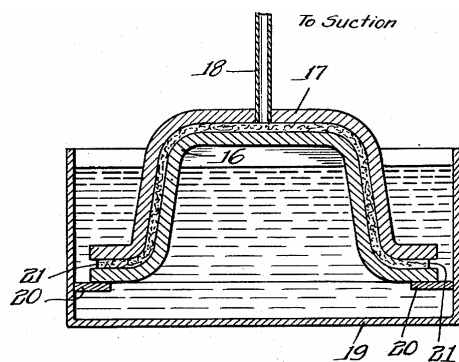
An important feature of this thesis is the time and effort devoted to attempting to validate the flow models experimentally. Process models have two main purposes, to predict the behavior of a process during manufacture, and to develop insight into the relative importance of process parameters and thereby develop more efficient processes. For either purpose to be fulfilled it is essential to adequately validate the behaviors predicted by the models. In VARTM, validation to date has largely been a matter of measurement of flow front shapes. This works adequately when the processes modeled are relatively simple, but as the shapes become more complex, and as additional materials such as sandwich cores are introduced to the process, it is essential to understand how the preform is deforming during the actual process. As part of the work, a shadow moiré machine and associated control software was designed and built. In this thesis a simple flow shape is used for both modeling and validation. However, considerable complexity is introduced by the variation in preform thickness during resin infusion, and the experimental measurement of this thickness variation is unique, and required the development of new methods of data analysis for the shadow moiré measurement system.

2 The Vacuum Assisted Resin Transfer Molding (VARTM) Process

2.1 Origins

The VARTM process is a liquid composite molding process, in which a liquid resin is drawn through a reinforcement preform using only vacuum pressure, with one or more of the preform surfaces constrained by a flexible membrane (rather than a solid tool). There are numerous variations on the process, some proprietary, and most with their own acronyms, e.g., SCRIMP (Seeman Composites Resin Infusion Manufacturing Process), RIFT (Resin Infusion under Flexible Tooling), VARI (Vacuum Assisted Resin Infusion), etc. Recent convention has been to classify all these as forms of VARTM.

Williams [5] provides an excellent historical review of the development of the VARTM process, from the Marco methods in 1950 through 1996 (the publication date). The Marco method [6] used a thin but rigid tool, and drew resin through the dry glass fiber mat between the plug and tool using vacuum (see Figure 2-1).



KEY

- 16 Male mold
- 17 Female mold
- 18 Vacuum Tube
- 19 Resin tank
- 20 Mold support
- 21 Open end of the mold

Figure 2-1 Diagram of Marco Composite Manufacturing Method (1960) [6].

In the Marco method, the resin was initially held in a trough which was built as a part of the male plug, or in a submerged basin. The main difference between the modern VARTM method and the original Marco method is the use of a flexible tool on at least one side of the reinforcement.

In the late 1990s the process was gaining popularity for the fabrication of marine structures for two main reasons; reduction of volatile emissions from the resins, and improvements in resins and reinforcements which allow high volume fraction and low void content parts to be made using this method.

The reduction in resin emissions was driven largely by occupational health and safety concerns. Much of the composite industry (in particular manufacturers of non-structural and low volume fraction composites) used open mold technologies, such as hand lay-up and spray molding methods. The resins typically used were polyesters, vinyl esters, and acrylics, all of which release solvents into the workplace. Of particular concern was styrene, and although the US exposure limit remains at 100ppm (8 hour time weighted average) [7], in parts of Europe the regulatory exposure limits are now as low as 20ppm. During the 1990s significant efforts were made to reduce the levels of occupational exposure to styrene in composite manufacturing facilities, including the use of specialized resins, and there was a move to more closed mold techniques, such as resin transfer molding, and press molding. VARTM allows manufacturers to move away from hand lay-up methods at low cost. VARTM also improves the fiber volume fraction of the final composites, allows containment of the resin, significantly reducing workplace exposure, and

allows low cost single sided molds to be used. In many cases the original hand lay-up tools can still be used.

The other major driver for the introduction of the process was the development of new types of reinforcements such as warp knit fabrics. Most composites had been manufactured using unidirectional pre-preg tapes for high quality structures such as aircraft components, woven fabrics (either as dry fabric or pre-impregnated with resin) for medium quality structures (lower stressed aircraft applications and higher stressed marine applications), and random fibers (continuous filament mat CFM and chopped strand mat CSM) for lower quality structures such as interior panels for trains. Figure 2-2 shows two of these fabric types.

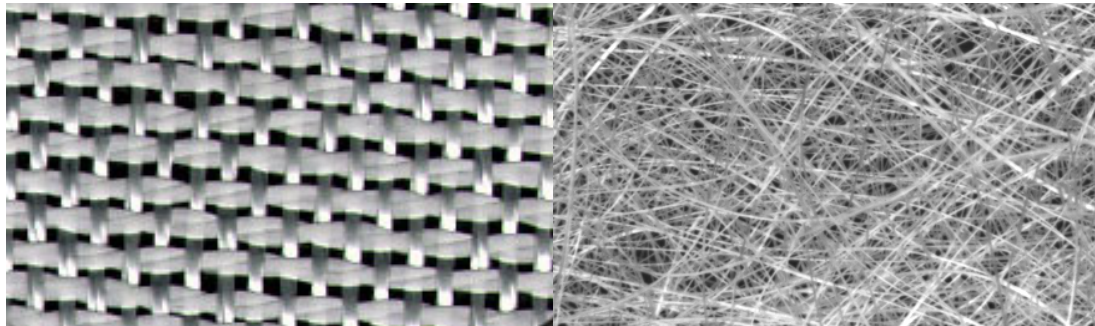


Figure 2-2 Plain Weave Fabric and Continuous Filament (Random) Mat

Warp knit or multi-axial fabrics consist of layers of tows (bundles of aligned fibers), stitched together into a fabric. This allows thick fabrics to be created, without the associated tow crimping (or waviness) of woven fabrics. These fabrics reduce manufacturing time and allow for increased reinforcement volume fraction with the available compaction pressure of VARTM (1 atmosphere or 101KPa).

In 1988 Seeman Composites applied for a US patent [8] on a variation of the vacuum infusion method, which involves the use of a disposable distribution layer placed over the reinforcement material. This innovation allows resin to flow rapidly across the whole surface of the reinforcement before wetting through the reinforcement thickness. Although the related patents were not granted internationally, the Seeman Composites Resin Infusion Manufacturing Process (SCRIMP) became the most common method for VARTM style manufacture, and several large composite structures were made using the process, including yacht hulls and some military naval vessels [9].

In the 1990s most VARTM applications were performed without recourse to models. Although the final part thickness was variable, the improvements in final material properties compared to the processes being replaced (typically hand lay-up) were substantial enough that high levels of optimization were generally not sought. In addition, the standards for structural certification in the marine industry where these processes were being applied are less demanding than for aerospace components. The quality of parts being produced using VARTM attracted the interest of the aerospace community during the late 1990s, in Europe focusing on the airbus A380 aircraft and in the US on the Boeing 787. The certification requirements for structural airframe components have led to a much higher demand for modeling of the VARTM process. Aerospace certification requirements limit some of the freedoms available in less strictly regulated industries, and the preforms which may be used are more complex in shape and frequently more expensive. Control of the infusion process is therefore more important and careful modeling allows processes with more consistent results to be designed. All these factors have led to an increased interest in modeling of the VARTM process.

2.2 General Principles of the VARTM process

In the VARTM process, reinforcement materials, often referred to as preforms, are infused with a resin by drawing the resin through the reinforcement under vacuum. The vacuum also serves to consolidate the reinforcement materials which are typically compliant in the through thickness direction. Additional materials may be included in the composite, e.g., core materials for sandwich type panels, and fasteners for attachments. Figure 2-3 shows a typical set up for the manufacture of a simple flat panel.

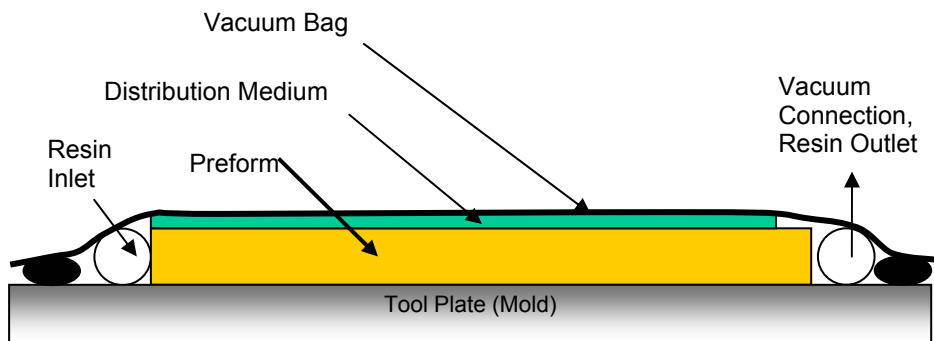


Figure 2-3 Typical VARTM set-up

For flat panels the tool is simply a plate of a suitable vacuum tight material, the preform is placed on the plate, and the remaining consumable components are arranged around the preform. The resin inlet and outlet distribute the resin along opposite edges of the preform. They therefore must not collapse under the vacuum pressure, and must allow resin to flow freely into and out of the preform. For the experimental part of the work presented in this thesis, steel springs were used to

form the inlet and outlet. The distribution medium, which is frequently used in VARTM, is typically a thermoplastic mesh, which may be thermoformed or knitted, although there are many other types of distribution media. The purpose of the distribution medium is to allow an easy flow path for the resin over the whole surface of the preform, so that the final infusion is merely through the thickness (a much shorter distance). In the experimental program presented in Chapter 6 no distribution medium was used, so that the flow process became one dimensional, and the changes in preform thickness could be more conveniently observed. The preform and inlets are covered by a vacuum bag film sealed around the edge using vacuum sealant tape (tacky-tape).

2.3 Darcy's Law, Permeability and the Effect of Preform Compaction

The analysis of the VARTM process is largely based on models developed for the related resin transfer molding (RTM) process, which has been successfully used in aerospace applications since 1985 [10]. In RTM, preforms are compressed inside a rigid tool, and the resin is then forced through the preform under applied pressure. Although the mold surfaces are known to deform under the elastic reaction forces built up in compressing the preform and under the pressure of the resin during and after injection, the tool deflection is ignored for modeling purposes and the preform geometry is treated as being fixed. In VARTM on the other hand, the preform deforms freely due to the pressure difference between the atmospheric pressure on the outside of the vacuum bag and the fluid pressures (resin and air) within (see Figure 2-4)

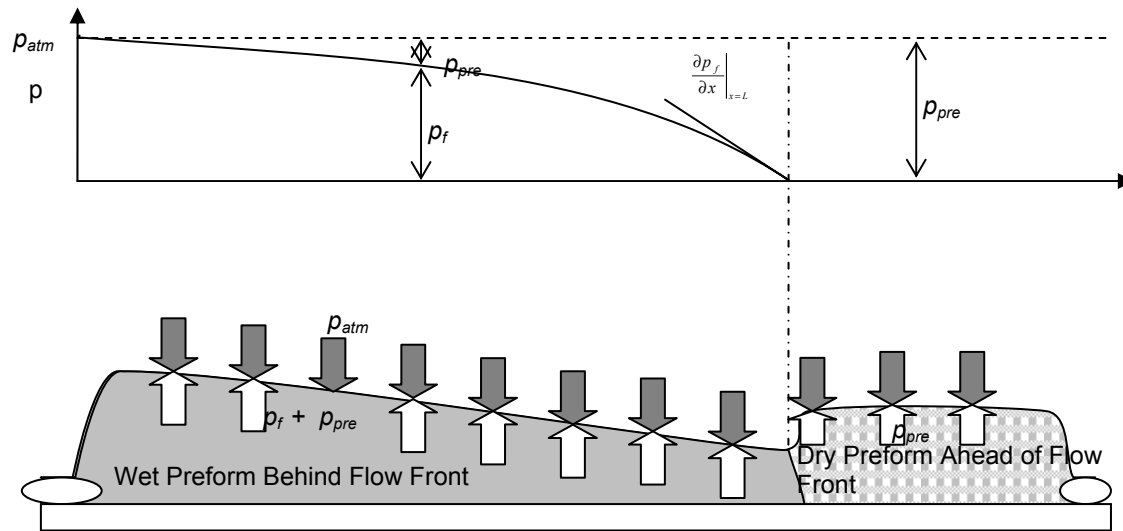


Figure 2-4 Basis of Flow Models for VARTM

2.3.1 Definition of Darcy Velocity

In composite processes where resin flows through fibers and in particular in RTM and VARTM, the flow process is typically described in terms of the pressure gradient ∇p , the resin viscosity μ , the permeability tensor \mathbf{K} , and the volume averaged or Darcy flow rate \mathbf{q} . The general form of the relationship

$$\mathbf{q} = \frac{\mathbf{K}}{\mu} \nabla p \quad (2.1)$$

is known as Darcy's law.

This is a three dimensional generalization of the empirical relationship Henri Darcy originally demonstrated in 1856, as part of a study on the factors affecting the flow of public water supplies in Dijon [11]. Darcy measured the rate of flow of water out of a packed bed of porous sand. He

showed that the outflow rate is proportional to the pressure head applied, and the cross sectional area, and inversely proportional to the thickness of the porous medium. Darcy’s experimental apparatus is shown in Figure 2-5. From this relationship the Darcy flow was defined as the volumetric flow per unit cross sectional area. According to Carman [12] the first significant modification to Darcy’s theory (by Dupuit) was to note that the actual cross sectional area available for fluid flow is less than the total cross sectional area, and that the average fluid velocity \bar{v} must therefore be higher

$$\mathbf{q} = \frac{1}{A} \int_{A_i} \mathbf{v} \cdot \mathbf{n} dA = \frac{A_i}{A} \bar{\mathbf{v}} = V_i \bar{\mathbf{v}} \quad (2.2)$$

Where \mathbf{q} is the Darcy velocity, \mathbf{n} is a unit vector parallel to \mathbf{q} , A_i is the area of the pores on a section perpendicular to the flow direction, A is the total cross-sectional area of the porous medium perpendicular to the flow direction, and V_i is the porosity of the medium at the cross section (the subscript i indicates a variable related to the interstitial space in the preform). Later work, in particular that by Slichter [13] and Terzaghi [14], based on the assumption that the flow could be approximated as viscous flow through a parallel set of channels, showed that the flow rate is inversely proportional to the fluid viscosity and from this the definition of the permeability K of a porous medium was developed as discussed in section 2.3.2.

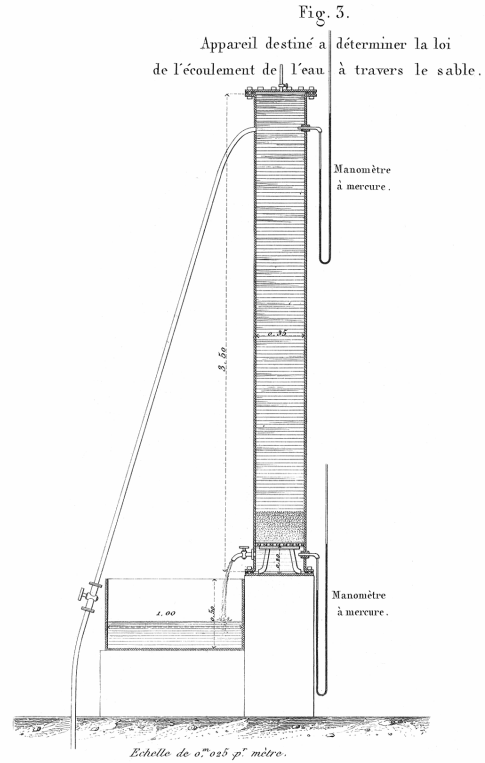


Figure 2-5 Henri Darcy’s Experimental Apparatus [11]

(Image From the collection of Glenn Brown, Stillwater OK, used by permission)

In the RTM case, for a constant preform type and thickness in a 1-D flow, the pressure gradient is constant between the inlet and outlet, and \mathbf{K} is only a function of position. In addition because the preform is static, we do not need to consider the movement of the preform in developing a governing equation for a model. In VARTM the changes in thickness result in a variation in permeability and therefore pressure gradient as shown in Figure 2-4 above. The relationships between pressure, permeability, and thickness are therefore important parts of the model. The other important consideration for VARTM is the correct definition of the Darcy flow within a moving preform. The basis of the applicability of Darcy's law is the assumption that the inertial terms in the fluid flow momentum equations are negligible. In this low Reynolds number flow regime, the pressure gradient is balanced with the viscous drag forces generated in the flow of the fluid through the channels which exist in the preform. As a result, the proper form of the constitutive law should balance the pressure gradient against the velocity of the fluid relative to the preform. With a multi phase material we need to deal with the resin and preform velocities in locally averaged form to develop a suitable macroscopic model, since at the microscopic level the quantities cannot co-exist at a single point.

The total volume Ω is divided into the volume occupied by tows Ω_t and the volume occupied by the interstitial space Ω_i , see Figure 2-6.

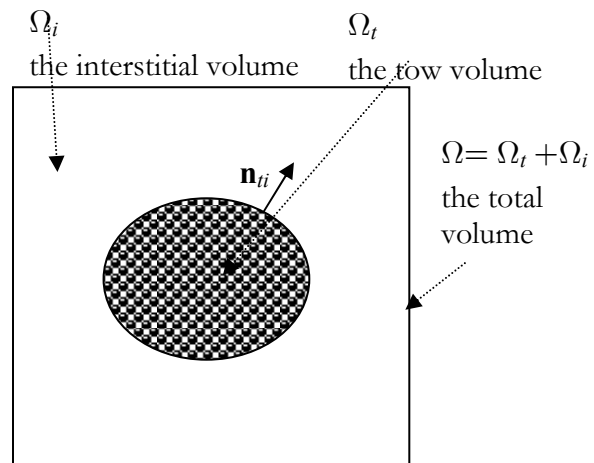


Figure 2-6 Terminology for Volume Averaging

Following the notation used by Gray et al. [15] we can define the velocity of the fluid averaged over the porous space as

$$\langle \mathbf{v}_i \rangle^i = \frac{1}{\Omega_i} \int_{\Omega_i} \mathbf{v} dV \quad (2.3)$$

Similarly we can define the velocity of the preform averaged over the space occupied by the preform

$$\langle \mathbf{v}_t \rangle^t = \frac{1}{\Omega_t} \int_{\Omega_t} \mathbf{v} dV \quad (2.4)$$

The averaged relative velocity of the fluid with respect to the preform is therefore

$$\langle \mathbf{v}_i \rangle^i - \langle \mathbf{v}_t \rangle^t \quad (2.5)$$

This quantity should be proportional to the pressure gradient, and inversely proportional to the viscosity. If we consider a static preform, $\langle \mathbf{v}_t \rangle^t = 0$

$$\mathbf{q} = \frac{1}{\Omega} \int_{\Omega_i} \mathbf{v} dv = \frac{\mathbf{K}}{\mu} \nabla p = \frac{\Omega_i}{\Omega} \langle \mathbf{v}_i \rangle^i = V_i \langle \mathbf{v}_i \rangle^i \quad (2.6)$$

The form of the Darcy equation we will use requires $\tilde{\mathbf{q}}$, the relative averaged fluid velocity, to be frame indifferent, and therefore for the static preform

$$\tilde{\mathbf{q}} = \frac{1}{\Omega} \int_{\Omega_i} \mathbf{v} dv = -\frac{K}{\mu} \nabla p = \frac{\Omega_i}{\Omega} \langle \mathbf{v}_i \rangle^i = V_i \langle \mathbf{v}_i \rangle^i \quad (2.7)$$

and therefore for the general case

$$\tilde{\mathbf{q}} = V_i (\langle v_i \rangle - \langle v_t \rangle) \quad (2.8)$$

where the factor of V_i comes from the use of the conventional form of the permeability.

2.3.2 Effect of Compaction on Permeability

Much of the study of flow through porous media has involved developing models to incorporate the effect of the geometry of the medium and the viscosity of the resin. The simplest models treated the porous medium as a set of channels through which fluid could flow [14]. Assuming that the fluid flow is smooth, the size of these channels can be related to various parameters of the porous medium. Carman gives a version of Kozeny's equation [12]

$$\langle v_i \rangle^i = -\frac{k_0 V_i^2}{\mu A^2} \frac{dP}{dx} \frac{L}{L_e} \quad (2.9)$$

where $\langle v_i \rangle^i$ is the average fluid velocity, A is the surface area presented to the fluid per unit volume of preform, μ the viscosity, $\frac{dP}{dx}$ the pressure gradient, k_0 a constant related to the shape of the granular particles assumed to make up the porous medium, and $\frac{L}{L_e}$ the ratio of the effective flow length to the apparent flow length. The effective flow length is the actual length a fluid particle must travel through the preform and the apparent flow length the straight line distance across the preform. Noting that

$$A \propto (1 - V_i) \quad (2.10)$$

and substituting this into Eqn (2.9) (incorporating the proportionality coefficient into k_0) yields

$$\langle v_i \rangle^i = -\frac{k_0 V_i^2}{\mu (1 - V_i)^2} \frac{dP}{dx} \frac{L}{L_e} \quad (2.11)$$

and therefore

$$q = V_i \langle v_i \rangle^i = -\frac{k_0 V_i^3}{\mu (1 - V_i)^2} \frac{dP}{dx} \frac{L}{L_e} \quad (2.12)$$

(Here we note that as the preform is considered to be static we use the standard Darcy flow rate q rather than the relative Darcy flow rate \tilde{q} .)

From which assuming $V_f = 1 - V_i$, the Carman-Kozeny equation for variation of permeability with volume fraction is derived as

$$K = k_o \frac{(1 - V_f)^3}{V_f^2} \quad (2.13)$$

Many more complex forms of this relationship have also been derived [16-18], however for the preform models used in this thesis the Carman-Kozeny relation will be used.

2.3.3 Measurement of Permeability

The measurement of permeability has been a significant problem in resin transfer molding, due in part to the complexity of adopting an acceptable experimental method. Several authors have used radial [19, 20] and hemi-spherical flow experiments, in which resin or a suitable substitute (e.g., corn syrup, oil, or glycerin) are injected into a preform and the resin flow front speed measured. Others have argued that this method incorrectly calculates the permeability since it measures the

unsaturated flow front (i.e., neglects the unfilled regions within the tow behind the flow front) and measures an advancing flow front, and will therefore include wetting effects, which are not accounted for in Darcy's law. To calculate the permeability without these effects, unidirectional flow experiments have been used in which the flow of resin through a fully saturated preform is measured [21]. However, it has been noted that the permeability measured in this manner can be significantly different from the permeability measured in advancing flow front experiments [3]. Kim [22] used a gas flow method to measure permeability in which nitrogen gas was used instead of a liquid resin substitute, and the gas flow rates were adjusted to maintain an appropriate Reynolds number relationship for the interstitial resin flow within the preform. This method proved successful, and gave results comparable to radial flow experiments previously carried out by the same research group [23]. As noted above and described in more detail in section 5.4 below, permeability is a measure of the mobility of a fluid through the preform (for a given viscosity). The small length scales involved ensure that the mobility of the resin is largely governed by viscous drag forces as the resin passes between tows and between fibers, and these forces increase considerably as the available resin channels are reduced and the inter fiber and inter tow gaps are reduced.

2.4 Areas of Model Development

In this thesis no new developments are proposed for the measurement or modeling of permeability. Significant developments in modeling are made by incorporating additional preform compaction effects into flow models. In particular, a new model for the relationship between the resin fluid

pressure and the preform compaction is developed in Chapter 3, and this and the effect of partial saturation on the preform stiffness are incorporated into a VARTM flow model in Chapter 5.

2.5 Areas of Experimental Development

To properly validate the proposed models, methods to measure the preform deformation and preform saturation during resin infusion were required. Chapter 6 discusses these developments.

3 Preform Compaction

3.1 Introduction

The fiber compaction process is complex, and has been studied for a considerable time in the textile industry. It is almost immediately apparent that the compaction process is non-linear, since an uncompacted textile will offer almost no resistance to compaction, whereas at the limit of compaction we can expect the stiffness to be close to the stiffness of a solid mass of the material making up the fiber. In the literature concerning compaction of textiles, many of the observed behaviors of fabric preforms have been discussed, including non-linearity, time dependent behavior, time-independent hysteresis, permanent deformation, and cyclic loading effects. One difficulty for VARTM modeling has been that in composite process modeling the only behavior of interest has been the compaction behavior of the reinforcement (aligned fibers in prepregs, filament windings, the fabrics and braids and random mats used in liquid molding processes etc). The behavior of the mat while the compacting pressure is released, or on subsequent reapplication of the compaction pressure, has not been fully addressed.

3.2 Compaction Process Behavior

Chen et al [24, 25] categorized the types of deformation which might be expected in a typical preform. Noting that preforms are multi-scale, we can also categorize the deformations in terms of the component scale which is deforming.

Fabric Level Deformation:

The fabric layers are not flat, and when initially stacked the tow bundles in two adjacent layers may not be optimally nested. During compaction the fabric's layers may slip, and in doing so, the nesting of the tows may improve.

The importance of nesting in compaction is very dependent on the fabric architecture, for example continuous filament mat fabrics will not exhibit this behavior since the tow level structure is not sufficiently regular to permit nesting of the tows. Figure 3-1 also shows that this mechanism will have a significant effect on the interstitial flow, since while the fabrics are not tightly nested, flow channels of significant size exist between the tows in adjacent fabric layers. After nesting, these flow channels are significantly restricted. (This gives some indication as to why no simple model will handle the variation in permeability perfectly.)

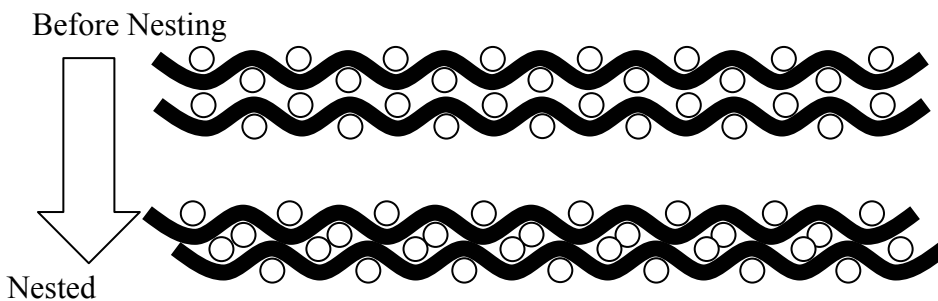


Figure 3-1 Layer Nesting

Tow Level Deformation:

At the tow scale, three mechanisms are identified:

- Tow Bending
 - Tow cross section deformation (without cross section area change)
 - Tow flattening (or tow crimp reduction)
-

Figure 3-2 Tow Scale Fabric Deformation Mechanisms

The tow level deformation relates to the changes in the contact points between the fiber tows, and to the effective stiffness of the tows themselves, which is highly dependent on the interfiber friction and the number and position of interfiber contact points. We also note that none of the identified tow level mechanisms results in an increase in the fiber volume fraction within a tow, only a reduction in interstitial space (and hence a direct effect on the macroscopic permeability and not microscopic permeability).

Fiber Level Deformation:

Figure 3-3 Fiber Scale Deformation Mechanism, Tow Cross Section Reduction

At the fiber level reductions in cross section due to deformation also affect the tow bending stiffness; models for aligned fibers can be directly related to the tow cross section reduction.

3.2.1 Model Development

Models for the compaction of the preform in composite processing have typically concentrated on the initial fabric compaction, although the effect of repeated compactions and the hysteresis observed between the loading and unloading behavior have been noted [26]. One reason for this is that in the traditional composite manufacturing methods, the fiber stack is compacted monotonically from its initial state to the final consolidated thickness, and hence the main interest has been in the first load application. In textile processing, the effect of multiple compactions has been studied in more detail, though typically the models developed have been for randomly oriented fibers (typical in processing of wool). The earliest physical model [27] was developed over 50 years ago by Van Wyk, who was studying the compaction of wool and calculated the stiffness by assuming that the deformation was solely the result of fibers bending between contact points (see Figure 3-4).



Figure 3-4 Van Wyk Model Basis

Making additional assumptions about the distance between contact points and orientation of the fibers allowed the following expression to be derived:

$$p = KEV_f^3 (V^3 - V_0^3) \quad (3.1)$$

where p is the applied pressure, E the elastic modulus of the fibers, V_f the volume of material in the system (the fiber mass divided by the fiber density), V the current volume, and V_0 the volume at zero pressure. K is an empirical constant required due to the simplifying assumptions used in deriving the model. Although this model could be used to fit the loading part of the compaction curve for wools, it has several significant weaknesses, including its inability to account for the different behavior on unloading, and its inability to account for the observed permanent deformation of the fiber stack. For composites it has a further disadvantage in that it does not deal with aligned fibers. Gutowski et al. [16, 17] whilst initially unaware of the prior work of Van Wyk, incorporated some of the same ideas for their model of the transverse compression of aligned fiber bundles. This model was developed for the compaction of pre-preg and hence considered a lubricated fiber bundle (neglecting any losses associated with fiber slippage).

Gutowski assumed that individual fibers have a sinusoidal waviness of the form

$$y = \frac{a}{2} \left(1 - \cos \frac{2\pi x}{L} \right) \quad (3.2)$$

where y is the transverse position of the fiber axis, x the position on an axis aligned with the average direction of the fiber, a the amplitude of the waviness and L the wavelength. The fiber is deformed through the application of an end load P_x and a transverse load P_y as shown in Figure 3-5.

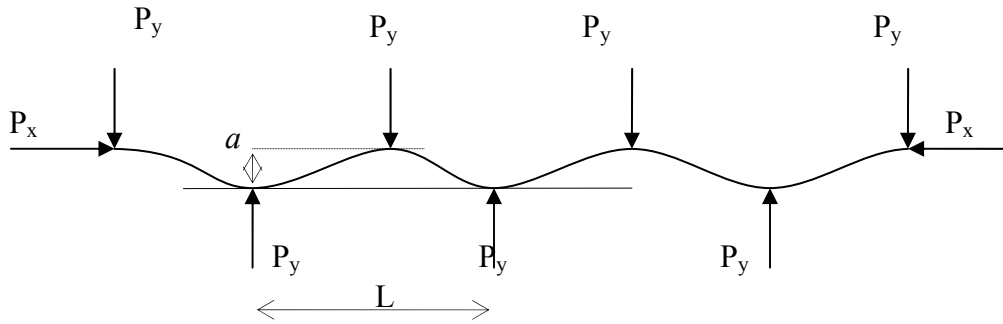


Figure 3-5 Gutowski Compaction Model [16, 17]

The deflection of the fiber is then calculated as

$$\begin{Bmatrix} \Delta_x \\ \Delta_y \end{Bmatrix} = \begin{bmatrix} \frac{a^2 L}{8EI} + \frac{L}{EA} & -\frac{aL^2}{4\pi^2 EI} \\ -\frac{aL^2}{4\pi^2 EI} & -\frac{L^3}{192EI} \end{bmatrix} \begin{Bmatrix} P_x \\ P_y \end{Bmatrix} \quad (3.3)$$

Where E is the bending modulus of the fiber, I the moment of inertia of the fiber cross section, A the cross sectional area, P_i are the applied loads, and Δ_i the deflections. Assuming for transverse compaction that the fiber end loads are zero, and converting the transverse load to a pressure by constructing a unit cell around a representative fiber wave of length L , and height and width h we can relate the pressure on the unit cell wall ($p=P_y/Lh$), to the unit cell transverse strain ($e_t=\Delta_y/h$)

$$e_t = p \frac{L^4}{192EI} = p \frac{L^4}{3\pi d^4 E} \quad (3.4)$$

where d is the fiber diameter. We can then show that

$$e_t = 1 - \sqrt{\frac{V_f}{V_o}} \quad (3.5)$$

where V_f is the current fiber volume fraction, and V_o is the fiber volume fraction at zero pressure.

Gutowski assumes that the ratio of the distance between contact points to the amplitude of the fiber waviness is a constant β

$$\beta = \frac{L}{a} \Rightarrow \frac{L}{d} = \beta \frac{a}{d} = \beta \left(\sqrt{\frac{V_a}{V_f}} - 1 \right) \quad (3.6)$$

where V_a is the maximum V_f based on a packed square box. Hence

$$p = \frac{3\pi E}{\beta^4} \frac{\sqrt{\frac{V_f}{V_o}} - 1}{\left(\sqrt{\frac{V_a}{V_f}} - 1 \right)^4} \quad (3.7)$$

This simple model can capture the behavior of even complex preforms adequately, despite being designed solely for aligned fiber arrays. Unlike the simpler empirical power law proposed by Robitaille [26, 28] it has the advantage of having no singularities over the range of use ($V_o < V_f < V_a$). Robitaille models the compaction as

$$p = aV_f^b \quad (3.8)$$

where a and b are empirical constants. The singularity occurs in the preform thickness which is inversely proportional to the volume fraction. Since $p=0$ implies $V_f=0$, this gives an infinite

thickness, which is problematic for any VARTM model. All these models consider deformation only at the fiber level, and assume either random fibers or aligned fibers. If we wish to consider woven fabrics, a considerably more complex physical model is required. Chen and Chou [25] created a comprehensive finite element model for plain weave fabrics, however this type of modeling requires significant effort and the results are typically not applicable to variations in the fabric type. In their model they develop a unit cell for the fabric and use experimentally determined pressure profiles at the contact points between fabric layers and assumed pressure profiles at the contact points between tows within each layer. These models do not show significantly better performance than the simpler models of Gutowski [17] and Robitaille [26, 28, 29], though they have the advantage of being calculated from geometrical measurements of the fabric's architecture. In addition none of the models discussed so far can account for the hysteresis behavior observed in real fabrics, the permanent deformation, or the effects of cyclic loading.

In the textile industry literature, it has been noted that there are two types of loss mechanism present in the compaction of random assemblies of fiber. Both time dependent (viscous type) and time independent (frictional type) loss mechanisms are seen. In liquid composite molding, Bickerton [30-35] has studied the time dependent effects of preform loading. Bickerton observed both a loading rate effect and a relaxation after the end of loading. From this he proposed a viscoelastic model, which works acceptably for monotonic compaction as found in RTM and compression RTM, however it does not work well for the slow cyclic compaction observed in VARTM, largely because the dissipative viscous part of the behavior is not sufficiently recoverable on unloading. Dunlop [36, 37] found that in wool a hysteresis effect was present between the

loading and unloading behaviors which was independent of the rate of loading, and from this concluded that this effect was due to friction. This same effect can be observed in the VARTM preforms tested, and it is this frictional effect which causes the errors observed when trying to fit Bickerton's model to VARTM cyclic loading data. Dunlop's model, like Bickerton's is empirical and based on frictional sliding elements, whereas Bickerton's is based on Voight type viscous elements.

As with the other models, once the preform becomes complex a computational method is required to calculate the behavior. Beil and Roberts [38, 39] developed a model for the behavior of random fiber assemblies by using a Love-Kirchhoff model for a long thin rod to represent the fiber, and assembling a number of such rods within a cubic unit cell. The inter fiber contacts were modeled as perpendicular linear springs with one spring acting to separate the fibers, and the second representing static friction. The force allowed in the static friction spring was limited by a slippage criteria, which if exceeded replaced the spring by a non-linear kinetic spring, representing the viscous slippage of the fibers at the contact points. The model is capable of reproducing representative behaviors for both the hysteresis and the permanent deformations which are observed in typical textile fiber assemblies at the expense of considerably more complexity than is reasonable for a simple VARTM model.

3.3 The Compaction Process in VARTM

3.3.1 Reference State and Definition of Strain

Preforms are typically very compliant at low levels of compaction, and it is very difficult to properly define the initial thickness of the fabric, since this can be affected by the way the fabric

was stored, the time since the fabric was removed from the roll, and even the method of measurement. In addition the deformations can be very large compared to the initial nominal thickness. It is therefore more realistic to measure and compare the applied stress σ_{zz} to the achieved volume fraction which is independent of the initial thickness, rather than use a measure, such as engineering strain ε , which is very dependent on the initial thickness. An alternative to this is to use the true strain ϵ rather than engineering strain. We can relate thickness, V_f , ϵ and ε using the relationship

$$\epsilon = \ln\left(\frac{V_f^*}{V_f}\right) = \ln\left(\frac{h}{h^*}\right) = \ln(1 + \varepsilon) \quad (3.9)$$

Where V_f^* is the reference volume fraction and h , h^* are the preform thickness and reference preform thickness respectively. This shows the benefit of using the true strain rather than engineering strain, since any error or discrepancy in the measurement of initial volume fraction becomes a constant error in the calculation of true strain. In addition, for comparison of models it is possible to correct all strains to those related to a reference volume fraction.

3.3.2 Compaction Pressure

In the VARTM process the compaction pressure on the preform is usually assumed to be a pressure loading from the balance between the fluid inside the vacuum bag and the atmospheric pressure outside the bag. The local gradients in thickness are considered small enough to assume

$$p_c = p_{atm} - p_{fluid} = -\sigma_{zz} \quad (3.10)$$

where p_c is the compressive pressure on the preform, p_{atm} the atmospheric pressure ($\sim 101\text{Kpa}$) and p_{fluid} the pressure of the resin or air inside the bag, $-\sigma_{zz}$ is the compressive stress on the bag surface.

During a typical process cycle the vacuum bag will be evacuated, thereby compressing the preform. One or more vacuum leak tests will be carried out, each of which will involve a partial or

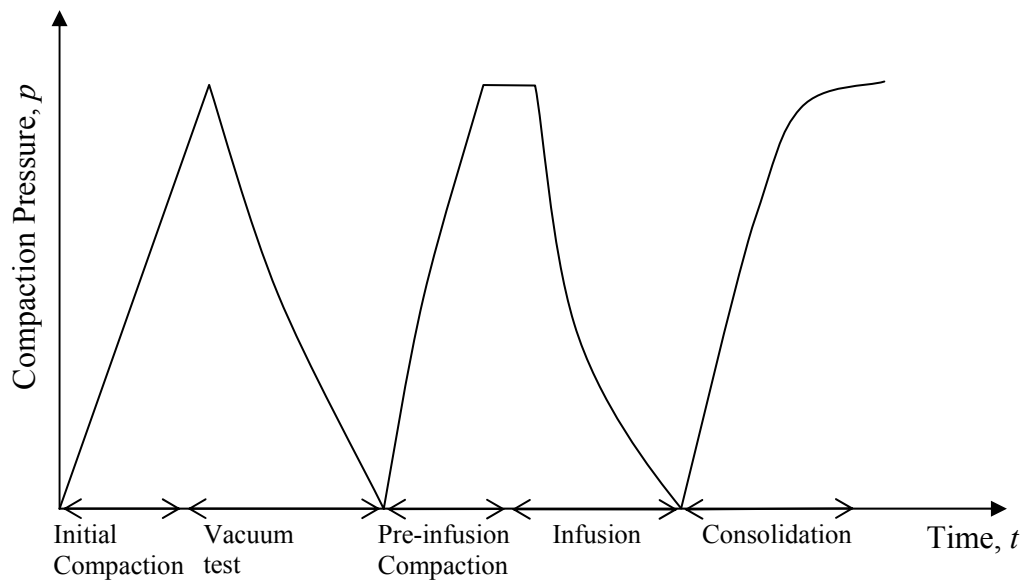


Figure 3-6 Schematic of preform compaction stages

full decompaction of the preform. Before infusion, the bag is evacuated again and the resin flow is allowed to start. The pressure drop in the dry part of the preform is very small compared to the pressure drop in the resin saturated part, so at any point the preform remains compressed at 1 atmosphere until the resin passes, after which the fluid pressure rises gradually, thus reducing the preform compaction. At the end of infusion (when the resin has reached the outlet) the inlet is

closed and the fluid pressure through most of the system gradually decreases. Figure 3-6 and Table 1 show a typical preform compaction pressure cycle.

Table 1 Preform Compaction Stages

1.	preform consolidation under vacuum
2.	preform compaction released as part of vacuum integrity testing
3.	preform reconsolidation prior to infusion
4.	infusion starts, as flow front passes point on interest, the consolidation pressure slowly decreases
5.	end of infusion, inlet closed, fluid pressure slowly decreases, resulting in an increase in compaction pressure

To properly model the VARTM process, we therefore need a model to describe the behavior of the preform after the first initial compaction cycle, including a description of the behavior after partial unloading and reloading to the full compaction state. None of the models reported to date can do this.

3.4 Proposed Model

Various models have been proposed for the non-linear elastic behavior observed. For the loading model described here we use a modified form of Gutowski's model Eqn (3.7) normalized using the maximum compaction pressure applied $p_{\max} = p_{atm}$

$$\frac{p_c}{p_{\max}} = k \frac{\left(1 - \sqrt{\frac{V_f}{V_0}}\right)}{\left(\sqrt{\frac{V_a}{V_f}} - 1\right)^4} \quad (3.11)$$

For the unloading behavior a simple empirical relationship is used to fit the curve

$$p_c = k \left(1 + \varepsilon - \frac{V_f}{V_f^*} \right)^n - k \left(1 + \varepsilon - \frac{V_o}{V_f^*} \right)^n \quad (3.12)$$

where $V_f^* = V_f(p_c = p_{atm})$. To simplify model development further we assume that the viscoelastic behavior is small and normalize the model using the maximum pressure p_{atm} (101Kpa) and the volume fraction at the maximum pressure V_f^* defining the following normalized parameters for pressure and volume fraction respectively

$$\beta = \frac{p_c}{p_{atm}}, \quad \alpha = \frac{V_f}{V_f^*} \quad (3.13)$$

The basic preform loading model becomes

$$\beta_l = \frac{(\sqrt{\alpha_a} - 1)^4 \left(1 - \sqrt{\frac{\alpha}{\alpha_0}} \right)}{\left(1 - \sqrt{\frac{1}{\alpha_0}} \right) \left(\sqrt{\frac{\alpha_a}{\alpha}} - 1 \right)^4} \quad (3.14)$$

and the unloading model

$$\beta_u = \frac{(\alpha_a - \alpha)^n - (\alpha_a - \alpha_0)^n}{(\alpha_a - 1)^n - (\alpha_a - \alpha_0)^n} \quad (3.15)$$

where the subscripts l, u refer to the loading and unloading behavior for the second and subsequent full loading cycles. The constant terms in these equations are set to ensure that $\beta(\alpha = \alpha_0) = 0$ and $\beta(\alpha = 1) = 1$. We note from experimental observation that, as long as the load is restricted

to the load limit of the first cycle, any subsequent load history will be bounded by these two envelope curves.

$$\beta_u(\alpha) \leq \beta(\alpha) \leq \beta_l(\alpha) \quad (3.16)$$

The lack of a unique value of α for any value of β (and vice versa) is a problem for modeling. However, if we assume (as appears to be true from experimental observations) that the curves for loading from intermediate value form a non intersecting family of curves, we can at least develop a model for the incremental unloading and loading behavior from any point as long as we know both α and β .

3.4.1 Reloading from Partial Unloading

A simple interpolation model for the reloading from partial unloading would take the form

$$\begin{aligned} \beta^*(\alpha, \alpha^*) &= \beta_l(\alpha) - f(\alpha, \alpha^*)(\beta_l(\alpha) - \beta_u(\alpha)) \\ f(\alpha = \alpha^*, \alpha^*) &= 1 \\ f(\alpha = 1, \alpha^*) &= 0 \end{aligned} \quad (3.17)$$

where $\beta_l^*(\alpha, \alpha^*)$ is the normalized pressure for loading from α^* , having unloaded from $\alpha=1$ to α^* , f is an interpolation function. A simple linear interpolation function would be

$$f(\alpha, \alpha^*) = \frac{1-\alpha}{1-\alpha^*} \quad (3.18)$$

This model works fairly well for values of α^* close to 1, but does not work well for smaller values.

This leads to a simpler model based on a linear reduction in the difference between β and β_l during reloading

$$\begin{aligned} \beta^{**}(\alpha, \alpha^*) &= \beta_l(\alpha) - f(\alpha, \alpha^*)(\beta_l(\alpha^*) - \beta_u(\alpha^*)) \\ f(\alpha = \alpha^*, \alpha^*) &= 1, f(\alpha = 1, \alpha^*) = 0 \end{aligned} \tag{3.19}$$

A schematic of this is shown in Figure 3-7.

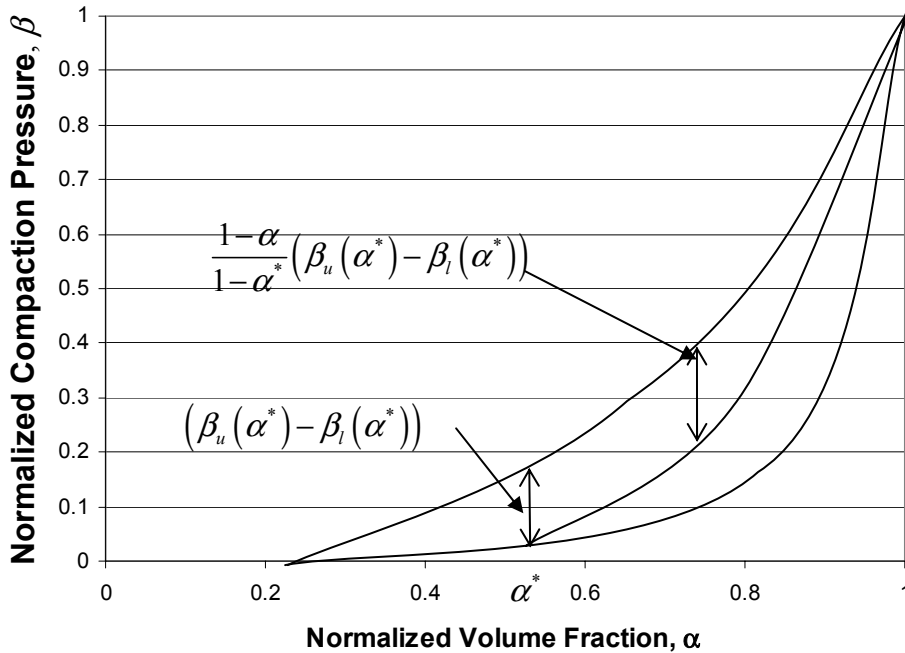


Figure 3-7 Schematic of the Modified Loading and Reloading Model

Converting the final form (3.19) to a more useable one we have

$$p = p_{\max} \left(\beta_l(\alpha) - \left(\frac{1-\alpha}{1-\alpha^*} \right) (\beta_l(\alpha^*) - \beta_u(\alpha^*)) \right) \tag{3.20}$$

Differentiating this gives

$$\frac{\partial p}{\partial \alpha} = p_{\max} \left(\frac{\partial \beta_l}{\partial \alpha} + \frac{\beta_l}{1-\alpha} \right) + \frac{p}{1-\alpha} \tag{3.21}$$

3.4.3 Effect of Saturation on Compaction in Dual Scale Preforms

It has been noted that on lubrication the compliance of the preform increases, and typically this effect is evaluated on fully lubricated preforms. In a dual scale preform the tows within the preform become saturated over a short period after the interstitial regions are filled with the infusing fluid. It seems reasonable therefore to assume that during the infusion of a dual scale preform the change from dry behavior to lubricated (wet) behavior will not be instantaneous, and therefore it is reasonable to use some form of interpolated model for the change in behavior, with the interpolation parameter being the tow saturation. This model takes the form

$$h = V_{sat}h_s(p) + (1 - V_{sat})h_d(p) \quad (3.24)$$

Where V_{sat} is the tow saturation, h is the preform thickness and h_d and h_s are the models for the relationship for the wet (saturated) and dry cases respectively.

3.4.4 The Effect of Varying Saturation on Behavior

One effect which was not considered in the development of the model was the rate of change of thickness as a result of saturation. The models assume that this occurs instantaneously, however, especially in the case of the CFM, this assumption produces unrealistic results. As a limiting case, an alternative model was also used in the analysis of experimental data, in which the change in saturation had no effect on the preform thickness, which in effect simulates an infinitely slow change in thickness as a result of saturation. This is shown schematically in Figure 3-9.

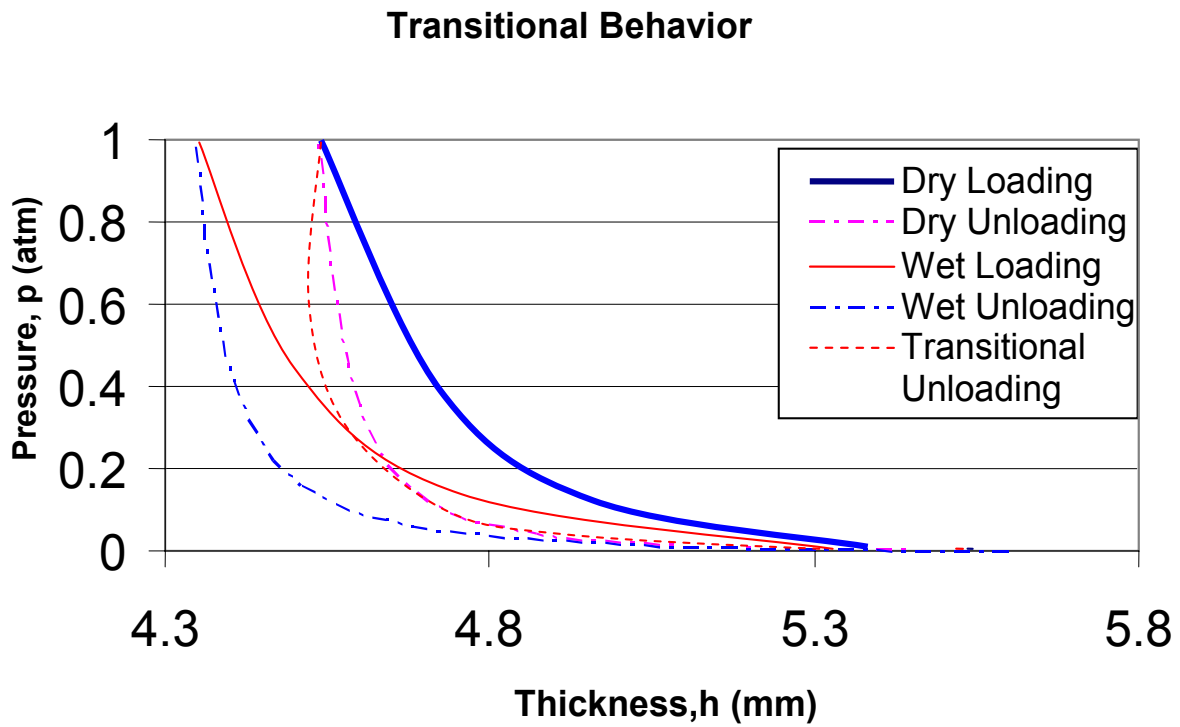


Figure 3-9 Saturation Behavior, Dry and Wet Showing Possible Transitional Behavior for Saturation while Unloading

4 Experimental Evaluation of Preform Compaction

4.1 Materials

Two glass fiber reinforcement fabrics were used in these evaluation trials, Hexcel 7500 style plain weave glass and OCF8610 Continuous Filament (Random) Mat. Figure 2-2 shows photographs of these materials.

Table 2 Plain Weave Fabric Properties

Material	Hexcel 7500 style glass fabric
Weave style	Plain Weave
Tow Type	ECG 37 ½
Fiber count/tow	Each strand in the plain weave is made from a twisted pair of 816 filament tows.
Tow Count	16 ends/in 14 picks/in
Weight/Unit Area	327 g/m ²

Table 3 CFM Random Mat Properties

Material	Owens Corning Fiberglass OCF8610 Continuous Filament mat
Weave Style	Random
Fiber Type	ECG
Typical fiber count/tow	20~100
Weight/Unit area	450 g/m ²

The ECG fibers used in both fabrics are e-glass with a diameter of between 8.89µm and 10.12µm.

4.2 Preliminary Evaluation of Basic Preform Parameters

To set up an appropriate test program for assessing the model performance, some preliminary testing was required. The main objectives of this preliminary testing were to establish:

- The effect of Poisson's ratio of the preform under uniaxial loading
- The effect of the lubricating fluid on the behavior of the lubricated preform under uniaxial loading
- The effect of loading rate on behavior

4.2.1 Poisson's Ratio for Plain Weave Fabric under Transverse Compression

Most preform tests use a test specimen which is thin in the loading direction. To ensure that the results are not significantly affected by Poisson's ratio, a thick specimen with a small diameter, was tested. The test specimen was made by cutting the plain weave preform, which is expected to have a higher Poisson's ratio than the CFM, into 25.4mm disks. To make a consistent stack, the disks were cut using a steel punch. Each circle of fabric was held by the sides of the punch, eventually forming a 99 layer stack.

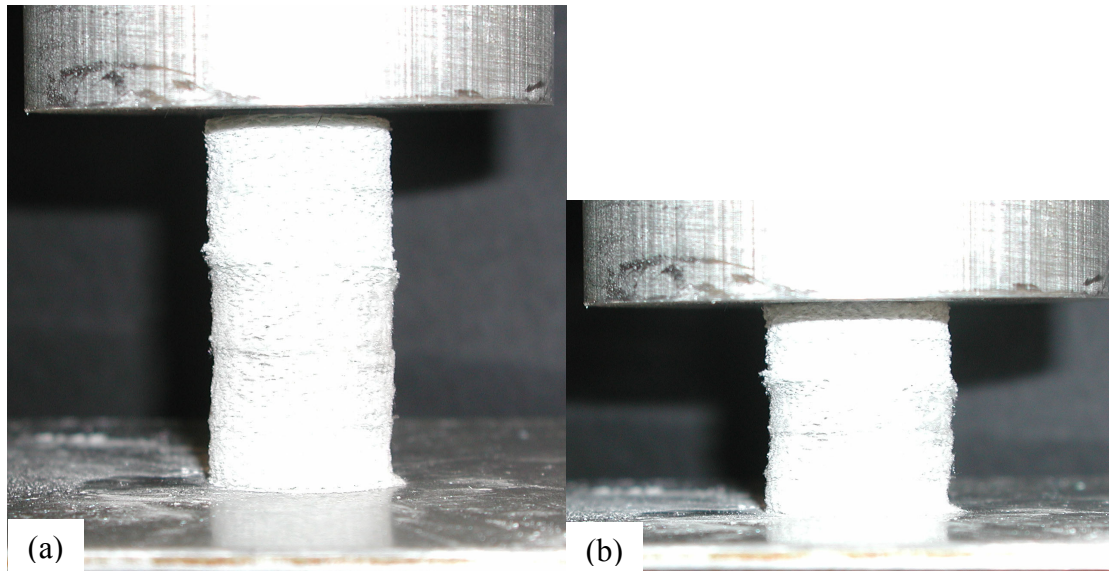


Figure 4-1 Plain Weave Fabric under Compression, (a) Unloaded and (b) Compressed to Approximately 50% of the Original Thickness.

The fabric stack was placed in a servo-hydraulic testing machine and compressed at a displacement rate of 1.27mm/min. The vertical displacement was measured using the cross head displacement of the machine, and the horizontal deformation was measured by image analysis. Figure 4-1 shows two images of the stack under compression. It is worth noting that in the images in Figure 4-1 the fabric stack was deliberately overexposed to create a more distinct edge for the image analysis.

During compaction, the preform stack showed a typical non-linear load displacement behavior for this type of material (see Figure 4-2). The stack was loaded to considerably higher final load than the subsequent fiber compaction tests, so that a sufficiently large transverse strain could be observed.

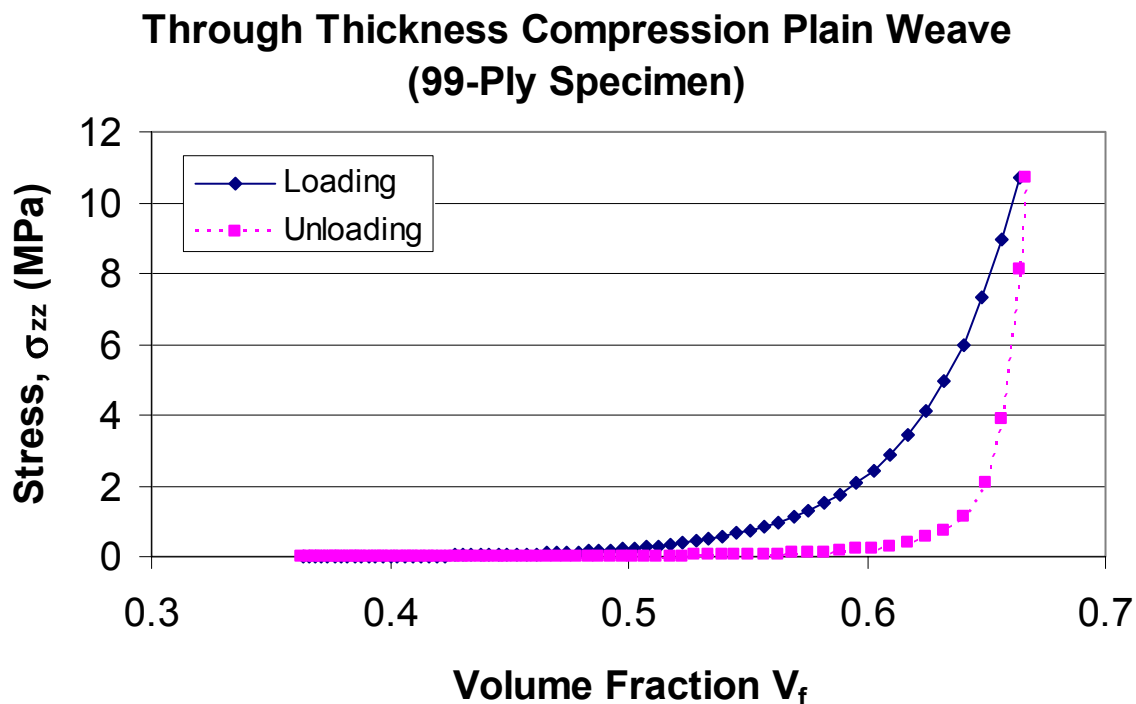


Figure 4-2 Load vs Volume Fraction for 99 Ply Columnar Stack of Plain Weave Glass Fabric

Image analysis was performed to measure the change in length of horizontal lines on the specimen taken during deformation. The average width of the preform in pixels was then calculated and the strains parallel to the applied compression loading (ϵ_3) and perpendicular to it (ϵ_1) are shown in

Figure 4-3

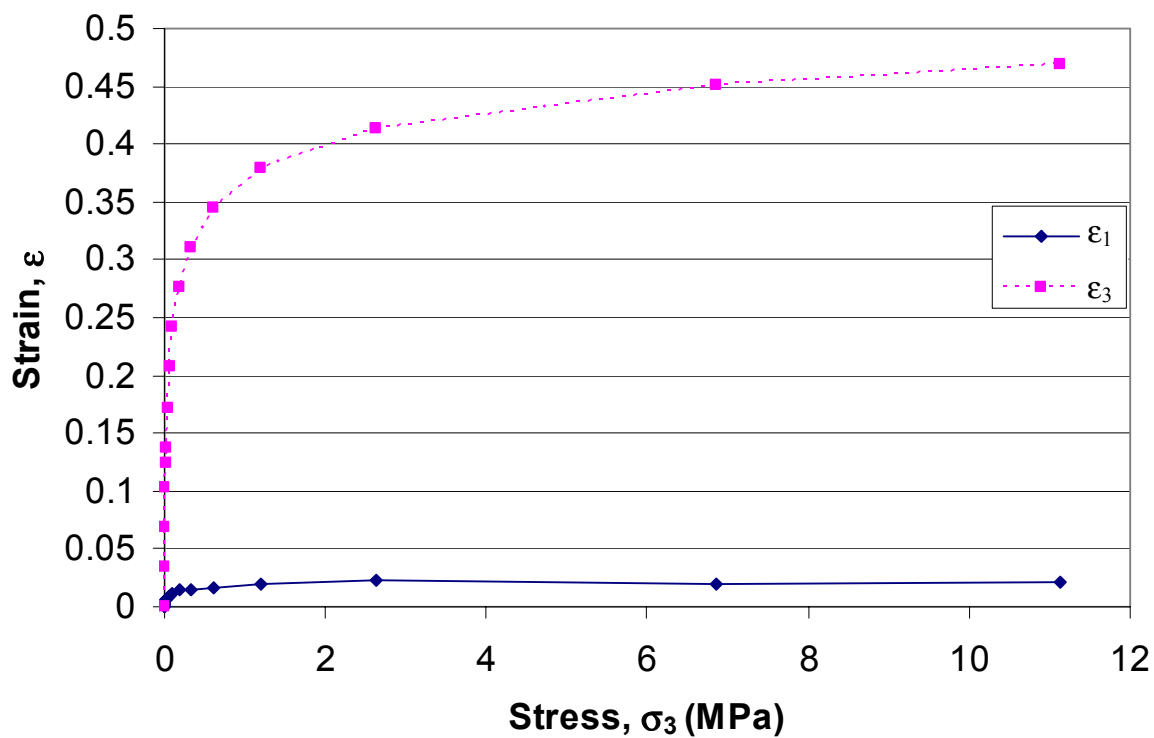


Figure 4-3 Axial and Transverse Strains in Fabric Subject to Transverse Compression

Based on this, Poisson's ratio was determined to be 0.0483 (see Figure 4-4), which is too low to significantly affect the results of the standard planar tests generally used.

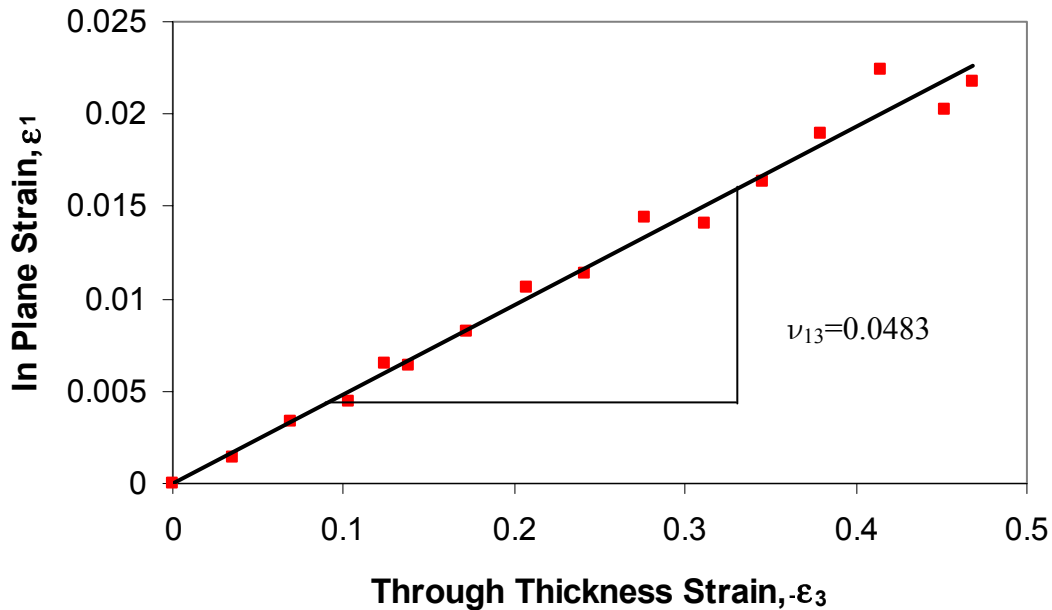


Figure 4-4 In-Plane vs Through Thickness Strain under Through Thickness Compression for Plain Weave Fabrics

4.2.2 Effect of Lubricating Fluid on Preform Compaction

In evaluating liquid composite molding processes various fluids have been used to test the permeability of the preform including resins, silicone oil, glycerin and vegetable oil [40, 41]. In testing for compaction parameters, similar choices for the fluid are possible; however, in addition to the problems with cleaning up most of these fluids after testing an additional difficulty in using any viscous fluid is that the fluid viscosity can affect the measured pressure during compaction as a function of the displacement rate. As a result, if a viscous fluid is used a correction factor must be calculated to ensure that the effect is small or to correct the measured pressure. To calculate the correction factor, we consider a pair of circular parallel plates of radius R moving toward each other at constant velocity v , assuming that

- The fluid pressure is a function only of the radius
- The preform pressure is independent of position
- Fluid flows only radially

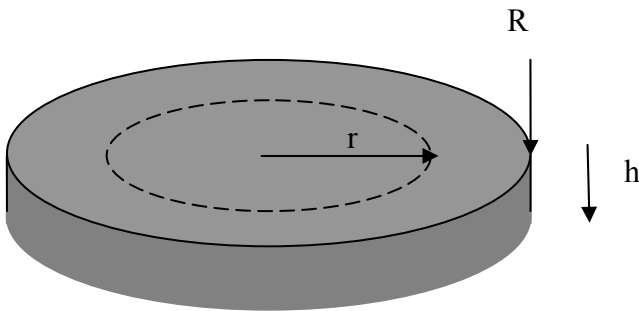


Figure 4-5 Flow Model for Compaction Tests

The total volume of fiber within the domain is constant ($V_f \pi R^2 h$), hence the total outflow of resin must equal the change in volume of the system

$$\int_0^{2\pi} q_r h R d\theta = \pi R^2 v \quad (4.1)$$

where q_r is the radial Darcy or volume averaged velocity. In fact this relationship must hold at any radius, therefore

$$2\pi r \bar{q}_r h = \pi r^2 v \quad (4.2)$$

where \bar{q}_r is the radially averaged Darcy velocity. If we assume an average radial permeability K_r ,

we can then show that, for a boundary condition $p_{fluid}=0$ at $r=R$

$$p_{fluid} = \mu v \frac{R^2 - r^2}{4hK_r} \quad r \leq R \quad (4.3)$$

and the total force on the plate due to the resistance to fluid flow, in the preform is therefore

$$P_{flow} = \frac{\pi \mu v}{4hK} R^4 = Lv \quad (4.4)$$

where L is a parameter including the effects of viscosity, thickness and permeability. To test this, a 75mm diameter plate was used to compress a plain weave preform at varying compaction rates. From Eqn (4.4) above we can see that the excess pressure due to the fluid flow resistance of the preform at any specified thickness is proportional to the test machine crosshead rate. In Figure 4-6 we can see the experimental data overlaid with linear fits of the pressure compared to the compaction rate.

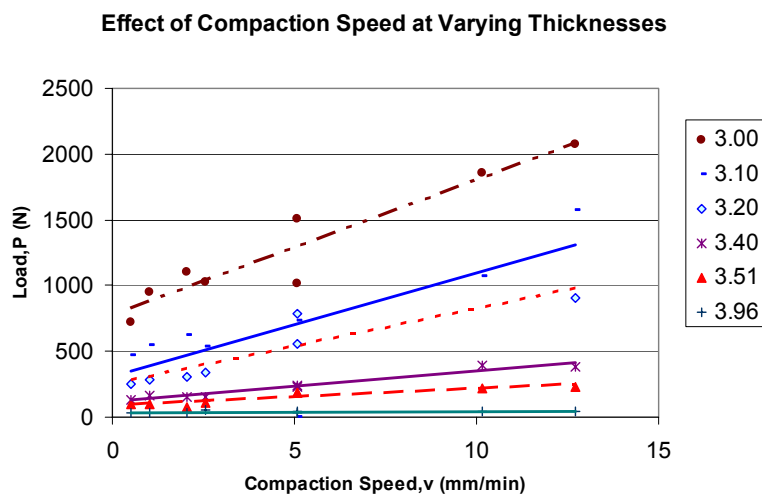


Figure 4-6 Effect of Compaction Speed on Measured Load

From these linear fits we can calculate experimental values of $L = \pi R^4 \mu / 4hK_r$ for various thicknesses of preform.

Substituting a modified form of the Carman-Kozeny equation

$$Kh = k_0 h_0 \left(\frac{h_0}{h} - 1 \right)^3 \quad (4.5)$$

where h is the thickness and h_0 the thickness at $V_f=100\%$ in the expression for L we obtain

$$L = \frac{\pi \mu}{4k_0 h_0 \left(\frac{h_0}{h} - 1 \right)^3} R^4 \quad (4.6)$$

If we plot L versus $\left(\frac{h_0}{h} - 1 \right)^{-3}$ the slope should be constant. We can see from the satin weave results that although there is a region of constant slope, the line fit does not intersect the y axis at the origin as it should for this model. This is probably due to the effect of time dependent preform compaction behavior, though it could also be due to changes in the form of K as the preform thickness decreases.

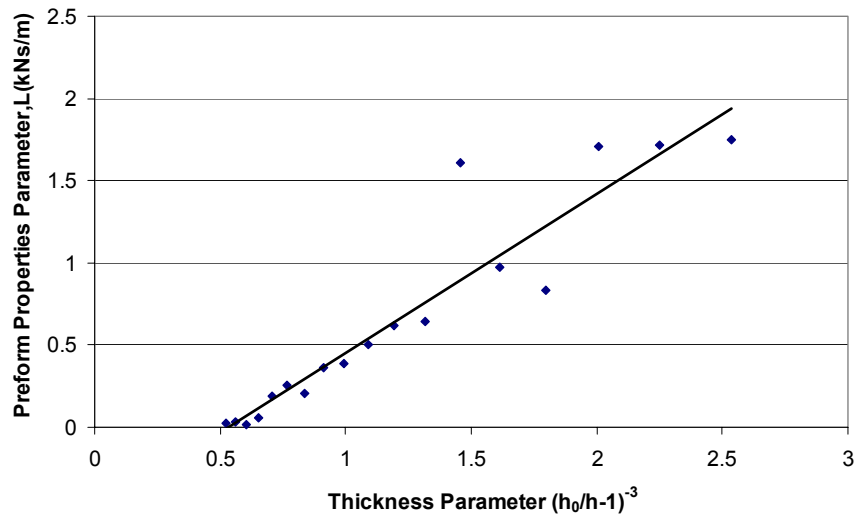


Figure 4-7 Plot of Preform Properties Parameter L against Thickness Parameter

Using an oil of significant viscosity increases substantially the complexity and duration of the experiment. To assess the possibility of using a low viscosity fluid (such as water) we compared a set of preliminary compaction tests at the slowest possible crosshead rate for both silicone oil and water. These results were sufficiently close to each other, that we chose for the final set of experiments to use water as the lubricating fluid. In selecting the deformation rate for the experiments we can use the equation to show that the force due to the effect of the flow of water is very small compared to the total force.

$$P_{tot} = P_{pre} + P_{flow} \quad (4.7)$$

Using water as the fluid ($\mu=1\text{mPas}$) with a test jig radius of 76.2mm, a cross head speed of 1mm/min, permeability of the order based on Carman-Kozenys equation with a constant of $2.19 \times 10^{-10} \text{ m}^2$ the effect of the water on the pressure over the range of measurements studied is less than 1%. Using a fluid of similar viscosity to a typical resin (100mPas) requires test speed of around 0.01mm/min to similarly limit the effect of the fluid on the compaction pressure.

4.3 Experimental Evaluation of Proposed Compaction Model

The primary experimental program involved compressing stacks of preforms in a hydraulic testing machine. The experimental set up is shown in Figure 4-8. The preforms were compressed between a 2.5cm thick, 25cm diameter aluminum disk and a support plate. The compaction forces were recorded using the machine load cell or a smaller independently recorded load cell (0-8.9KN) mounted between the cross head and the test plate.

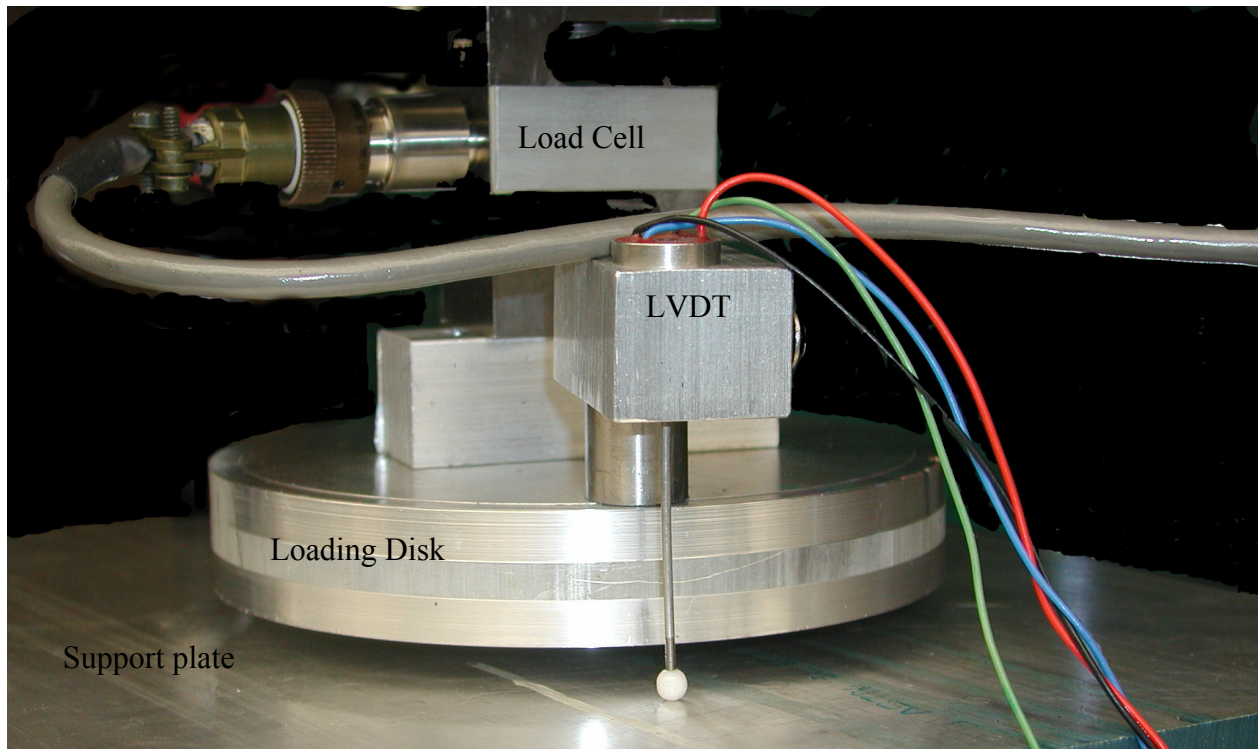


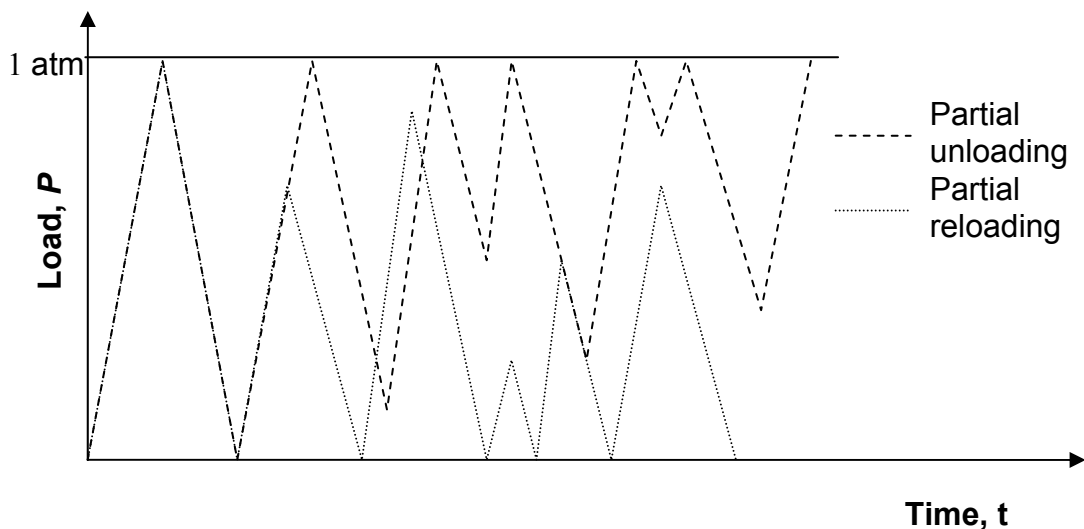
Figure 4-8 Test Jig, Load Cell and Linear Voltage Displacement Transducer

The preform thickness was recorded using a linear voltage displacement transducer (LVDT) recording the separation between the loading disk and the flat support plate. Using the machine cross-head displacement distorts the results significantly due to the small thickness of the specimens. The loading rate was chosen to be slow enough to minimize the time dependent effects observed. Two different fabrics were studied, a plain weave (PW) E-glass (7500 style) and a glass continuous filament mat (CFM, OCF8610). The plain weave fabric was compressed at a rate of 0.126mm/min, for the CFM the compression was carried out in stages as shown in Table 4.

Table 4 Cross-Head Rates for Compaction of Continuous Filament Mat

Load (N)	Load (lbf)	Rate (mm/min)	Rate (in/min)
>1345	>300	0.0254	0.001
890 to 1345	200 to 300	0.126	0.005
445 to 890	100 to 200	0.254	0.01
<445	<100	1.26	0.05

Two types of experiment were carried out, partial loading and partial unloading experiments. In both types, an initial loading cycle was used in which the fabric was loaded to 101KPa, immediately unloaded to the original thickness, and then reloaded to 101KPa. For the partial loading experiments the preform was fully unloaded, and subsequently a series of partial reloading cycles were carried out. For the partial unloading experiments the preform was unloaded to various intermediate states before reloading to full compaction. These cycles are shown graphically in Figure 4-9 .

**Figure 4-9 Schematic of Partial Unloading and Partial Reloading Cycles**

The plain weave was reloaded to the same thickness at each maximum load point, the CFM however, showed noticeable deformation at each cycle and was therefore loaded to a slightly increased thickness. To limit systematic errors in the measurements, the intermediate unloading points were not sequential.

Lubricated preforms were saturated with water. Preliminary experiments indicated no difference in the results between water and viscous oil (silicone oil 0.2Pas) when the tests with oil were conducted sufficiently slowly. The benefit of using water is that the viscosity is sufficiently low that no significant fluid pressure is developed in the water during testing. This removes the need to correct for the fluid pressure developed as is required when a higher viscosity fluid is used [42].

4.3.1 Comparison with Experimental Results.

The experimental testing was carried out using a 16 ply preform of the plain weave fabric and a 4 ply preform of the CFM. The preforms were loaded in a hydraulic testing machine, at the loading rates shown in Table 4 for the CFM and 0.126mm/min for the plain weave to an applied pressure of 1atm. The preform was then unloaded completely, reloaded to 1 atm, and then subsequently unloaded to several intermediate pressures, on each unloading it was reloaded to 1 atm. The envelope curves were fitted to several models and the most suitable models were selected. The fitting constants used for the plain weave fabric are shown in Table 5 and for the CFM in Table 6. As noted before the CFM data was affected by small changes in the compressed thickness at maximum applied compression, and therefore the volume fraction data is not shown in the table.

Table 5 Parameters Used for Envelope Curves for Plain Weave

	Gutowski				Robitaille				Power	
	Loading		Unloading		Loading		Unloading		Unloading	
	Wet	Dry	Wet	Dry	Wet	Dry	Wet	Dry	Wet	Dry
m	4	4	12	10	20.5	20.5	60	40	-1.7	-2.0
α_0	0.776	0.811	0.776	0.811	0	0	0	0	0.776	0.811
α_a	1.28	1.25	1.28	1.25	Infinite				1.02	1.02
V_f^*	46.8 %	44.8%	46.8%	44.8%	46.8 %	44.8 %	46.8 %	44.8%	46.8%	44.8%
V_f^0	36.3 %	36.3%	36.3%	36.3%	0	0	0	0	36.3%	36.3%
V_f^a	60%	56%	60%	56%	Infinite				47.5%	45.7%

The envelope curves for the plain weave fabric are shown in Figure 4-10 (dry) and Figure 4-11(wet). The envelope curves shown indicate that the Gutowski and Robitaille models both fit the loading curves for the plain weave fabric fairly well, however neither can be made to fit the unloading behavior well without substantial modification. The main difficulty being the initial slope at the start of unloading, which is considerably steeper than either model. This is not surprising since both models were developed to model the loading behavior only. For the unloading behavior the best fit was obtained using the empirical power law from Eqn (3.15).

Plain Weave Glass (7500 style) Envelope Models (Dry)

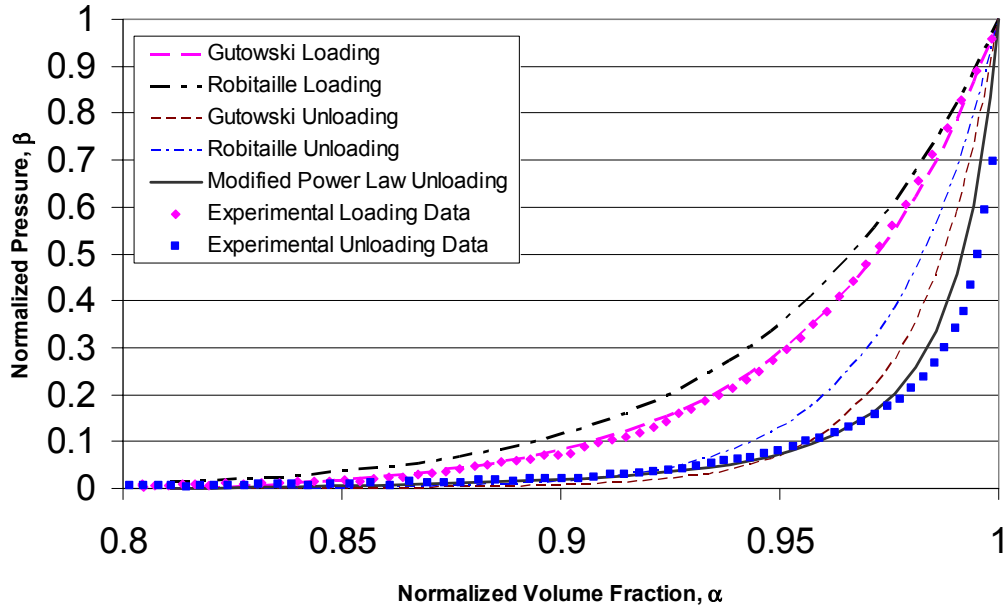


Figure 4-10 Loading and Unloading Envelopes for Dry Plain Weave (7500 style)

Plain Weave Glass (7500 style) Envelope Models (Wet)

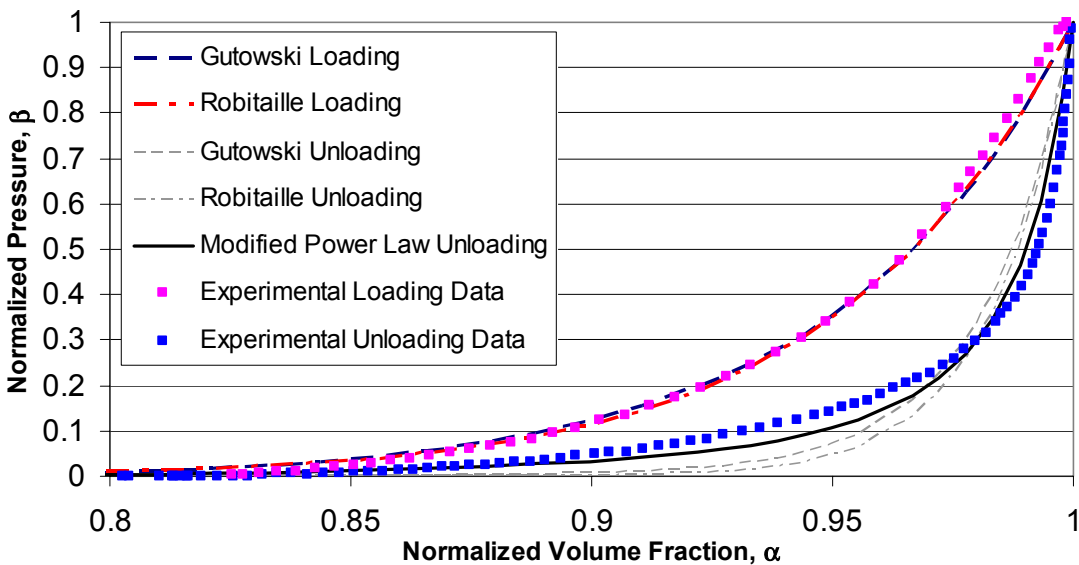


Figure 4-11 Loading and Unloading Envelopes for Wet Plain Weave (7500 style)

We do note however that while the V_f^a values for the Gutowski model are physically realistic for this fabric, the equivalent values used in the Empirical Power law model have no physical meaning, and must be separately fitted. It would be possible to improve the fit of the models by also adjusting the value of V_f^0 for the power law model, however this seemed unreasonable, since this parameter value has a physical meaning in all the models investigated.

The same comparisons also hold for the CFM material, though the viscoelastic behavior, which is ignored in this analysis, does distort the results somewhat.

Table 6 Parameters Used for Envelope Curves for Continuous Filament Mat (CFM, OCF8610)

	Gutowski				Robitaille				Power	
	Loading		Unloading		Loading		Unloading		Unloading	
	Wet	Dry	Wet	Dry	Wet	Dry	Wet	Dry	Wet	Dry
m	4	4	12	10	20.5	7	60	20	-2.0	-2.0
α_0	0.224	0.224	0.224	0.224	0	0	0	0	0.14	0.224
α_a	1.49	2.04	1.49	2.04	Infinite				1.05	1.05

Continuous Filament Mat Envelope Models (dry)

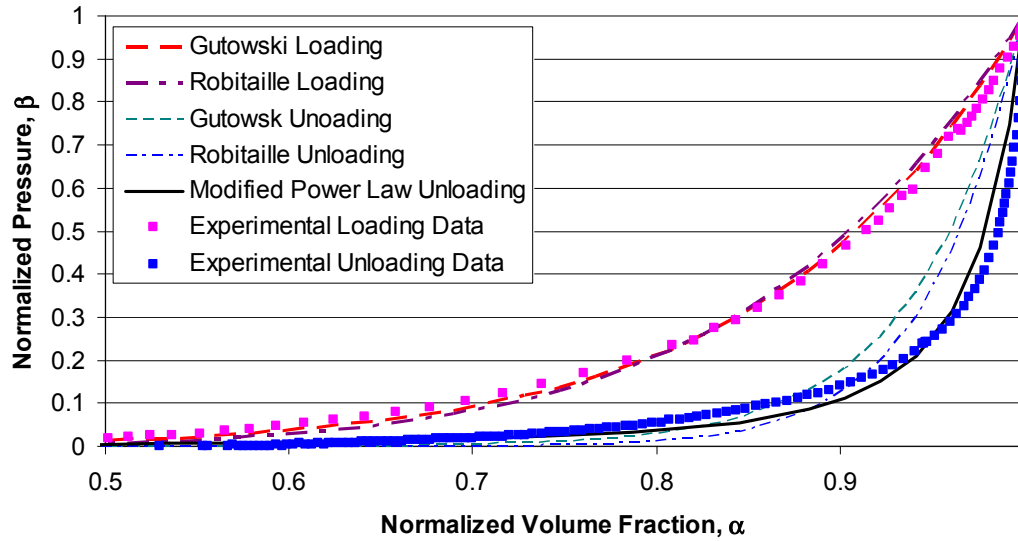


Figure 4-12 Loading and Unloading Envelopes for Unlubricated (dry) Continuous Filament Mat

Continuous Filament Mat Envelope Models (wet)

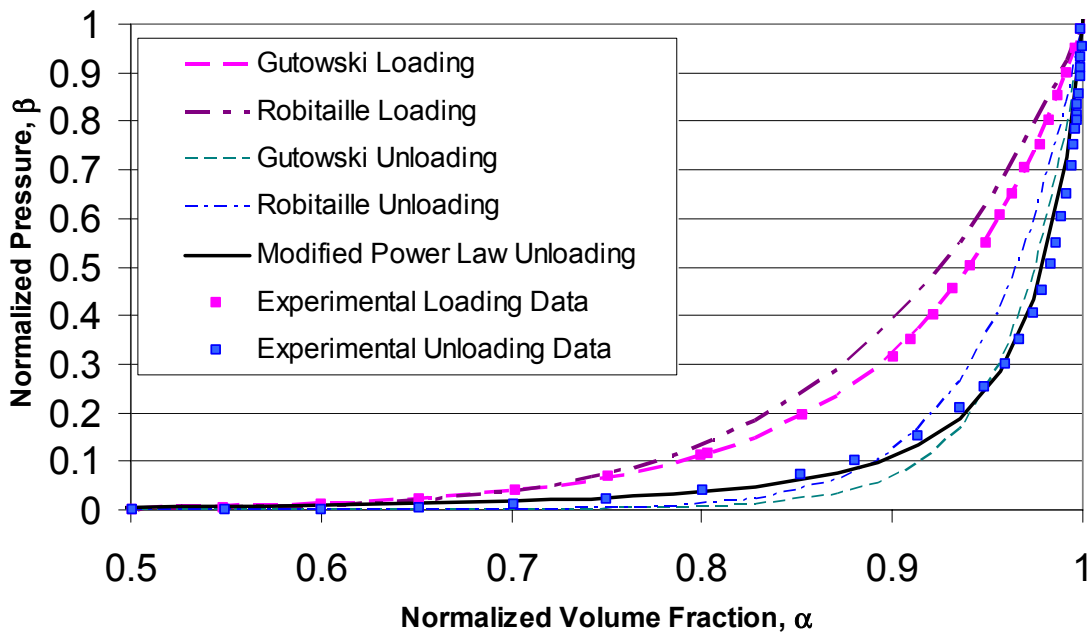


Figure 4-13 Loading and Unloading Envelopes for Lubricated (wet) Continuous Filament Mat

Having established the unloading and loading envelope behaviors we can now investigate the effectiveness of the proposed interpolation model for the intermediate loading conditions. The following figures show the partial reloading behavior for the two fabrics in the two conditions along with the modeled envelope curves and the interpolated model.

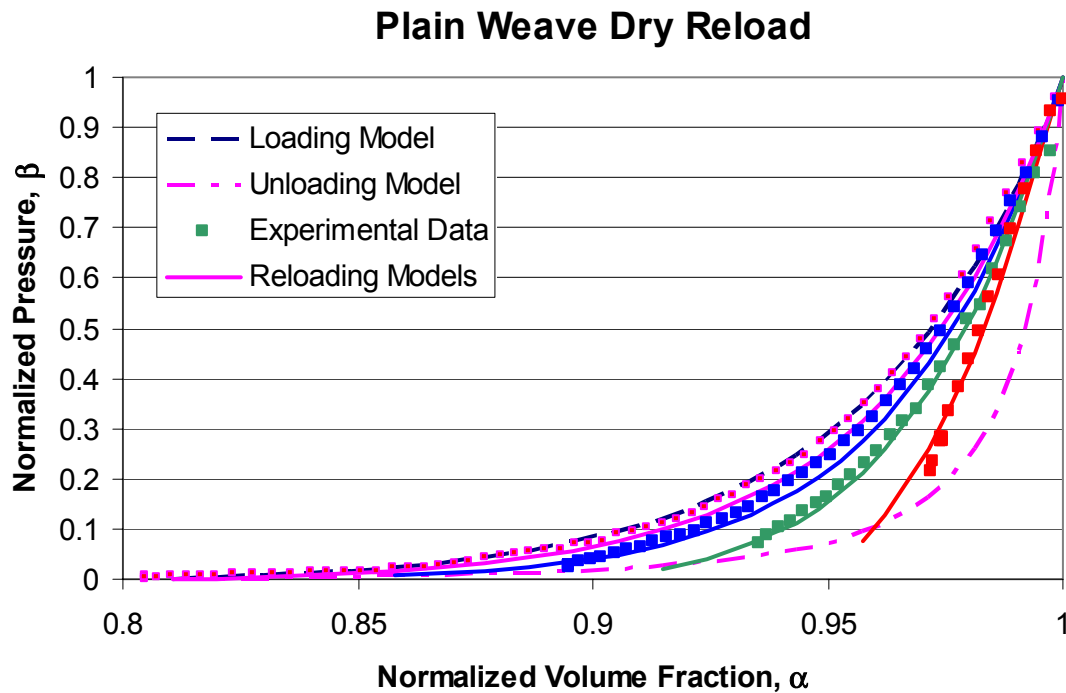


Figure 4-14 Behavior of Dry (Unlubricated) Plain Weave on Reloading after Partial Unloading

In Figure 4-15 the partial unloading curves for lubricated 16 Ply plain weave preforms are shown.

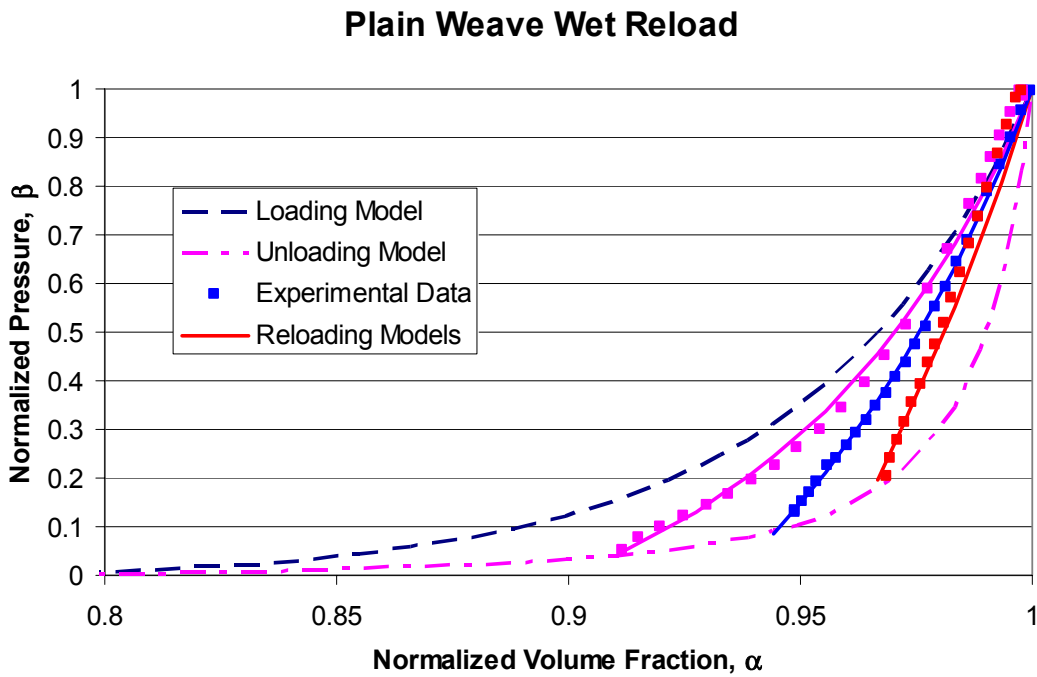


Figure 4-15 Behavior of Wet(Lubricated) Plain Weave Fabric on Reloading from Partial Unloading

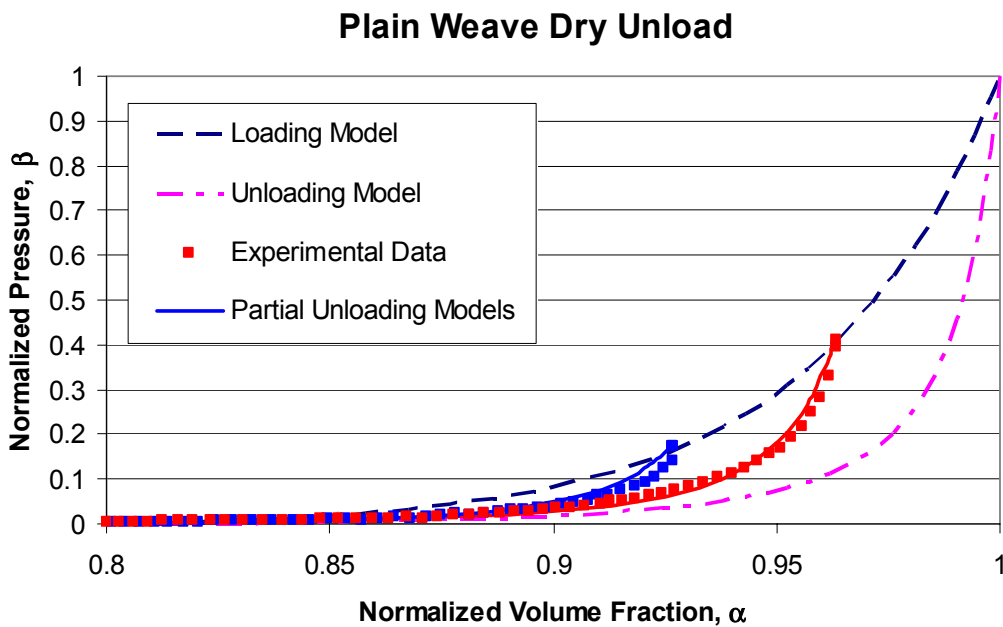


Figure 4-16 Behavior of Dry (Unlubricated) Plain Weave on Unloading from Partial Loading

The data shown here for the lubricated preform also show very good agreement with this empirical model.

For CFM the results shown in Figure 4-17 through 4-21 still show the same behavior we have seen in the plain weave, in particular the reloading curves form a non-intersecting family of curves.

Comparing a selection of these data to the interpolation model we can see some divergence from the model here, although once again the interpolation gives much better results than relying on the unloading or loading models alone.

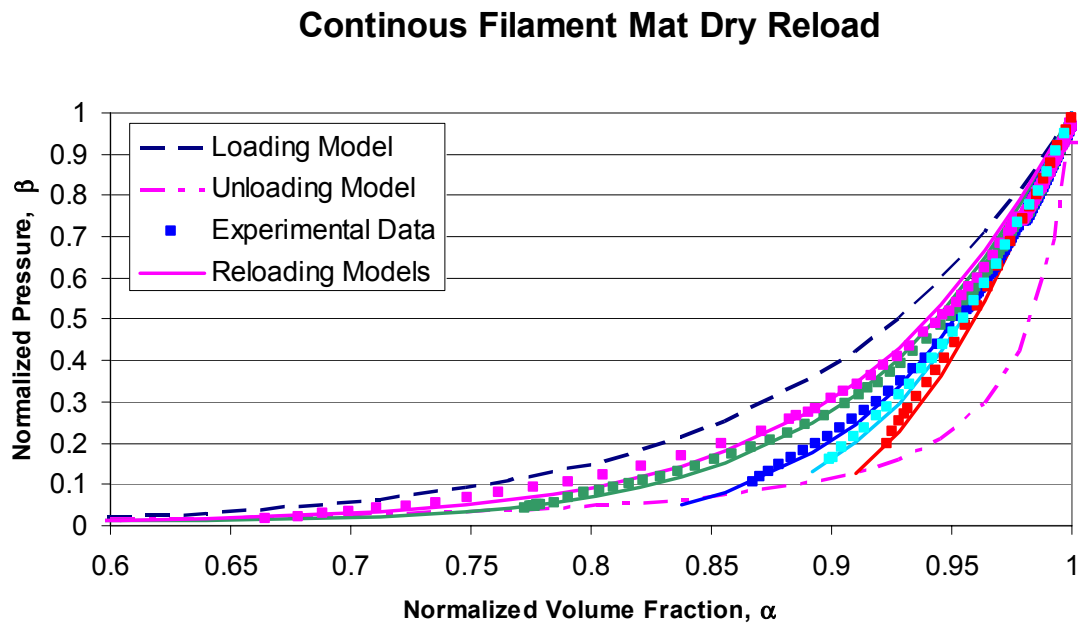


Figure 4-17 Behavior of Dry (Unlubricated) Continuous Filament Mat on Reloading after Partial Unloading

Continuous Filament Mat Wet Reload

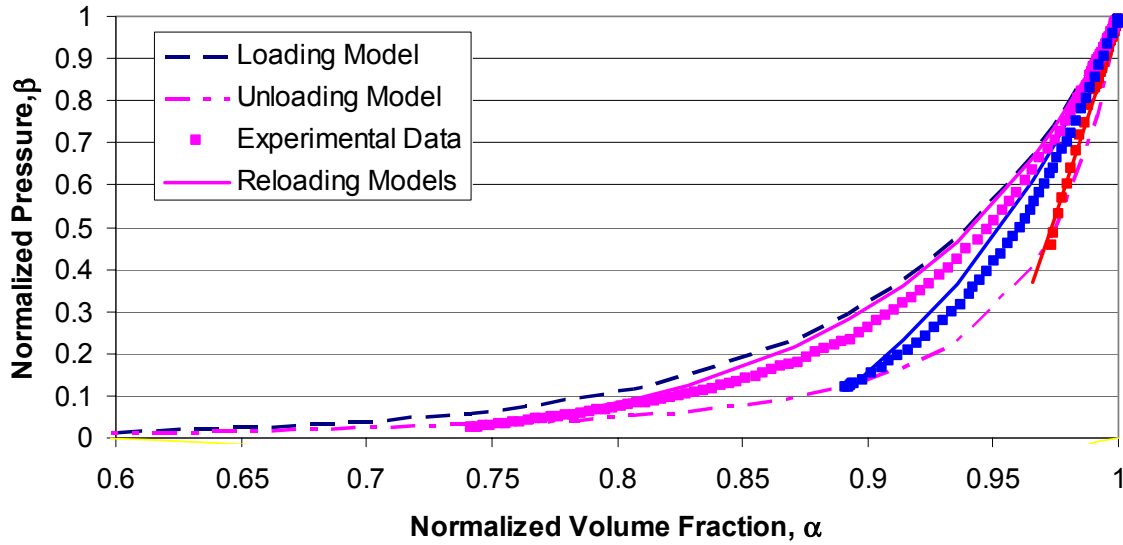


Figure 4-18 Behavior of Wet (Lubricated) Continuous Filament Mat on Reloading after Partial Unloading

Continuous Filament Mat Dry Unload

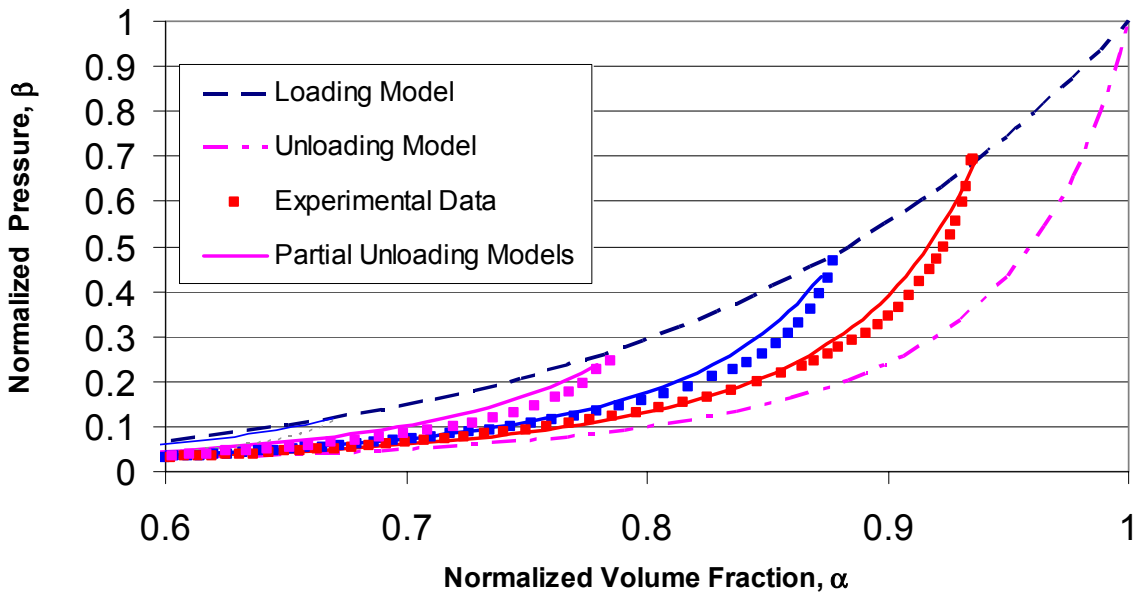


Figure 4-19 Behavior of Dry (Unlubricated) Continuous Filament Mat on Unloading after Partial Loading

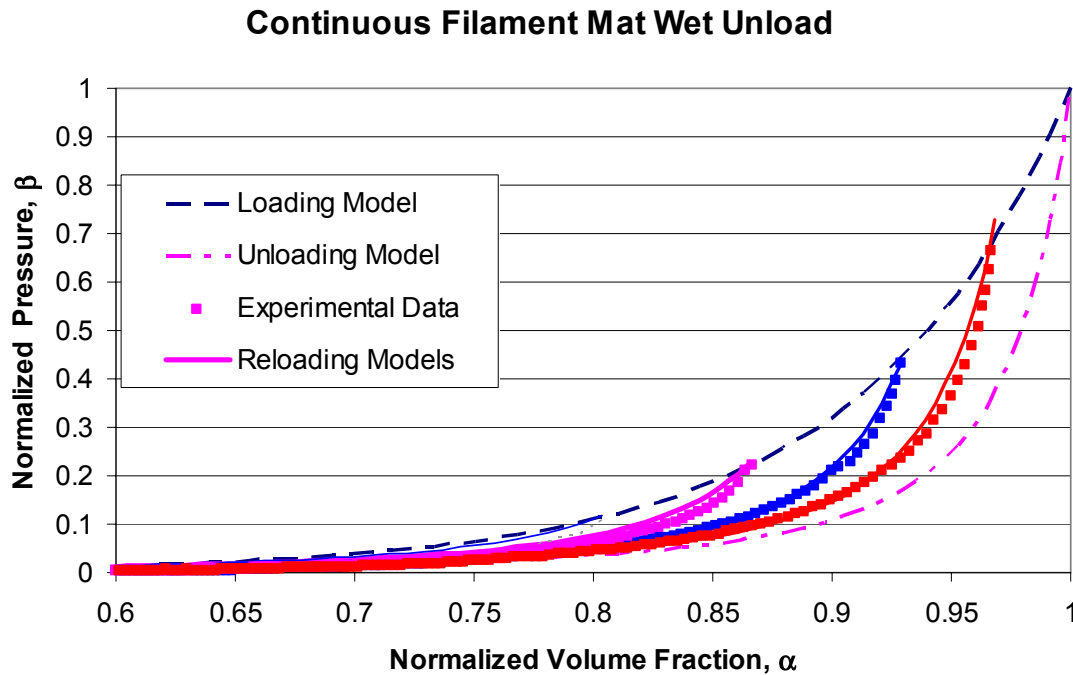


Figure 4-20 Behavior of Wet (Lubricated) Continuous Filament Mat on Unloading after Partial Loading

4.3.2 Compaction Model Conclusions

The compaction models developed in section 3 provide an acceptable fit for the data measured on the hydraulic testing machine (Instron), and provide a significantly better model for the compaction behavior than the models typically described in the literature. Most VARTM flow models described in the literature, if they specify the compaction model at all, simply refer to the unloading behavior of the wet preform. It is immediately apparent from Figure 4-21 that if the incorrect unloading model is used the thickness data will be very poorly reproduced, since an unloading curve taken from a higher initial loading pressure will fall entirely outside the envelope curve for a lower initial pressure.

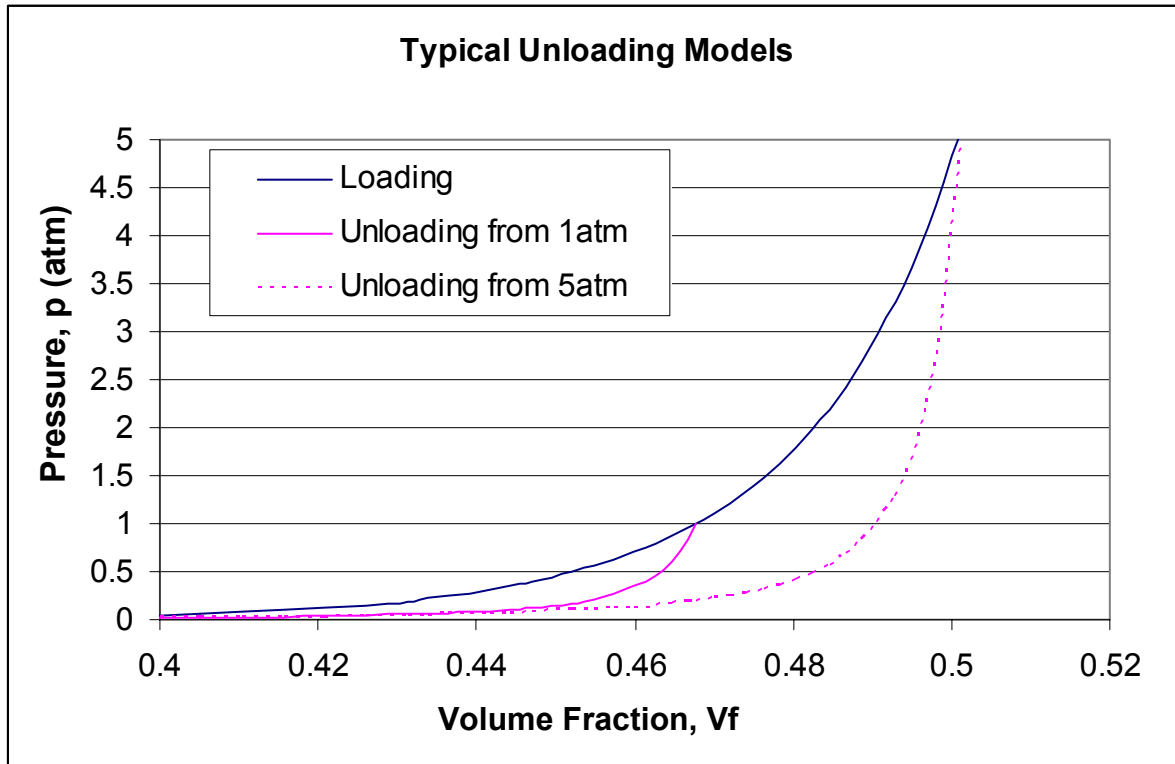


Figure 4-21 Schematic of Unloading Curves for Unloading from 1atm and 5atm Compaction

5 Flow modeling

5.1 Background

Chapter 2.3 describes some of the underlying transport phenomena typically used in modeling VARTM. Most models are based on Darcy's law, Eqn (2.1), which as noted in chapter 2 was experimentally derived. Pillai [4, 43, 44] showed how Darcy's law can be derived from the fundamental momentum equation for fluid flow, through the application of volume averaging theories and by making certain assumptions relating to the flow length scales. Pillai also developed a form of the continuity equation for dual scale porous media however in its development he did not consider the effect of a deforming preform and a modification of his argument is presented here including the appropriate features required to describe the preform deformation.

5.2 Notation and Volume Averaging theorems

ρ	Density
\mathbf{v}	Velocity
A_{jk}	Surface separating volumes j and k
\mathbf{n}_{jk}	Unit normal to surface A_{jk} pointing into volume k
\mathbf{u}_{jk}	Velocity of surface A_{jk} (n.b. for simplicity subscripts dropped for \mathbf{u}_{it} i.e. $\mathbf{u} = \mathbf{u}_{it}$)
p	Pressure
$\boldsymbol{\sigma}$	Stress
\mathbf{b}	body force per unit mass (gravity)

5.3 Definition of Volume Elements

Woven preforms consist of large (0.3-3mm) tows interspersed by gaps, whose size depends on the nature of the preforming process, and on the degree of compression to which the preform is subjected. Considering a point at position \mathbf{x} , the elementary volume Ω surrounding the point can be subdivided into superposed volumes:

Ω_f The volume occupied by solid fibers

Ω_r The volume within the tows filled with resin

Ω_p The volume within the tows not occupied by fibers or resin

Ω_R The interstitial volume between the tows filled with resin

Ω_v The interstitial volume not filled by resin

(These subscripts will be used throughout to distinguish variables related to specific volumes)

$\Omega_t = \Omega_f + \Omega_r + \Omega_p$ The tow volume

$\Omega_i = \Omega_R + \Omega_v$ The interstitial volume

$\Omega = \Omega_t + \Omega_i = \Omega_f + \Omega_r + \Omega_p + \Omega_R + \Omega_v$

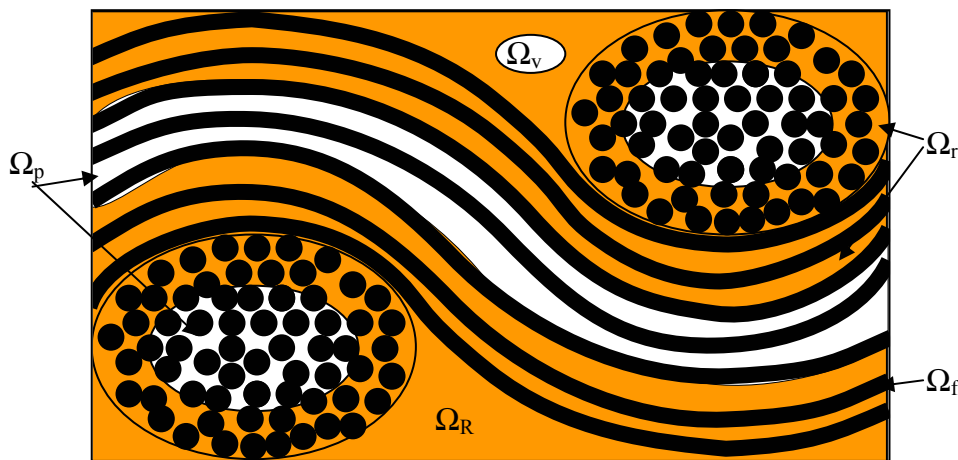


Figure 5-1 Multi-Scale Structure of Unit Cell

To describe the flow we will typically use a macro scale at which the inhomogeneities shown in Figure 5-1 are averaged. The microscale for the flow model development will be at the tow level and the flows at the subtow level will be calculated analytically and introduced as sink/source terms. To describe the macro and micro scale requires some form of volume averaging. For instance, to describe the motion of fibers it is important to recognize that the fibers do not exist at every point within the unit cell, however in our continuum approximation equations may be required which treat field variables related to the fiber as continuous. To do this requires some systematic method for averaging field variables over the volume. The method we use is a form of integral averaging described in detail by Gray et al. [15].

5.3.1 Integral Averaging Theories

Consider a representative volume element (RVE) Ω , surrounding point \mathbf{x} , enclosed by a surface A with outward pointing normal vector \mathbf{n} . A representative volume element is an element sufficiently large that it contains a representative sample of the material at the length scale of interest. First we introduce a generalized function

$$\gamma_j = \begin{cases} 1 & \text{within } \Omega_j \\ 0 & \text{elsewhere in } \Omega \end{cases} \quad (5.1)$$

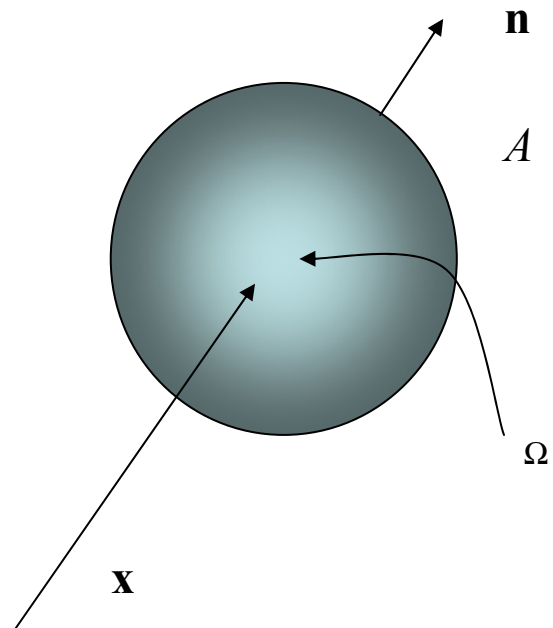


Figure 5-2 Representative Volume Element

The generalized function is a convenient way of subdividing a volume for integral operations.

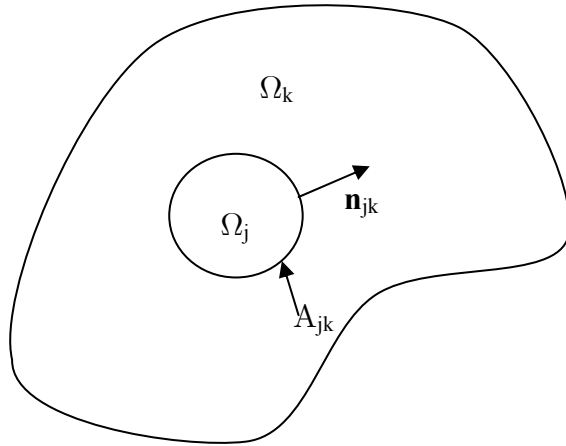


Figure 5-3 RVE Sub-element Notation

By multiplying a field variable by the generalized function and then integrating over the entire volume, we can calculate the integral of the variable over the relevant sub element, for example the mass of fiber within the RVE is

$$M_f = \int_{\Omega_f} \rho dV = \int_{\Omega} \rho \gamma_f dV = \langle \rho_f \rangle \int_{\Omega} dV \quad (5.2)$$

Where $\langle \rho_f \rangle$ is the material density within the fiber sub-volume averaged over the RVE. The benefit of this type of averaging is that it becomes possible to convert an integral over a changing sub volume into an integral over a static RVE. In calculating the average of a field variable over the RVE we need to consider carefully how that average will be used. (As an additional notation

shorthand $\phi_j = \gamma_j \phi$.) The following averages of the generic field variable ϕ may be used. The

average value of ϕ over the RVE

$$\langle \phi \rangle = \frac{1}{\Omega} \int_{\Omega} \phi dV \quad (5.3)$$

ϕ within the sub-volume Ω_j averaged over the entire REV

$$\langle \phi_j \rangle = \frac{1}{\Omega} \int_{\Omega_j} \phi dV = \frac{1}{\Omega} \int_{\Omega} \phi \gamma_j dV = \frac{1}{\Omega} \int_{\Omega} \phi_j dV \quad (5.4)$$

ϕ within the sub-volume Ω_j averaged over the sub-volume Ω_j .

$$\langle \phi_j \rangle^j = \frac{1}{\Omega_j} \int_{\Omega_j} \phi dV = \frac{1}{\Omega_j} \int_{\Omega} \phi \gamma_j dV = \frac{\Omega}{\Omega_j} \langle \phi_j \rangle = \frac{1}{V_j} \langle \phi_j \rangle \quad (5.5)$$

Where V_j is the volume fraction of a sub volume j

$$V_j = \frac{\int_{\Omega_j} dV}{\int_{\Omega} dV} = \frac{\Omega_j}{\Omega} \quad (5.6)$$

5.4 Mass Balance (Continuity)

The microscopic continuity equation is used as the basis of the macroscopic averaged continuity equation used in developing the flow equations

$$\frac{\partial \rho}{\partial t} + \nabla \cdot (\rho \mathbf{v}) = 0 \quad (5.7)$$

Integrating this over the interstitial volume and assuming that the rate of change of resin density is constant within the interstitial volume yields

$$\underbrace{\frac{\partial \rho}{\partial t} \Omega_i}_{\text{Effect of Changes in Resin Density}} + \underbrace{\int_{\Omega} \rho \nabla \cdot (\rho \mathbf{v}) dV}_{\text{Resin Flux Out of Interstitial SubVolume}} = 0 \quad (5.8)$$

Using results from Gray et al [15] we can show

$$\underbrace{\frac{\partial \rho}{\partial t} \Omega_i}_{\text{Effect of Changes in Resin Density}} + \underbrace{\Omega \nabla \cdot \langle \rho_i \mathbf{v}_i \rangle}_{\text{Macroscopic Resin Divergence}} - \underbrace{\int_{A_i} \rho_i \mathbf{v}_i \cdot \mathbf{n}_{ti} dV}_{\text{Resin Flux at Boundary Between Tow and Interstitial Sub-Volumes}} = 0 \quad (5.9)$$

Pillai assumed that the tow surfaces were stationary, and hence the third term represented flows of resin into the tows. If, however, we allow for the tows to be moveable (as is the case in a deformable preform) the flow of resin into the tow is $\mathbf{v}_i - \mathbf{v}_t$ and the third term is split into two separate physical phenomena

$$\frac{\partial \rho}{\partial t} \Omega_i + \Omega \nabla \cdot \langle \rho_i \mathbf{v}_i \rangle - \underbrace{\int_{A_i} \rho_i (\mathbf{v}_i - \mathbf{v}_t) \cdot \mathbf{n}_{ti} dV}_{\text{Resin Flux into Tow}} + \underbrace{\int_{A_i} \rho_i \mathbf{v}_t \cdot \mathbf{n}_{ti} dV}_{\text{Rate of Change of Size of Interstitial Volume}} = 0 \quad (5.10)$$

This can be rewritten

$$\frac{\partial}{\partial t}(\rho_i \Omega_i) + \Omega \nabla \cdot \langle \rho_i \mathbf{v}_i \rangle - \int_{A_{it}} \rho_i (\mathbf{v}_i - \mathbf{v}_t) \cdot \mathbf{n}_{it} dV = 0 \quad (5.11)$$

which for an incompressible resin becomes

$$\nabla \cdot \langle \mathbf{v}_i \rangle - \int_{A_{it}} (\mathbf{v}_i - \mathbf{v}_t) \cdot \mathbf{n}_{it} dV + \frac{\partial V_i}{\partial t} = 0 \quad (5.12)$$

We can therefore define a resin sink per unit volume

$$S = \frac{1}{\Omega} \int_{A_{it}} (\mathbf{v}_i - \mathbf{v}_t) \cdot \mathbf{n}_{it} dA \quad (5.13)$$

And the continuity equation becomes

$$\nabla \cdot \langle \mathbf{v}_i \rangle = S - \frac{\partial V_i}{\partial t} \quad (5.14)$$

If we neglect the deformation of the preform and the sink term due to dual scale flow we recover the steady form of the single scale continuity equation used in RTM and in most of the published VARTM models.

$$\nabla \cdot \langle \mathbf{v}_i \rangle = 0 \quad (5.15)$$

The justification for the pseudo steady assumption is that the rate deformation is slow compared to the flow velocities, and whilst this may be true in some cases for a part of the domain, it is certainly not reasonable near the flow front, where the effect of preform lubrication can result in a

rapid change in the preform thickness. In addition, use of this continuity equation will not subsequently allow the modeling of preform consolidation after the end of the infusion, where the source of resin for any flow to take place is the change in thickness of the preform.

5.5 Macroscopic Momentum Equation

The microscopic momentum equation for fluid flow is:

$$\frac{\partial}{\partial t}(\rho \mathbf{v}) + \nabla \cdot (\rho \mathbf{v} \mathbf{v}) = \nabla \cdot \boldsymbol{\sigma} + \rho \mathbf{b} \quad (5.16)$$

Following the standard practice for preform infusion we will assume that the flow rate is slow enough that the inertial terms are small (i.e. we are assuming that the Reynolds number is small).

$$\nabla \cdot \boldsymbol{\sigma} + \rho \mathbf{b} = 0 \quad (5.17)$$

In carrying out volume averaging Pillai demonstrates that the fluid pressure in the pores must be balanced by the viscous drag forces due to the resin flow past the tows [4, 44].

$$-V_i \nabla \langle p_i \rangle^i = \mathbf{f}_d \quad (5.18)$$

The drag forces should be proportional to the relative velocity of the resin with respect to the preform, and the resin viscosity, and should be inversely proportional to the permeability. To find the appropriate averaged values for this we note that the drag forces should be indifferent to the frame of calculation. The averaged measure we use to ensure this is

$$\underbrace{\langle \mathbf{v}_i \rangle^i}_{\text{Interstitial Resin Velocity Averaged Over the Interstitial Volume}} - \underbrace{\langle \mathbf{v}_t \rangle^t}_{\text{Tow Velocity Averaged Over the Tow Volume}} \quad (5.19)$$

This leads to

$$-V_i \nabla p = \frac{f(V_i) \mu}{l^2} \{ \langle \mathbf{v}_i \rangle^i - \langle \mathbf{v}_t \rangle^t \} \quad (5.20)$$

where $f(V_i)$ is some function of the interstitial volume fraction and l is a characteristic length scale in the porous medium. Since we will use conventional models for permeability, the final version of Darcy's law used here is

$$\begin{aligned} -\nabla p &= \mu \mathbf{K}^{-1} \tilde{\mathbf{q}} \\ \langle \mathbf{v}_i \rangle &= -\frac{\mathbf{K}}{\mu} \nabla p + V_i \langle \mathbf{v}_t \rangle^t \end{aligned} \quad (5.21)$$

(where the definition of $\tilde{\mathbf{q}}$ is given in Eqn (2.8))

5.5.1 Final Form of Governing Equation

Combining equations (5.14) and (5.21) we generate the final version of the 3-D governing equation

$$\nabla \cdot \left(-\frac{K}{\mu} \nabla p + V_i \langle \mathbf{v}_t \rangle^t \right) = S - \frac{\partial V_i}{\partial t} \quad (5.22)$$

This can be rewritten in terms of macroscopic measured variables

$$\nabla \cdot \left(\frac{K}{\mu} \nabla p - V_i \mathbf{u} \right) = \frac{\partial V_i}{\partial t} - S \quad (5.23)$$

where \mathbf{u} is the macroscopic preform velocity.

5.6 Sink Term Derivation

The sink term in the macroscopic mass balance equation comes from equation (5.13). This is the rate of resin flowing into the resin tows from the interstitial spaces per unit of elementary volume.

$$S = \frac{1}{\Omega} \int_{A_{it}} (\mathbf{v}_i - \mathbf{u}) \cdot \mathbf{n}_{it} dA = -\frac{1}{\Omega} \frac{\partial}{\partial t} \Omega_r \quad (5.24)$$

The flow of resin into the tow can be conveniently expressed in terms of the rate of change of tow saturation V_{sat} where

$$V_{sat} = \frac{\Omega_r}{\Omega_p + \Omega_r} = \frac{\Omega_r}{\Omega_t - \Omega_f} \quad (5.25)$$

since in this model the tow volume ($\Omega_t = \Omega_r + \Omega_p + \Omega_f$) is a constant and the fiber volume Ω_f is also constant

$$-S = \frac{\Omega_t - \Omega_f}{\Omega} \frac{\partial V_{sat}}{\partial t} = (V_t - V_f) \frac{\partial V_{sat}}{\partial t} = V_f \left(\frac{V_t}{V_f} - 1 \right) \frac{\partial V_{sat}}{\partial t} \quad (5.26)$$

This form of the saturation rate is convenient when the volume fraction of the tows remains constant during deformation, as we assume it does, since we now only have to consider the rate of infiltration of the tows.

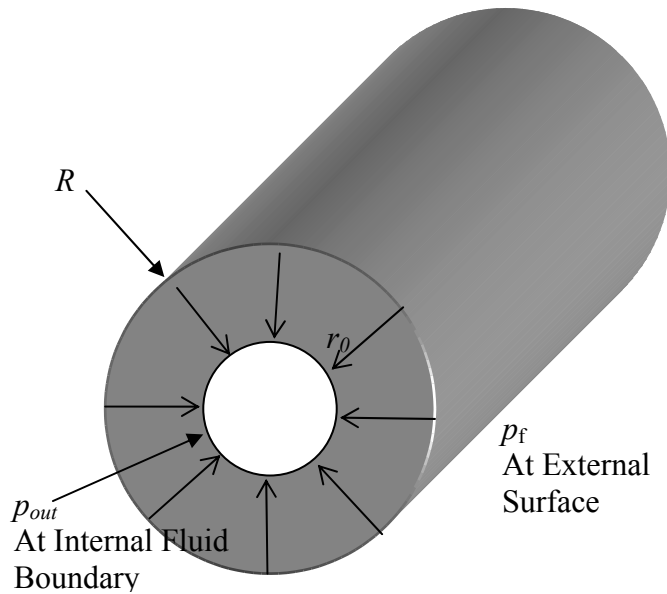


Figure 5-4 Tow Infiltration Model

The simplest model for tow saturation assumes that the tow is infiltrated radially inwards from the surface as shown in Figure 5-4. The pressure at the outer surface of the tow (at radius R) is considered to be uniform (p_f) and the pressure at the microscopic flow front (at radius r_0) within the tow is considered to be equal to the vent pressure (p_{out}).

The pressure gradients can be calculated from a cylindrical polar form of the single scale flow equation

$$\frac{1}{r} \frac{\partial}{\partial r} \left(r \frac{\partial p}{\partial r} \right) = 0 \quad (5.27)$$

We apply the boundary conditions $p(R) = p_f$, $p(r_0) = p_{out} = 0$ and solve for p

$$p = (p_f - p_{out}) \frac{\ln(r/R)}{\ln(R/r_0)} + p_f \quad (5.28)$$

Since tow saturation $V_{sat} = 1 - (r_0/R)^2$ the pressure gradient at the tow surface is

$$\left. \frac{\partial p}{\partial r} \right|_{r=R} = -\frac{2(p_f - p_{out})}{R \ln(1 - V_{sat})} \quad (5.29)$$

and the volume flow of resin into the tow

$$Q_r = -\frac{\Omega_t 2\pi R}{\underbrace{\pi R^2}_{\substack{\text{tow surface} \\ \text{area in REV}}}} \frac{2K_{tow}(p_f - p_{out})}{\mu R \ln(1 - V_{sat})} = -\Omega S \quad (5.30)$$

The sink term is therefore

$$S = \frac{V_t 4K_{tow}(p_f - p_{out})}{\mu R^2 \ln(1 - V_{sat})} \quad (5.31)$$

and from (5.26) the rate of change of tow saturation

$$\frac{\partial V_{sat}}{\partial t} = -\frac{V_t}{V_t - V_f} \frac{4K_{tow}}{\mu R^2} \frac{p - p_{out}}{\ln(1 - V_{sat})} = -\frac{C_{sat}}{\mu} \frac{p - p_{out}}{\ln(1 - V_{sat})} \quad (5.32)$$

Where C_{sat} is a function of the tow geometry, and is considered to be a constant in this model.

5.7 Computational Implementation

The computational discretization of the problem follows Patankar's [45] control volumes finite element method, and uses the same basic terminology. For the 1-D models the mesh is fixed in space and the domain is divided up into control volumes with a node at the center of each control volume. The values of variables are only calculated at each node point, and therefore where intermediate values are required they must be interpolated using a suitable assumption for the variation of the variable between the node points.

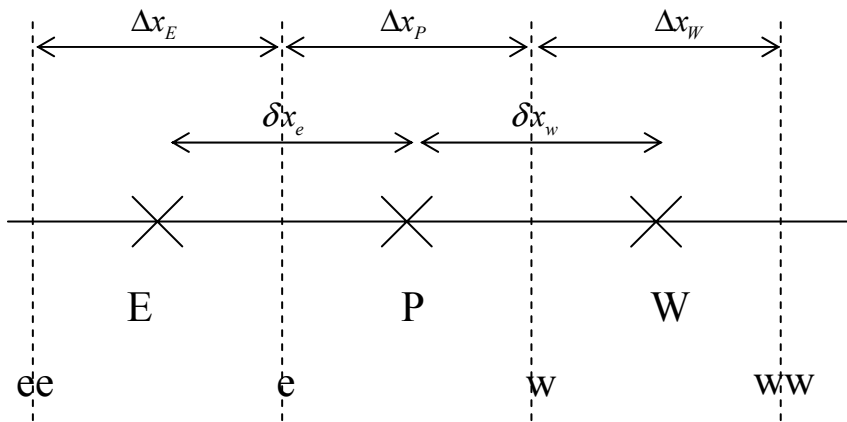


Figure 5-5 Node Line Terminology [45]

In developing a control volume finite element scheme to calculate the resin flow and preform compaction we will develop a discrete form of the governing equations discussed in section 5.5.1. For convenience we will typically show the discrete equation for a point P, at position x_p with nearest neighbors E and W, these upper case letters are used as subscripts to denote the value of a particular variable at that position. The values of variables at the control volume faces (denoted using lower case subscripts) are also required in the development of the discrete equation, although they are not used in the final form of the equations since they will not be calculated in the solution of the system of linear equations developed. The control volume around node P has length Δx_p , and the distance between nodes P and E is δx_e . The 1-D element is developed from the flow model by integrating the flow over the area of the control volume face. In the case of VARTM the governing equations for a fixed grid have no convective terms.

5.8 Discretization

5.8.1 1-D fixed mesh

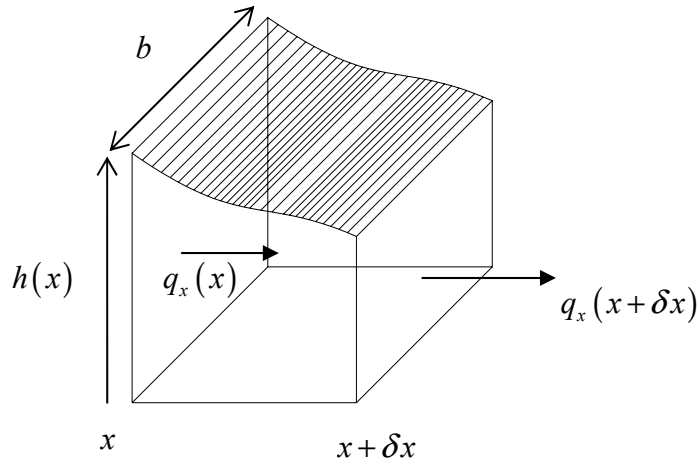


Figure 5-6 1-D Static Element

For the fixed mesh we define an element of fixed length Δx_p , of width b and thickness h (see Figure 5-6). We only consider elements behind the fluid flow front for the flow modeling, and we assume that the tow size remains constant during saturation of the tow, in which case the change in volume of the element is balanced by the resin flows in and out of the element and the flow of resin into the tows. (n.b. we are assuming here that the volume of fiber in this 1-D element remains constant.)

To develop a 1-D equation we integrate Eqn (5.23) over the width and thickness

$$\int_0^h \int_0^b \nabla \cdot \left(\frac{K_x}{\mu} \frac{\partial p}{\partial x} \hat{\mathbf{x}} + \frac{K_x}{\mu} \frac{\partial p}{\partial x} \frac{\partial h}{\partial x} \frac{z}{h} \hat{\mathbf{z}} - V_i \mathbf{u} \right) dy dz = \int_0^h \int_0^b \frac{\partial V_i}{\partial t} - S dy dz \quad (5.33)$$

(Note the direction of the fluid flow at the top surface of the preform dictates the relationship between the x component and the z component of the resin flow.)

The integration of Eqn (5.33) gives

$$h \frac{\partial}{\partial x} \left(\frac{K}{\mu} \frac{\partial p}{\partial x} \right) + \frac{K}{\mu} \frac{\partial p}{\partial x} \frac{\partial h}{\partial x} - V_i \frac{\partial h}{\partial t} = h \frac{\partial V_i}{\partial t} - Sh \quad (5.34)$$

which can also be written

$$\frac{\partial}{\partial x} \left(\frac{Kh}{\mu} \frac{\partial p}{\partial x} \right) = \frac{\partial}{\partial t} (hV_i) - Sh \quad (5.35)$$

noting that K is a function of thickness h , which is in turn a function of pressure p . Eqn (5.35) is equivalent to that derived by Acheson [46] however Acheson goes on to develop a non dimensional form of this equation which ignores the effective convection of saturation and thickness. Since $V_i = 1 - V_t$, substituting for S from Eqn (5.26) gives

$$\frac{\partial}{\partial x} \left(h \frac{K}{\mu} \frac{\partial p}{\partial x} \right) = \frac{\partial h}{\partial t} + hV_f \frac{1 - V_{flow}}{V_{flow}} \frac{\partial V_{sat}}{\partial t} \quad (5.36)$$

since $hV_f = h_0$ is a constant this becomes

$$\frac{\partial}{\partial x} \left(\frac{Kh}{\mu} \frac{\partial p}{\partial x} \right) = \frac{\partial h}{\partial t} + h_0 \frac{1 - V_{flow}}{V_{flow}} \frac{\partial V_{sat}}{\partial t} \quad (5.37)$$

Since the thickness variation is a non-linear function of the pressure it is convenient to expand the rate of change of thickness term by taking the time derivative of Eqn (3.24), applying the chain

rule and substituting $k_{sat} = h_0 \frac{1 - V_{flow}}{V_{flow}}$

$$\frac{\partial}{\partial x} \left(\frac{Kh}{\mu} \frac{\partial p}{\partial x} \right) = \frac{\partial p}{\partial t} \frac{\partial h}{\partial p} + \frac{\partial V_{sat}}{\partial t} \left\{ k_{flow} + \frac{\partial h}{\partial V_{sat}} \right\} \quad (5.38)$$

Integrating Eqn (5.38) over the control volume (i.e. from x_w to x_e) yields

$$\left[\frac{Kh}{\mu} \frac{\partial p}{\partial x} \right]_{x_w}^{x_e} = \int_{x_w}^{x_e} \frac{\partial p}{\partial t} \frac{\partial h}{\partial p} + \frac{\partial V_{sat}}{\partial t} \left\{ k_{tow} + \frac{\partial h}{\partial V_{sat}} \right\} dx \quad (5.39)$$

Treating the terms inside the integral on the right hand side as constant within the control volume, and assuming the pressure gradient is linear between nodes results in the following ‘semi-discrete’ form

$$\Gamma_e \left(\frac{p_E - p_P}{\delta x_e} \right) - \Gamma_w \left(\frac{p_P - p_W}{\delta x_w} \right) = \Delta x_P \left[\frac{\partial p_P}{\partial t} \left(\frac{\partial h}{\partial p} \right)_P + \frac{\partial V_{sat}}{\partial t} \left\{ k_{tow} + \frac{\partial h}{\partial V_{sat}} \right\} \right] \quad (5.40)$$

Where Γ is the diffusion co-efficient at the control volume boundary, calculated as the weighted harmonic mean of the diffusion coefficients calculated at the nodes on either side of the boundary.

$$\Gamma_e^{-1} = \left(\frac{\Delta x_P}{2\delta x_e} \left(\frac{\mu}{Kh} \right)_E + \left(1 - \frac{\Delta x_P}{2\delta x_e} \right) \left(\frac{\mu}{Kh} \right)_P \right) \quad (5.41)$$

If we indicate the current value of any variable as the variable with no superscript and the value at the previous timestep using a superscript 0, then by integrating over time from t^0 to $t^0 + \Delta t$ we get

$$\left(\frac{\Gamma_e}{\delta x_e} + \frac{\Gamma_w}{\delta x_w} \right) p_P - \frac{\Gamma_e}{\delta x_e} p_E - \frac{\Gamma_w}{\delta x_w} p_W = - \frac{\Delta x_P}{\Delta t} \left[\begin{aligned} & (p_P - p_P^0) \left(\frac{\partial h}{\partial p} \right)_P + \\ & (V_{sat} - V_{sat}^0) \left\{ k_{tow} + \frac{\partial h}{\partial V_{sat}} \right\} \end{aligned} \right] \quad (5.42)$$

(Here we are assuming that the values of the right hand side, $\left\{ k_{tow} + \frac{\partial h}{\partial V_{sat}} \right\}$ and $\left(\frac{\partial h}{\partial p} \right)_P$ do not change significantly during the time step .)

If we linearize the source term in Eqn (5.42) we get

$$\left(\frac{\Gamma_e}{\delta x_e} + \frac{\Gamma_w}{\delta x_w} + \frac{\Delta x_P}{\Delta t} \left(\frac{\partial h}{\partial p} \right)_P - S_P \right) p_P - \frac{\Gamma_e}{\delta x_e} p_E - \frac{\Gamma_w}{\delta x_w} p_W = \frac{\Delta x_P}{\Delta t} \left(\frac{\partial h}{\partial p} \right)_P p_P^0 + S_C \quad (5.43)$$

$$S_C + S_P p_P = -\frac{\Delta x_P}{\Delta t} (V_{sat} - V_{sat}^0) \left\{ k_{tow} + \frac{\partial h}{\partial V_{sat}} \right\}$$

Using Patankar's iterative scheme to solve these equations we will require $S_P \leq 0$ to ensure that the coefficient of p_P remains unconditionally positive.

5.8.2 Updating the Tow Saturation

The tow saturation updating for the first time step is calculated by integrating Eqn (5.32) over a time period $t=0$ to $t=\Delta t$ and assuming that over that period the pressure increases linearly from 0 at the start of the time step to the updated pressure p at the end of the time step.

$$\int_0^{\Delta t} \ln(1 - V_{sat}) \frac{\partial V_{sat}}{\partial t} dt = -\frac{C_{sat}}{\mu} \int_0^{\Delta t} \frac{tp}{\Delta t} dt \quad (5.44)$$

From this we can show

$$(1 - V_{sat}) \ln(1 - V_{sat}) + V_{sat} = \frac{C_{sat} p \Delta t}{2\mu} \quad (5.45)$$

For small values of V_{sat} we can therefore approximate

$$V_{sat}^2 \approx \frac{C_{sat} p \Delta t}{2\mu} \quad (5.46)$$

For subsequent updates we will use

$$V_{sat} = V_{sat}^0 - \Delta t \frac{C_{sat}}{\mu} \frac{p}{\ln(1 - V_{sat}^0)} \quad (5.47)$$

(which cannot be used for the first update as it would result in a singularity). The linearized source terms in Eqn(5.43) are therefore

$$\left. \begin{aligned} S_C &= -\Delta x_P \sqrt{\frac{1}{\Delta t \mu} \frac{C_{sat} P_p^*}{2}} \left[k_{tow} + \frac{\partial h}{\partial V_{sat}} \right] \\ S_P &= 0 \end{aligned} \right\} V_{sat}^0 = 0,$$

$$\left. \begin{aligned} S_C &= \frac{\Delta x_P}{\mu} \frac{C_{sat} P_p^*}{\ln(1 - V_{sat}^0)} \left[k_{tow} + \frac{\partial h}{\partial V_{sat}} \right] \\ S_P &= 0 \end{aligned} \right\} V_{sat}^0 > 0, \left[k_{tow} + \frac{\partial h}{\partial V_{sat}} \right] < 0 \quad (5.48)$$

$$\left. \begin{aligned} S_C &= 0 \\ S_P &= \frac{\Delta x_P}{\mu} \frac{C_{sat}}{\ln(1 - V_{sat}^0)} \left[k_{tow} + \frac{\partial h}{\partial V_{sat}} \right] \end{aligned} \right\} V_{sat}^0 > 0, \left[k_{tow} + \frac{\partial h}{\partial V_{sat}} \right] \geq 0$$

where the superscript asterisk indicates the pressure value at the previous iteration of the non-linear iterative solution method.

5.8.3 Thickness Term

Five models were evaluated for the change in thickness

- Model 1: The standard practice for VARTM models at present, the preform is assumed to be fully saturated and the thickness is calculated using Eqn (3.15)
- Model 2: this uses the same compaction behavior as Model 1 but superimposes Eqn (3.24) to account for the effect of saturation variation

- Model 3: This model includes the effect of hysteresis from Eqn (3.22)
- Model 4: This includes both the hysteresis effect and the saturation effect
- Model 5: This model is a limiting case in which the effect of changes in saturation on preform thickness are assumed to take place very slowly

Model 1:

$$\begin{aligned}
 h &= h_{\max} \left[c_1 + 1 - \{(1-p)(c_1^n - c_2^n) + c_2^n\}^{1/n} \right]^{-1} \\
 c_1 &= \alpha_a - 1 \\
 c_2 &= \alpha_a - \alpha_0
 \end{aligned} \tag{5.49}$$

from which

$$\frac{\partial h}{\partial p} = \frac{h_{\max} (c_1^n - c_2^n) \{(1-p)(c_1^n - c_2^n) + c_2^n\}^{1/n-1}}{n \left[c_1 + 1 - \{(1-p)(c_1^n - c_2^n) + c_2^n\}^{1/n} \right]^2} \tag{5.50}$$

and

$$\frac{\partial h}{\partial V_{sat}} = 0 \tag{5.51}$$

Model 2:

$$\frac{\partial h}{\partial p} = V_{sat} \frac{\partial h_s}{\partial p} + (1 - V_{sat}) \frac{\partial h_d}{\partial p} \quad (5.52)$$

Where h_s and h_d are both calculated using Eqn (5.50) using the appropriate constants for the saturated and dry behavior, and $\frac{\partial h_s}{\partial p}$, $\frac{\partial h_d}{\partial p}$ are therefore calculated from Eqn (5.50) again using the appropriate constants for saturated and dry behavior. The rate of change of thickness with saturation is then

$$\frac{\partial h}{\partial V_{sat}} = h_s - h_d \quad (5.53)$$

Model 3:

The underlying model is

$$\alpha = \frac{\alpha_u + k\alpha_0}{1 + k}, \quad \frac{\partial \alpha}{\partial \beta} = \frac{\partial \alpha_u}{\partial \beta} \frac{\alpha - \alpha_0}{\alpha_u - \alpha_0} \quad (5.54)$$

converting this to thickness and pressure terms

$$\frac{\partial h}{\partial p} = \frac{h^2}{h_u^2} \frac{\partial h_u}{\partial p} \frac{\frac{1}{h} - \frac{1}{h_{\min}}}{\frac{1}{h_u} - \frac{1}{h_{\min}}}$$

$$h_u = h_{\max} \left[c_1 + 1 - \{(1 - p)(c_1^n - c_2^n) + c_2^n\}^{1/n} \right]^{-1} \quad (5.55)$$

$$\frac{\partial h_u}{\partial p} = \frac{h_u^2 (c_1^n - c_2^n) \{(1 - p)(c_1^n - c_2^n) + c_2^n\}^{1/n - 1}}{h_{\max} n}$$

Model 4:

Again using Eqn (5.54) as the basic model since during infusion pressure monotonically increases,

but now modifying the expressions for α based on Eqn (3.24) give

$$\alpha_u = \frac{V_{sat} h_{\max s} + (1 - V_{sat}) h_{\max d}}{V_{sat} \frac{h_{\max s}}{a_{us}} + (1 - V_{sat}) \frac{h_{\max d}}{a_{ud}}}$$

$$\frac{\partial h_u}{\partial p} = \left(V_{sat} \frac{\partial h_{us}}{\partial p} + (1 - V_{sat}) \frac{\partial h_{ud}}{\partial p} \right) \quad (5.56)$$

$$\left. \begin{aligned} h_{ui} &= h_{\max i} \left[c_{1ui} + 1 - \left\{ (1 - p)(c_{1ui}^{n_{ui}} - c_{2ui}^{n_{ui}}) + c_{2ui}^{n_{ui}} \right\}^{1/n_{ui}} \right]^{-1} \\ \frac{\partial h_{ui}}{\partial p} &= \frac{h_{ui}^2}{h_{\max i}} \frac{(c_{1ui}^{n_{ui}} - c_{2ui}^{n_{ui}}) \left\{ (1 - p)(c_{1ui}^{n_{ui}} - c_{2ui}^{n_{ui}}) + c_{2ui}^{n_{ui}} \right\}^{1/n_{ui} - 1}}{n} \end{aligned} \right\} i = s, d$$

and as before (Eqn (5.55))

$$\frac{\partial h}{\partial p} = \frac{h^2}{h_u^2} \frac{\partial h_u}{\partial p} \frac{1}{h_u} - \frac{1}{h_{\min}} \frac{1}{h_u} - \frac{1}{h_{\min}} \quad (5.57)$$

The simplest option for the saturation modification assumes that alpha does not change as a result of a saturation change.

$$h = \frac{V_{sat} h_{\max s} + (1 - V_{sat}) h_{\max d}}{\alpha}$$

$$\frac{\partial h}{\partial V_{sat}} = \frac{h_{\max s} - h_{\max d}}{\alpha} = h \frac{h_{\max s} - h_{\max d}}{V_{sat} h_{\max s} + (1 - V_{sat}) h_{\max d}} \quad (5.58)$$

Model 5:

The same underlying behavior is used as in Model 4 however the preform is initially dry and

$$\frac{\partial h}{\partial V_{sat}} = 0 \quad (5.59)$$

Although physically unrealistic this model is included as a limiting case compared to Eqn (5.58).

5.8.4 Non-Linearity

The system of equations developed from Eqn (5.42) can be expressed in the standard form used by

Patankar as

$$\begin{aligned} a_P p_P - a_E p_E - a_W p_W &= a_P^0 p_P^0 + b \\ a_E &= \frac{\Gamma_e}{\delta x_e} \\ a_W &= \frac{\Gamma_w}{\delta x_w} \\ a_P^0 &= \frac{\Delta x_P}{\Delta t} \frac{\partial h}{\partial p} \\ b &= a_P^0 p_P^0 + S_C \\ a_P &= a_W + a_E + a_P^0 - S_P \end{aligned} \quad (5.60)$$

provided the coefficients a_P, a_E, a_W are positive, this set of equations can be solved iteratively, to converge to the exact solution of the nonlinear governing equation. The solution procedure is to calculate values of each coefficient for an initial guessed pressure field, and then solve to find an

updated pressure field. The solution is considered converged when the summed absolute difference between iterations is less than a preset tolerance (in this model I used 10^{-10}).

$$\epsilon^2 \geq \frac{\sum_{i=1}^N (p_i^{new} - p_i^{guess})}{N^2} \quad \epsilon^2 \geq \frac{\sum_{i=1}^N (P_i - P_i^*)^2}{N^2} \quad (5.61)$$

In updating the pressure equation the time step is also updated (i.e. the time step is calculated implicitly) however to ensure convergence the updated time step is subjected to a relaxation factor of α_{rel} .

$$\Delta t^{new} = \Delta t^{guess} + \alpha_{rel} (\Delta t^{calc} - \Delta t^{guess}) \quad (5.62)$$

The relaxation factor is necessary since otherwise the solution can oscillate significantly before converging in a controlled way.

5.8.5 Time Step Calculation

In this one dimensional system we use an implicit time step based on the flow front velocity. In each time step we want the flow front to move across a single element. This allows a consistent boundary condition at the element edge. We calculate the flow front velocity from the pressure gradient of the last filled element in the previous time step. In the linear equations we impose the boundary condition $p(x_{front}) = p_{out} = 0$ at the control volume boundary of the last control volume containing resin. This point is not part of the regular mesh but its position can be calculated as $x_{front} = x_p + \Delta x_p / 2$. At each new time step we add a new control volume to the flow domain.

Assuming the new control volume has a node point as x_P , the pressure gradient at the control volume inflow boundary (at position x_e) will be

$$\left(\frac{\partial P}{\partial x}\right)_{front}^0 = -\frac{2P_E^0}{\Delta x_E} \quad (5.63)$$

At the end of the time step the gradient at x_e will be

$$\left(\frac{\partial p}{\partial x}\right)_{front} = -\frac{P_E - P_P}{\delta x_e} \quad (5.64)$$

The total resin flow into the control volume in the time step will therefore be

$$\frac{h_e K_e}{2\mu} \left(\frac{P_E - P_P}{\delta x_e} + \frac{2P_E^0}{\Delta x_E} \right) \Delta t \quad (5.65)$$

This resin must fill the interstitial space of the volume, and allow for the change in tow saturation.

$$\frac{h_e K_e}{2\mu} \left(\frac{P_E - P_P}{\delta x_e} + \frac{2P_E^0}{\Delta x_E} \right) \Delta t = \Delta x_P \left(h_P - \frac{h_0}{V_{flow}} + V_{sat} h_0 \left(\frac{1 - V_{flow}}{V_{flow}} \right) \right) \quad (5.66)$$

The time step is therefore

$$\Delta t = \Delta x_P \frac{2\mu}{h_e K_e} \left(h_P - \frac{h_0}{V_{flow}} + V_{sat} h_0 \left(\frac{1 - V_{flow}}{V_{flow}} \right) \right) \left(\frac{P_E - P_P}{\delta x_e} + \frac{2P_E^0}{\Delta x_E} \right)^{-1} \quad (5.67)$$

5.9 Model Output

5.9.1 Convergence

The model convergence was tested by considering the time for the resin to flow from 210mm to 400mm for various element sizes (the lower limit is required because in the standard form of the

model the first 10 elements are already filled to provide an initial condition). Figure 5-7 shows the results of the convergence test for the hysteresis and saturation model (Model 4).

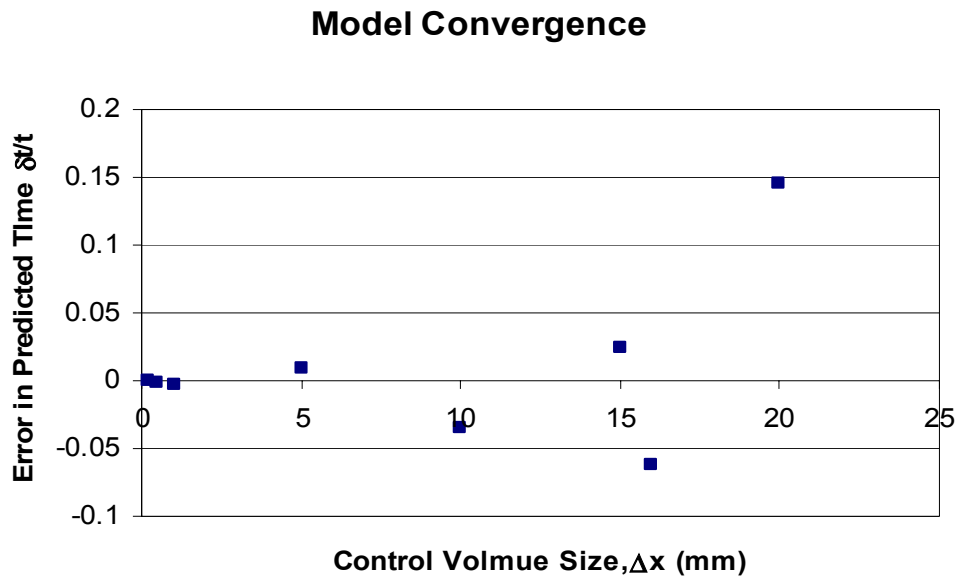


Figure 5-7 Convergence Plot Showing Error in Flow Time against Element Size

5.9.2 Model Results

The underlying behavior of the models was investigated using 1mm elements and a flow length of 380mm, and assuming a resin viscosity of 1Pas. The pressure profiles produced for all the models are qualitatively similar and therefore only a limited selection of the outputs is presented here. Figures 5-8 and 5-9 show typical pressure profiles at $L=100, 200, 300$ and 400 mm, for the combined hysteresis and saturation model. From these we can see that as flow proceeds the pressure gradient at the inlet end become very small. This effect is observed in actual components being molded, where the inlet end of the infusion becomes ‘baggy’ and the inlet flow rate becomes very small, even though the flow front is still moving.

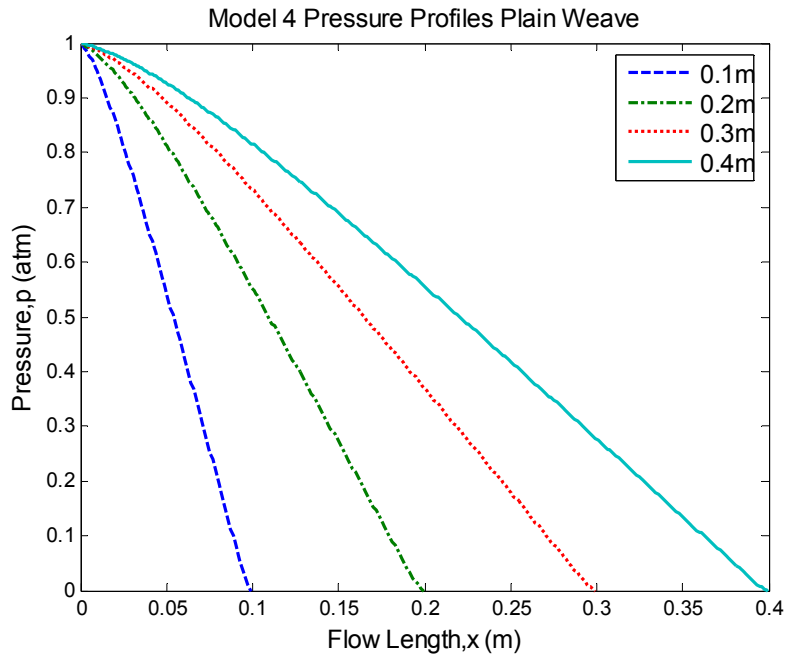


Figure 5-8 Pressure Profiles for Resin Flow in Plain Weave Fabric

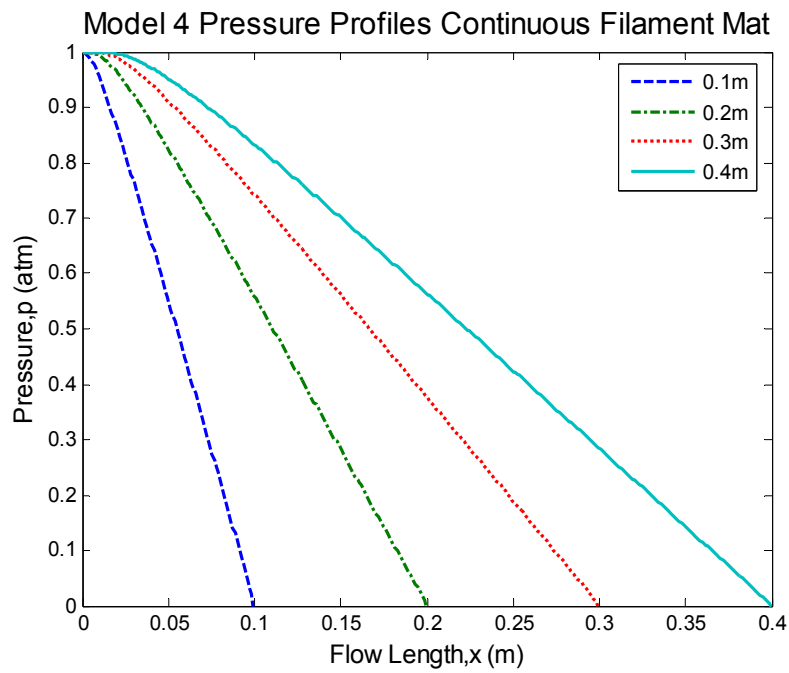


Figure 5-9 Pressure Profiles for Flow in Continuous Filament Mat

Figure 5-10 shows for the plain weave model how the thickness varies near the flow front as an effect of the change in elastic properties due to the variation in saturation. (In this figure the combined hysteresis and saturation model was used.) Here we can see that a more gradual thickness profile is observed, rather than an abrupt change in thickness at the flow front, and as the flow proceeds this gradually settles to a consistently shaped reduction in thickness over the unsaturated flow region. From Figure 5-10 we can also see that the unsaturated flow region has a stable length (of approximately 10mm.)

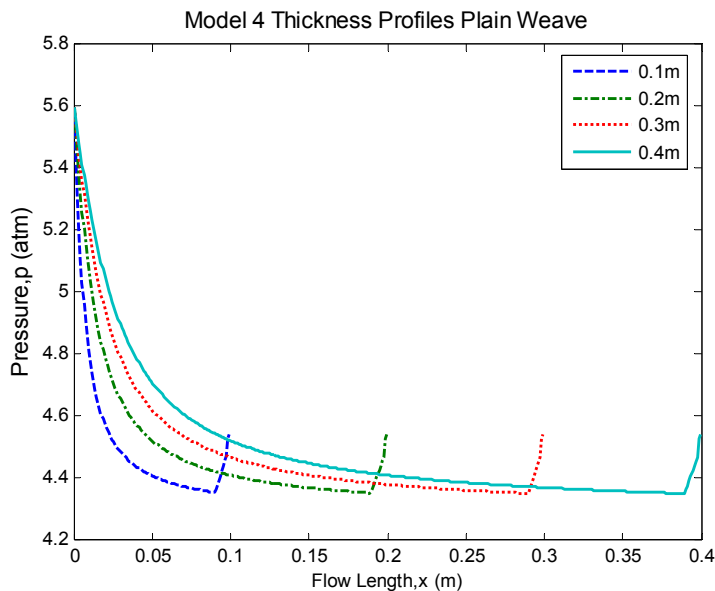


Figure 5-10 Thickness Profiles Showing Saturation Effect in Plain Weave

For the CFM the difference in thickness profiles for the various models is not significant, except for the model where the effect of saturation is ignored. This is because the CFM is assumed to wet immediately, and the hysteresis models therefore immediately conform to the unloading curve. The changes in flow rate observed in Figure 5-11 are due mainly to the difference in assumption of the

thickness and permeability of the flow front element. For the models which include saturation effects the flow front element changes thickness during the flow period. For the other models it is assumed to start at the saturated thickness.

The differences in flow rate are smaller for the plain weave due to the smaller range in variation of the thickness under the different pressure profiles.

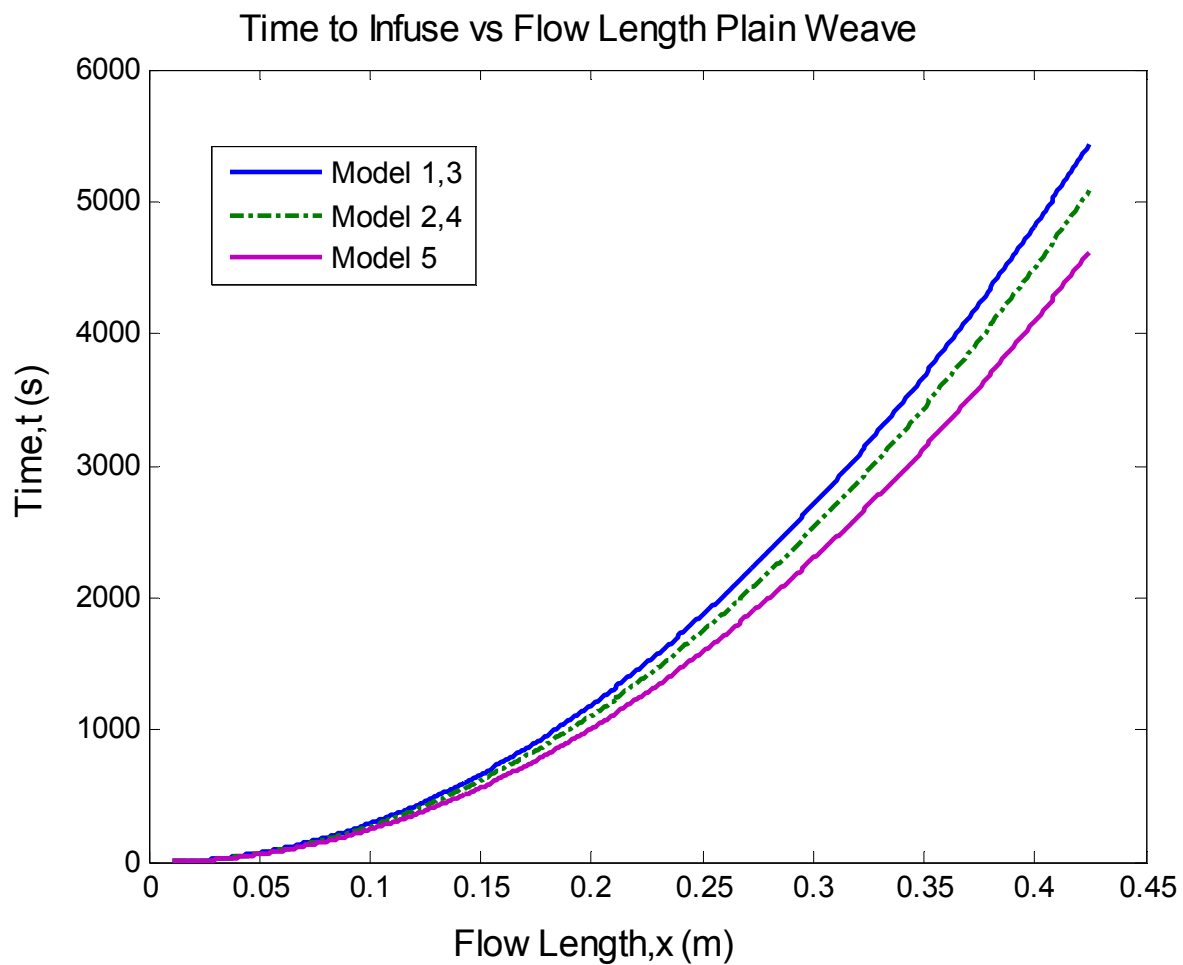


Figure 5-11 Model Flow Front Position Results For Plain Weave

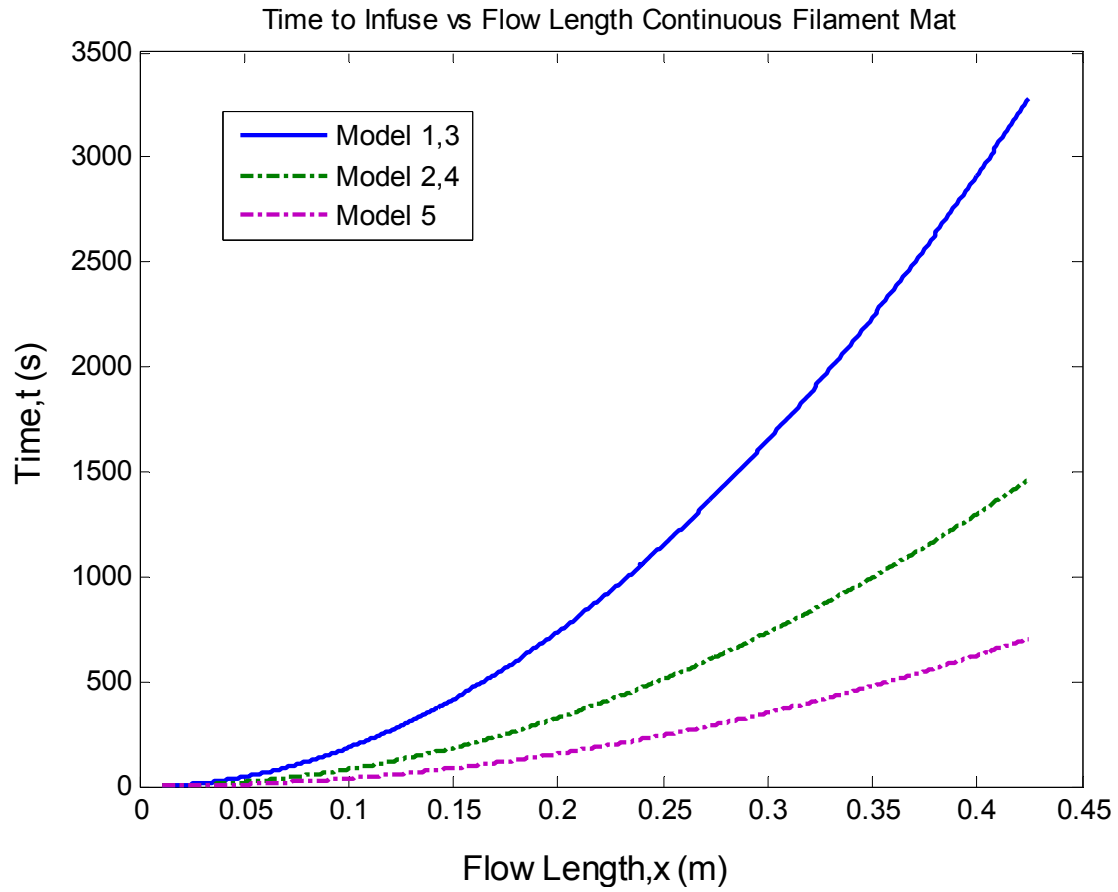


Figure 5-12 Model Flow Front Positions for Continuous Filament Mat

6 Experimental Methods

6.1 Shadow Moiré

6.1.1 Basic Moiré Theory

The moiré effect occurs when two sets of closely spaced patterns are overlaid, resulting in changes in contrast depending on the degree of overlap between the patterns. In most cases this results in fringes indicative of gradients in local displacements between a reference pattern or grating which remains undistorted and a specimen pattern or grating, which is allowed to distort under the action of some physical process. The term moiré was originally applied to semitransparent fabrics, where two layers of fabric produce a ripple pattern due to the differences in the distortion of the fabric while it is worn.

In shadow moiré, one of the earliest scientific applications of the moiré effect (Sciammarella in a comprehensive review [47] in 1982 cites a paper from as early as 1925 [48]), the specimen grating is typically created by projecting light through the reference grating and observing the moiré effect between the shadows formed on the surface of the specimen and the reference grating. The geometrical arrangement is such that displacements in the specimen surface

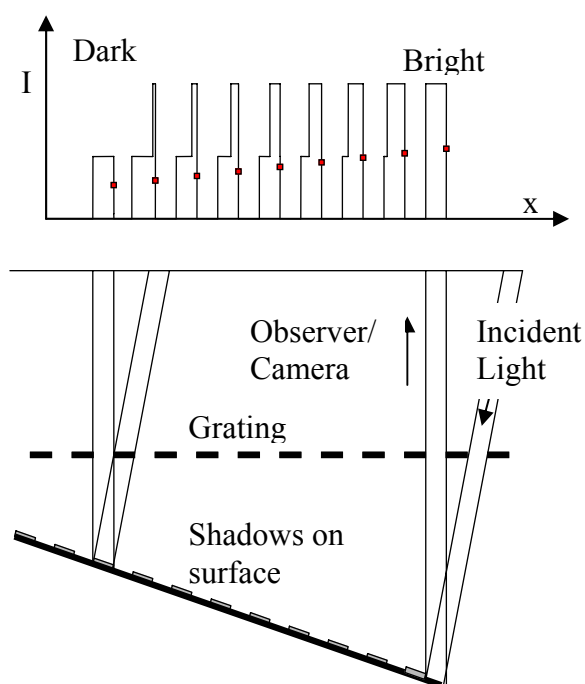


Figure 6-1 Basic Shadow Moiré Geometry

perpendicular to the reference grating result in displacements of the projected shadow parallel to it and hence the formation of moiré patterns. Figure 6-1 shows the basic arrangement for parallel incident light. Some of the key features can be seen in this diagram. In particular, we can see that the moiré pattern requires some averaging of the local observed light intensity. The lines in the inset chart represent the local intensity (I) and the square points represent the intensity averaged over one grating pitch (\bar{I}) plotted against their observed position x . A bright fringe is observed where the shadows line up precisely with the grating lines, and a dark fringe is observed where the shadows line up precisely with the gaps between the grating lines.

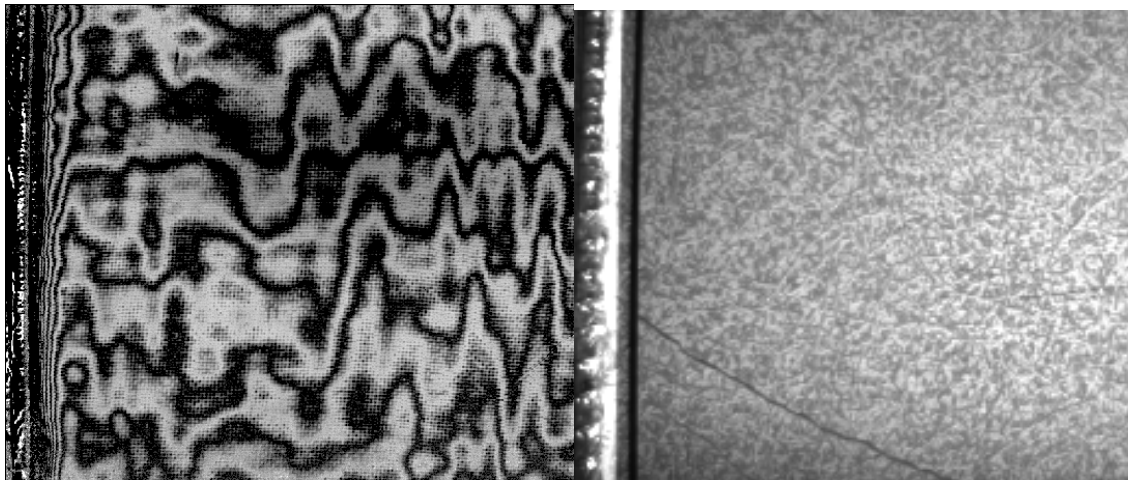


Figure 6-2 Moiré Images of 16 ply Plain Weave (left) and 4 Ply CFM (right) using 100 lines/inch Grating

Figure 6-2 shows typical moiré images of the plain weave and of the CFM fabric. A simpler example showing moiré fringes created by a steel stepped wedge can be seen in Figure 6-3. Here a steel plate has been machined into a set of angled steps. The top step is lined up parallel to the moiré grating, and the remaining 3 steps are at 0.27, 0.5 and 1 degrees to the plane of the grating.

From this we can see that the distance between fringes on the second step is half the distance between fringes on the first step, and on the third step the distance is approximately one third of the distance between fringes on the first step. In effect the fringes act as depth contours of the surface below the plane of the grating. It is worth noting that the orientation of the wedge compared to the light source or grating direction has no effect on the fringe spacing.

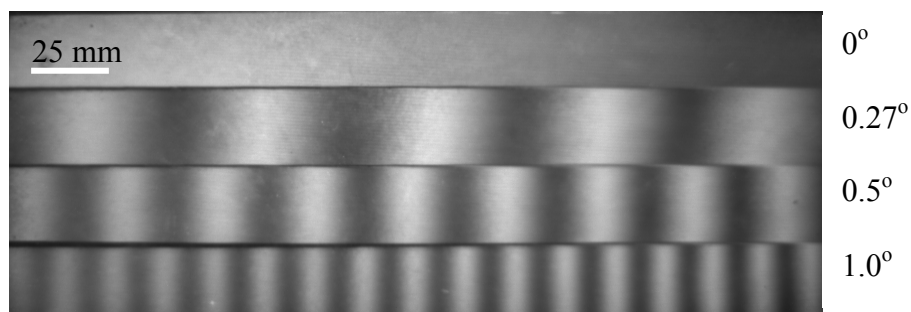


Figure 6-3 Shadow Moiré Image of Calibration wedge

In shadow moiré we need to ensure that the fringes act as equal depth contours. This can be achieved by using parallel illumination and observing from a long distance, however this requires intense illumination and a large area to work in. To create high intensity fringes it is more convenient not to use parallel light, and to site the observer (typically a digital camera) close to the grating. In the 1970s Takasaki [49] and Meadows [50] published general descriptions of the geometric arrangements for shadow moiré and demonstrated methods to develop moiré fringes as contours of equal distance from a reference plane. This geometry, which was used in the shadow moiré system built as a part of this work, is discussed in more detail in section 6.1.2. Sciammarella's Fourier series interpretation of moiré fringes [51] along with digital photography

allowed for more accurate interpolation between the fringe peaks and troughs, and the development of phase shift methods [52, 53] significantly increased the accuracy with which measurements could be made (up to 1/70 of a fringe) for static conditions.

In 1998 Harding and Bieman [54] reviewed several methods available for high speed shadow moiré, including fringe counting for single images, moving part phase shift methods, color encoded phase shift methods, multi camera phase shift methods, and split image phase shift methods. The last three methods require the entire system to be mounted on an optical bench (or similar) for acceptable results, which is cumbersome for monitoring the VARTM process. The moving part method requires additional image correction due to the changes which may take place between capture of individual images, and the fringe counting is limited in its accuracy. In the late 1990s temporal phase unwrapping methods were also being developed, in particular for electronic speckle pattern interferometry (ESPI) [55-57]. However, these methods suffer some limitations in cases where the direction of the movement is not monotonic or periodic.

6.1.2 Takasaki/Meadows Geometry for Shadow Moiré

The compact geometry for shadow moiré shown in Figure 6-4 was described by both Takasaki [49] and Meadows [50]. The Figure shows a general shadow moiré arrangement where a line grating forms the reference plane, with the y axis aligned with the grating lines and the camera placed directly over the origin on the z axis.

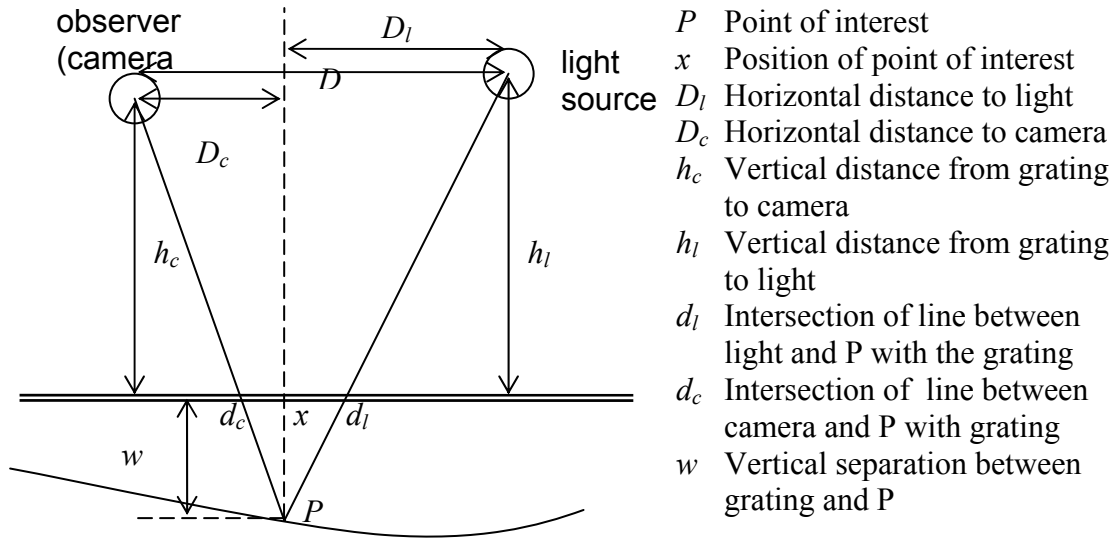


Figure 6-4 General Geometry for Shadow Moiré

The intensity of the light corresponding to a point P is a function of the transmittance of the grating at points d_l and d_c , the intensity of the light which would be recorded in the absence of the grating a , and the intensity of any background light b which the camera may also record

$$I(x, y) = a(x, y)T(d_c)T(d_l) + b(x, y) \quad (6.1)$$

In moiré patterns, the fringe intensity as differentiated from the local intensity at a point $P(x, y)$ is the average intensity over a single grating pitch p . This averaging is either an intrinsic part of the optical system, for example when the camera cannot resolve individual lines in the grating, or can be carried out numerically if the camera is able to resolve the individual lines.

$$\bar{I} = \frac{1}{p^2} \int_{x_p - p/2}^{x_p + p/2} \int_{y_p - p/2}^{y_p + p/2} I dy dx = \frac{1}{p} \int_{x_p - p/2}^{x_p + p/2} \int_{y_p - \lambda/2}^{y_p + \lambda/2} aT(d_c)T(d_l) dy dx + \frac{1}{p^2} \int_{x_p - \lambda/2}^{x_p + \lambda/2} \int_{y_p - \lambda/2}^{y_p + \lambda/2} b dy dx \quad (6.2)$$

Assuming that the variation in a is small over a single pitch distance and expressing I (a periodic function with period π) as a Fourier series, and carrying out appropriate algebraic manipulation this can be rewritten as

$$I = A(x, y)F(d_l - d_c) + B(x, y) \quad (6.3)$$

where F is a symmetrical periodic function with period p and amplitude 1, A is the fringe amplitude and B is the median intensity at the point. The precise form of F can be determined experimentally, and through the use of an appropriate optical system (e.g. sinusoidal grating, suitable separation of grating and object surface, filtration of higher harmonics) can generally be treated as a cosine. However, the analysis described below does not rely on any particular form of F , as long as the actual shape is known, and an inverse can be calculated over the range of half a period. The values of d_l and d_c can be obtained through the geometry shown in Figure 6-4. Thus

$$I_f = A(x, y)F\left(\frac{wD_l}{w+h_l} - \frac{wD_c}{w+h_c}\right) + B(x, y) \quad (6.4)$$

where w is the normal distance from the grating to the specimen, D_l and D_c are distances parallel to the grating from the reference point on the specimen to the illumination source and the camera respectively, and h_l and h_c are the normal distances. As noted by Takasaki [49] if $h_c = h_l$ and $w \ll h_c$ the above equation becomes

$$I_f = A(x, y)F\left(w\frac{D_l - D_c}{h_c}\right) + B(x, y) \quad (6.5)$$

and if we introduce an effective pitch $p_e = p h_c / D_c$ we can rewrite it as

$$I_f = A(x, y) f(w) + B(x, y) \quad (6.6)$$

where f is a symmetric periodic function of period p_e typically

$$f(w) = \cos\left(\frac{2\pi w}{p_e}\right) = \cos\left(\frac{2\pi(w + p_e)}{p_e}\right) = \cos\left(\frac{-2\pi w}{p_e}\right) \quad -1 \leq f(w) \leq 1 \quad (6.7)$$

The effective pitch p_e can be calculated from the geometry of the system, however, it is usually easier to use the system response to a calibration wedge, or relative movements between the grating and surface to calculate p_e , as described by Joris [58]. Carrying out this type of calibration also allows the functional form of f to be verified, or found (since as noted above the analysis does not depend on f being sinusoidal), and to ensure that there is no significant dependence of the effective pitch on the distance between the grating and the specimen surface, which would indicate an error in the geometrical arrangement of the system.

6.1.3 Phase Wrapped Images and Image Unwrapping

The first step in recovery of the displacements w from a data set is to eliminate A and B . In phase stepped methods this is done with multiple images, in effect generating three or more equations for the three unknowns w , A and B . Alternatively using Joris' calibration method, A and B can be calculated for each point in the image, and from this $f(w)$ can be calculated. The multi-phase or phase stepped moiré is a very convenient method for calculation of height profiles of static surfaces. Assuming the moiré fringes have a sinusoidal variation, by altering the moiré fringe

phase by known amounts (typically by moving either the grating or the object) it is possible to calculate w within a single fringe order. This is sometimes described as a phase wrapped value and its relationship to w is

$$\begin{aligned}\psi(w) &= w & 0 \leq w \leq p_e \\ \psi(w) &= \psi(w + p_e) & 0 \leq \psi \leq p_e\end{aligned}\quad (6.8)$$

where $\psi(w)$ is the phase wrapped value of thickness. To calculate this from a sinusoidal function such as Eqn (6.7) we can collect fringe data at a reference position (I_{ref}) and at two additional positions with the grating displaced δ above (I_+) and below (I_-) the reference position. Using standard trigonometric identities we can show

$$\frac{I_+ - I_-}{2I_{ref} - I_+ - I_-} = \frac{1 - \cos \frac{2\pi\delta}{p_e}}{\sin \frac{2\pi\delta}{p_e}} \tan \frac{2\pi z}{p_e} \quad (6.9)$$

The arctangent can be calculated in such a way as to preserve the full phase information and calculate the phase wrapped values. As an example, the use of this method to determine the shape of the steel step wedge as shown in Figure 6-3 is described. The steel plate was machined to create 4 angled planes; in the image in Figure 6-3 one of the planes has been aligned parallel to the grating (labeled 0° in the image). By measuring the distance between successive peaks or troughs, we can verify the calibration of the system, and ensure that the micrometer positioning system is working correctly.

To analyze the image, the longer wavelength variations are eliminated by first taking a discrete

Fourier transform of the intensity values along the length of the wedge, removing the first harmonic of the Fourier series and then inverting the Fourier transform. The recovered image then has the longer wavelength variations eliminated, and the result is shown in Figure 6-5.

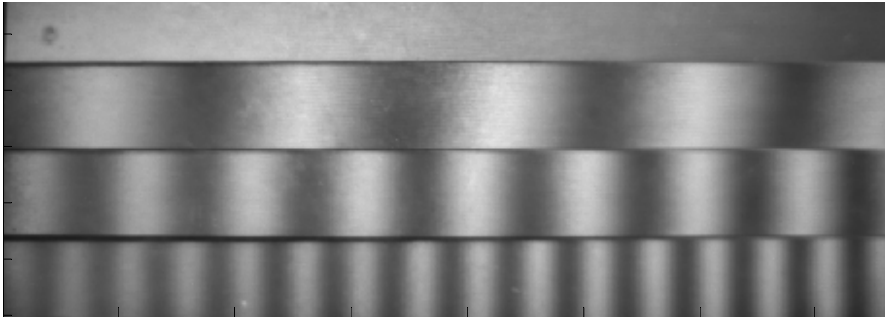


Figure 6-5 Filtered Image of Wedge with Low Frequency Variation Removed

Figure 6-6 shows the intensity along lines taken at the center of each step, and these can be used to calculate the average spacing of the fringes.

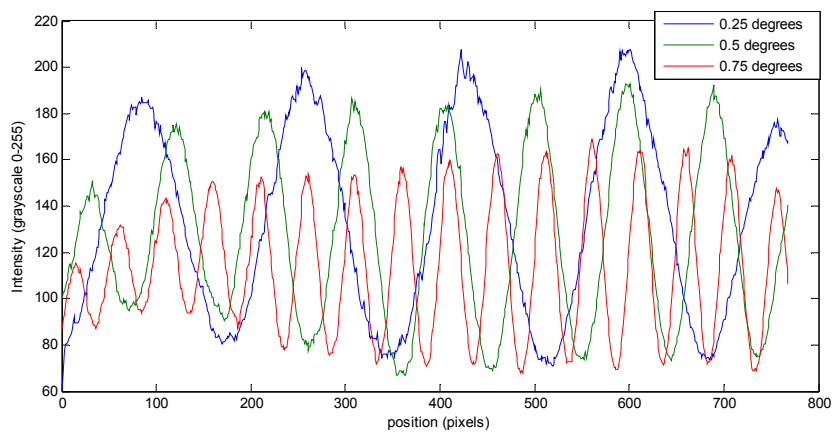


Figure 6-6 Intensity Plots Along Wedge Steps

These positions are then converted from a position in pixels to a position in mm on the plane of the image, and the average fringe spacing calculated, giving an effective pitch of 3.60 mm^{-1} .

Using the micro-positioner the system can be calibrated using the Joris method, and a calibration factor calculated for the micro-positioner step length. The micro-positioner can then be used to take a set of 3 images for multi phase analysis. Using Eqn (6.9) these images can then be converted to a phase wrapped image. Figure 6-7 shows a phase wrapped height map of the step wedge.

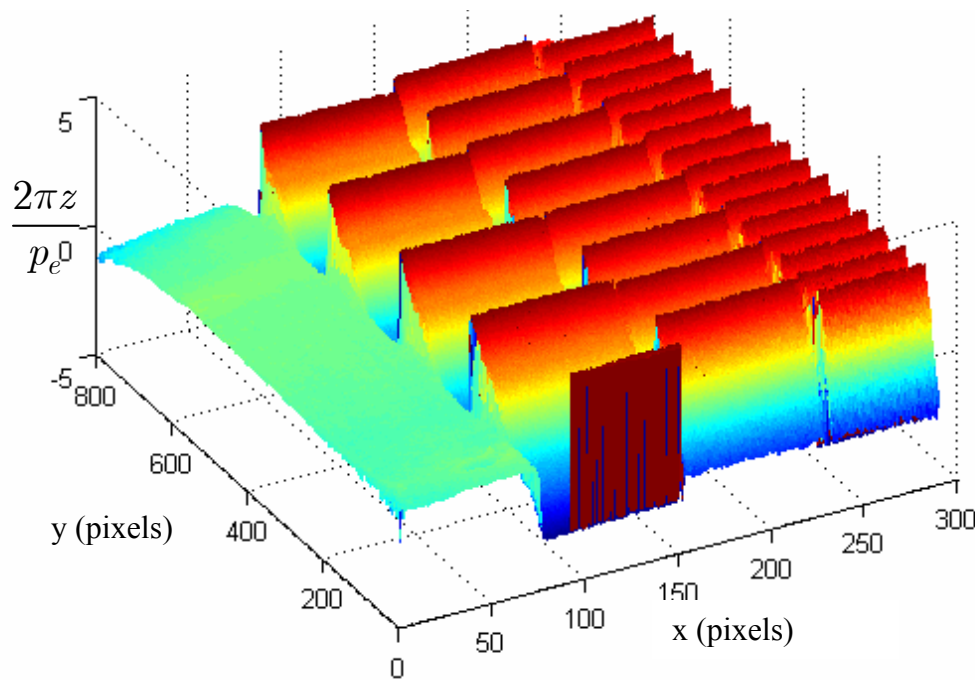


Figure 6-7 Phase Wrapped Height Map of Step Wedge

Here the distinct steps at the start of each new phase can clearly be seen. In addition it is clear that the gradient of each step is preserved in the phase wrapped data set. However, to recover the actual values of the surface heights this wrapped image must be unwrapped. A simple “line following” algorithm will work well to unwrap this. The line following algorithm follows a path in the image and whenever a step of 2π (plus or minus a small tolerance) is encountered between adjacent data

points, 2π is added to all the data points encountered previously along the line. In this way all the jumps are eliminated. Figure 6-8 shows three unwrapped lines from the step wedge.

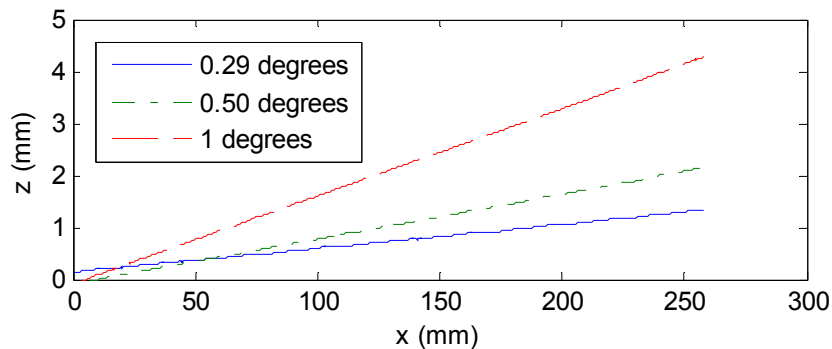


Figure 6-8 Unwrapped Lines from the Phase Wrapped Step Wedge Dataset

For more complex shapes such as VARTM preforms, line stepping algorithms have some difficulties, especially where any noise is present in the dataset. The lines in Figure 6-8 indicate one typical problem, since the line following algorithm cannot handle the stepped areas of the wedge without manual modifications it cannot easily match the thicknesses perpendicular to the wedge slopes. A more robust method was developed by Ghiglia and Romero [59], which uses a least squares minimization to eliminate the steps found, and is much better able to handle complex shapes. The operation uses the properties of a cosine transformation to carry out the unwrapping operation very efficiently, and a complete description can be found in their paper. This method produces very good results where a multi phase image is available. Figure 6-9 shows one of the three intensity images and the phase wrapped image generated from it and two other images for a small section of the CFM material.

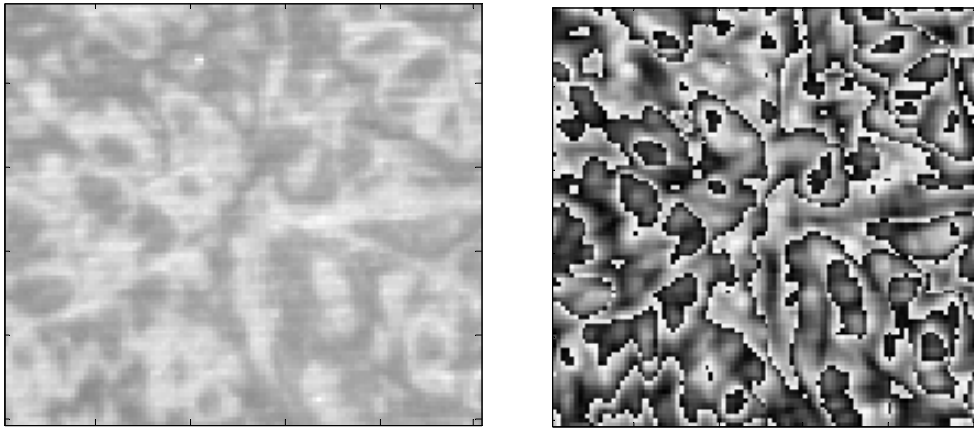


Figure 6-9 Intensity Image and Phase Wrapped Image of Segment of CFM Material

Using the Ghiglia algorithm we can use the phase wrapped image here to generate a surface profile and the results can be seen in Figure 6-10.

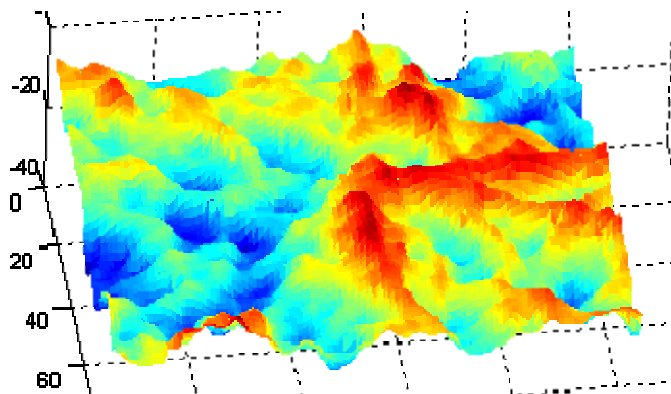


Figure 6-10 Surface Profile of Continuous Filament Mat Generated using Ghiglia Algorithm [59]

This type of unwrapping (either line following, or using the Ghiglia method) cannot work with single images since the phase wrapping in a single image is symmetrical, and the distinct steps found in the asymmetrically wrapped function do not exist.

6.1.4 Single Image Unwrapping

A significant difficulty with using shadow moiré to study evolving processes is the inability to collect a set of phase stepped images at each point in the process. Typically making a phase adjustment takes a finite length of time, and relies on very consistent repeated movements of the apparatus. It is not possible to calculate an asymmetric phase wrapped value from a single image since f is symmetric and periodic. We can only calculate a symmetric periodic inverse $\hat{\psi}$

$$\begin{aligned}\hat{\psi}(w) &= f^{-1}(f(w)) \\ \hat{\psi}(w) &= w & 0 \leq w \leq \frac{p_e}{2} \\ \hat{\psi}(w + p_e) &= \hat{\psi}(w) = \hat{\psi}(-w) & 0 \leq \hat{\psi} \leq \frac{p_e}{2}\end{aligned}\quad (6.10)$$

Figure 6-11 shows the functions f , ψ and $\hat{\psi}$ graphically (here using a cosine form of f)

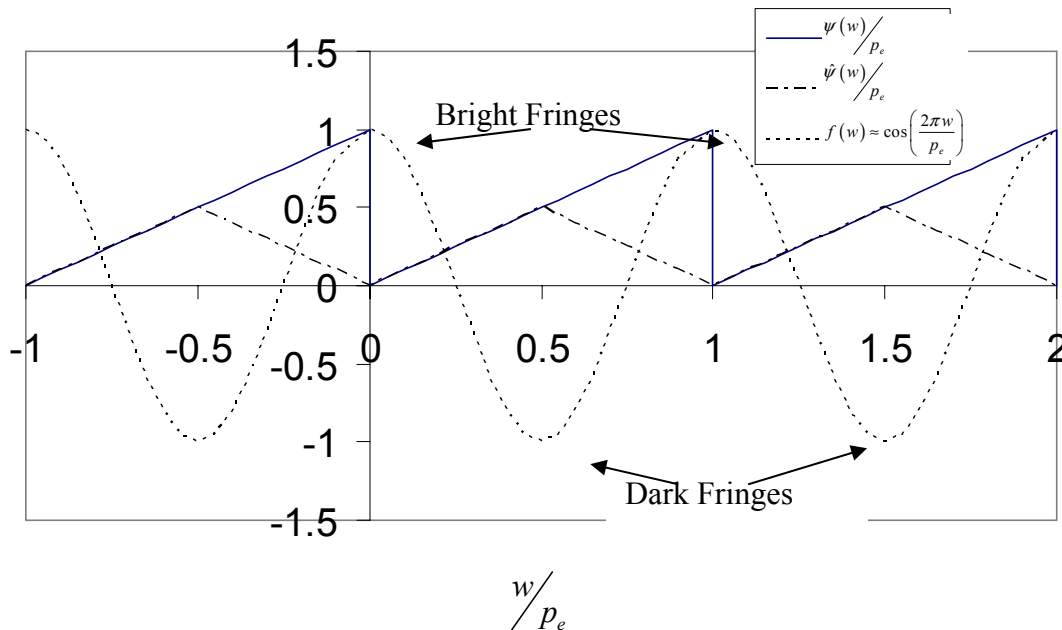


Figure 6-11 Functions of Surface Height w Used in Shadow Moiré Analysis

As can be seen from Figure 6-11, the asymmetric function ψ is significantly easier to unwrap than the symmetric function $\hat{\psi}$. This is due in part to the discontinuity at the end of each periodic repetition, and also to the fact that $\frac{\partial\psi}{\partial t} = \frac{\partial w}{\partial t}$ everywhere except at the discontinuity. There is a significant body of literature [47-65] discussing the unwrapping of functions of the form of ψ . In this section we therefore propose a method to convert the calculated values of $\hat{\psi}$ into values of the form of ψ , to allow these unwrapping algorithms to be applied. In many cases it is sufficient to take sufficient samples as t varies, and combine these with the known variation in the surface shape, however this requires some prior knowledge of the expected variation, and works best when the variation is monotonic.

The main challenges in interpreting moiré images are firstly the extraction of function f from the intensity data, and secondly the inversion of f to calculate w . In multi phase methods f is calculated by elimination of A and B from Eqn (6.6) and therefore requires at least 3 images, though for noisy systems additional images can improve the accuracy of the calculations. In temporal unwrapping the values of A and B are extracted from the Fourier analysis of time variation of the intensity, or can be calculated from the calibration run, which is in effect a multi phase image calculation. In the experimental work discussed here the calibration values are used to extract f , since the total variation of displacement is insufficient for Fourier analysis of the intensity variation.

The initial instrument calibration is used to collect an accurate starting surface profile. This yields values of $\psi(z_i^0)$ where z_j are the values of w at series of points indexed with i , and the superscript

0 indicates the initial values, as well as the calibration values A_j and B_i (the image amplitude and background intensity at the corresponding points). An additional calibration set is taken at the end of the experimental run allowing for calculations to be based on the final phase wrapped surface profile $\psi(z_i^\infty)$ as well as the initial surface profile.

Each subsequent image contains intensity data from which $\hat{\psi}(z_i) = \hat{\psi}(z_i^0 + \delta z)$ (here δz is the change in surface profile from the initial condition) can be calculated using the calibration values noted above. Because $\hat{\psi}$ is symmetric, we cannot directly recover δz , however, we can calculate the four possible values of $\psi(\delta z)$

$$\begin{aligned}
 \psi(\delta z) &= \psi(\hat{\psi}(z_i) - \hat{\psi}(z_i^0)) & \psi(z_i^0) \leq P_e/2; \psi(z_i) \leq P_e/2 \\
 &= \psi(-\hat{\psi}(z_i) - \hat{\psi}(z_i^0)) & \psi(z_i^0) \leq P_e/2; \psi(z_i) > P_e/2 \\
 &= \psi(-\hat{\psi}(z_i) + \hat{\psi}(z_i^0)) & \psi(z_i^0) > P_e/2; \psi(z_i) \leq P_e/2 \\
 &= \psi(\hat{\psi}(z_i) + \hat{\psi}(z_i^0)) & \psi(z_i^0) > P_e/2; \psi(z_i) > P_e/2
 \end{aligned} \tag{6.11}$$

From the initial calibration we can eliminate two of the possible values, as we know $\psi(z_i^0)$ with good confidence.

6.1.5 Statistical Separation of Phases

In this method we define a set of points with a corresponding set of heights $Z = \{z_1, z_2, \dots, z_N\}$

where the variation in δz_i from the initial set of heights $Z^0 = \{z_1^0, z_2^0, \dots, z_N^0\}$ is expected to be small

and any variations in δz_i randomly distributed. Experimentally we can calculate $\psi(z^0)$ and

$\hat{\psi}(z)$ for each point, and we can therefore also determine for any point if $\psi(z_i^0) \leq P_e/2$. Taking the four possible ways of calculating $\psi(\delta z_i)$ and only considering those that are valid for our known values of $\psi(z_i^0)$ we can tabulate the sets of possible results as shown in Table 7. The union of the four sets is

$$X = X_1 \cap X_2 \cap X_3 \cap X_4 = \{\psi(\delta z_i)\} \cap \{\psi(-2z_i^0 + \delta z_i)\} \quad (6.12)$$

Table 7 Possible Result Sets for Changes in Surface Height

	$\psi(z^0) \leq P_e/2$ $\psi(z) \leq P_e/2$	$\psi(z^0) \leq P_e/2$ $\psi(z) > P_e/2$	$\psi(z^0) > P_e/2$ $\psi(z) > P_e/2$	$\psi(z^0) > P_e/2$ $\psi(z) \leq P_e/2$
$X_1 = \{\psi(\hat{\psi}(z_i) - \hat{\psi}(z_i^0)) \psi(z_i^0) \leq P_e/2\}$	$\psi(\delta z_i)$	$\psi(-2z_i^0 - \delta z_i) \notin X_1$	$\notin X_1$	$\notin X_1$
$X_2 = \{\psi(\hat{\psi}(z_i) + \hat{\psi}(z_i^0)) \psi(z_i^0) > P_e/2\}$	$\notin X_2$	$\notin X_2$	$\psi(\delta z_i)$	$\psi(-2z_i^0 - \delta z_i)$
$X_3 = \{\psi(-\hat{\psi}(z_i) - \hat{\psi}(z_i^0)) \psi(z_i^0) \leq P_e/2\}$	$\psi(-2z_i^0 - \delta z_i)$	$\psi(\delta z_i)$	$\notin X_3$	$\notin X_3$
$X_4 = \{\psi(-\hat{\psi}(z_i) + \hat{\psi}(z_i^0)) \psi(z_i^0) > P_e/2\}$	$\notin X_4$	$\notin X_4$	$\psi(-2z_i^0 - \delta z_i)$	$\psi(\delta z_i)$

If the values of $\psi(z_i^0)$ are uniformly distributed between 0 and λ_e , the values of $\{\psi(-2z_i^0 + \delta z_i)\}$ will also be uniformly distributed between 0 and λ_e , and therefore a histogram of the distribution of the values of X will have the form

$$P(\chi) = \frac{1}{N} \left(\frac{1}{2} + \frac{1}{2\sigma\sqrt{2\pi}} e^{-\frac{(\chi-\mu)^2}{2\sigma^2}} \right) \quad (6.13)$$

In the case of VARTM the surface waviness of the preform ensures sufficient variation in the values of $\psi(z_i^0)$. In other cases the surface may need to be tilted. If the values of $\psi(z_i^0)$ are not uniformly distributed, we gain nothing from this procedure, however, in this case one of the other available unwrapping methods will work fairly effectively. Figure 6-12 shows a typical data set along with a calculated probability density function based on Eqn (6.13).

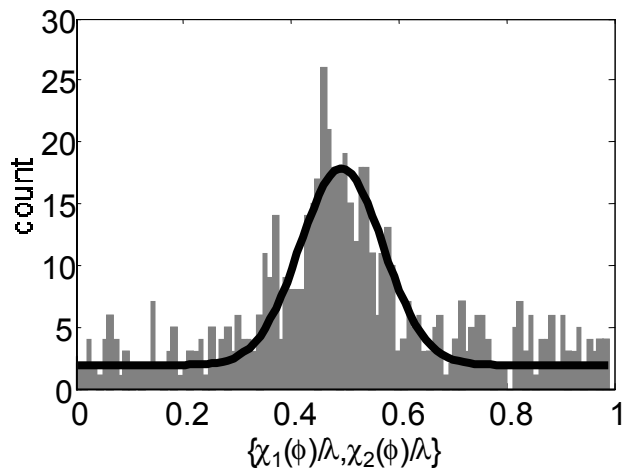


Figure 6-12 Histogram of Data Points from a Shadow Moiré Image of a Region of a VARTM Process (Probability density function shown as smooth black curve)

6.1.6 Experimental Validation

A diagram of the experimental system is shown in Figure 6-13. The surface to be measured rests on a stage with a simple adjustment mechanism to vary the orientation of the sample with respect to the grating. In the case of VARTM this is an aluminum plate, with appropriate ports drilled to allow the passage of resin. A grating is suspended on a frame over the specimen stage, the frame can be moved by a computer controlled micro-positioner. The micro-positioner has a resolution of

$\sim 0.1\mu\text{m}$, and, to reduce the loading, an elastic compensator is used to carry most of the mass of the frame and moiré grating.

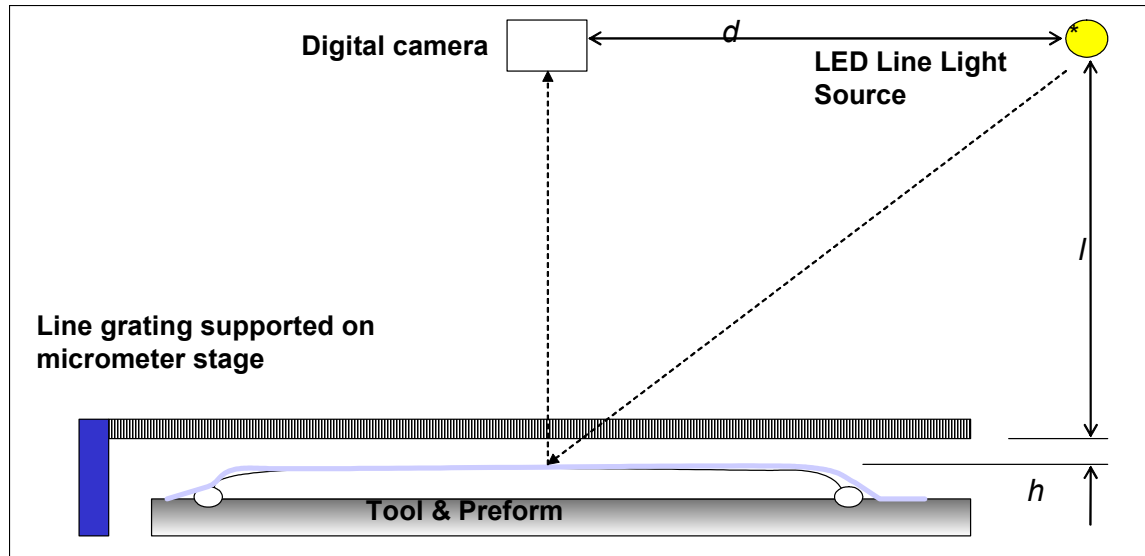


Figure 6-13 Shadow Moiré Setup for Recording Surface Morphology During VARTM Process

In these experiments a chrome-on-glass moiré grating was used with a pitch of 0.0847mm (100 lines/in.) The image field was illuminated by a light emitting diode line light source, and the images were captured with a Basler 622f monochrome DCAM camera at a resolution of 1024x768 pixels. The entire optical system is covered with dark cloth acting as a black-out screen. To provide consistent high contrast shadows the surface of the VARTM vacuum bag was painted with high opacity acrylic emulsion paint pigmented with titanium oxide. The image collection and positioning are controlled by computer.

The VARTM preform in the experiment consisted of 16 plies of 7500 plain weave glass fabric with no distribution medium. The preform was enclosed in a vacuum bag and the bag evacuated.

Once prepared, the vacuum bag was painted white, and the tool plate mounted on the Moiré stage and leveled. The camera settings were then adjusted to maximize the value of the fringe amplitude A across the region of interest. Typically A varies between 50/255 and 100/255 and B (the background intensity) varies between 70/255 and 150/255. The values of p_e are then calculated for the same region, by taking a series of up to 300 images while moving the micro-positioner a fixed amount between each image; the grating movement is set to be sufficient to ensure that the intensity at each point varies through approximately two wavelengths (i.e. step size $\sim 2p_e/300$). The optical system is adjusted, as required, to eliminate any variations in p_e (allowing for fine tuning of the geometry of the system). The large number of images taken helps to ensure that the mechanical system is working properly and verifies that the appropriate variation of $f(z)$ is found experimentally. (Over the normal range of the instrument $f(z)$ is typically sinusoidal, though for small values of z the shape can be closer to a simple ramp waveform.)

During the experimental trials, the camera captures three images in quick succession (less than 34 ms apart) at 10 second intervals and the computer averages the result. For the speed of VARTM flow this was found to give the best compromise for reducing random noise without significant movement of the preform surface between images.

At the end of the flow period the resin flow is shut off at the inlet and the vacuum maintained, the preform eventually settles to its final shape, and another 300 image calibration sequence is taken. This second calibration set can be used to calculate the total change in thickness from start to finish

using a multi phase calculation, and also allows for the small random changes in the thickness which occurs as a part of the fiber wetting process to be taken into account.

6.1.7 Trial Data

Test data were generated using MATLAB to check the effectiveness of the algorithm under various conditions. Table 8 shows the basis of the test data sets used in evaluating the algorithm.

Table 8 Data Used for Algorithm Evaluation Trials

Variable	Value
A	100 (Grayscale 0-255)
B	128 (Grayscale 0-255)
p_e	300 μ m
Calibration noise:	1 (Grayscale 0-255)
image size	1024x768
Pixels:Length	10:1mm

The initial surface z_0 is a set of random values between 1mm and $1+p_e$. δz is a spherical surface of radius 100m, centered at (51.2mm, 38.4mm, 100m+1mm). Moiré images are simulated by calculating an expected intensity based on equation (6.7). Noise is added to the image at varying levels to assess the ability of the algorithm to deal with noisy signals. The noise level added is expressed as a ratio of the standard deviation of the added Gaussian noise to the full scale of the measurement. In practice under the lighting conditions used, the signal varies by 1-2 gray levels on a full scale of 0-255, corresponding to a noise ratio of less than $2/255$ or 0.01. Figure 6-14 shows typical noisy moiré images of the surface as simulated in MATLAB.

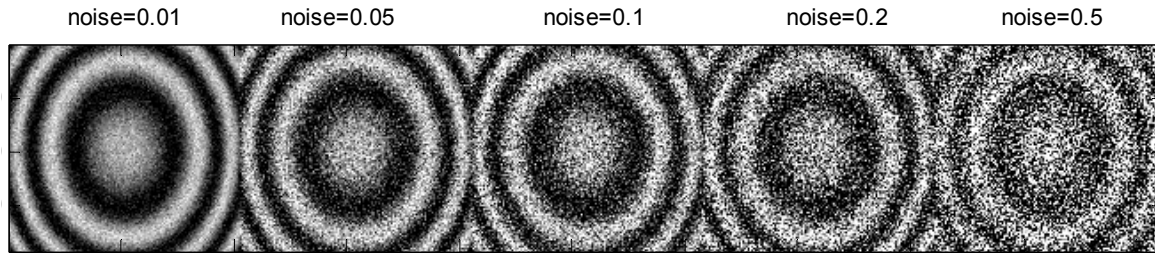


Figure 6-14 Images Showing Effect of Added Noise to Fringe Patterns Generated from a Simulated Spherical Surface.

Applying the statistical separation we can consider a line in the image and show the error in the calculated values of δz (Figure 6-15.)

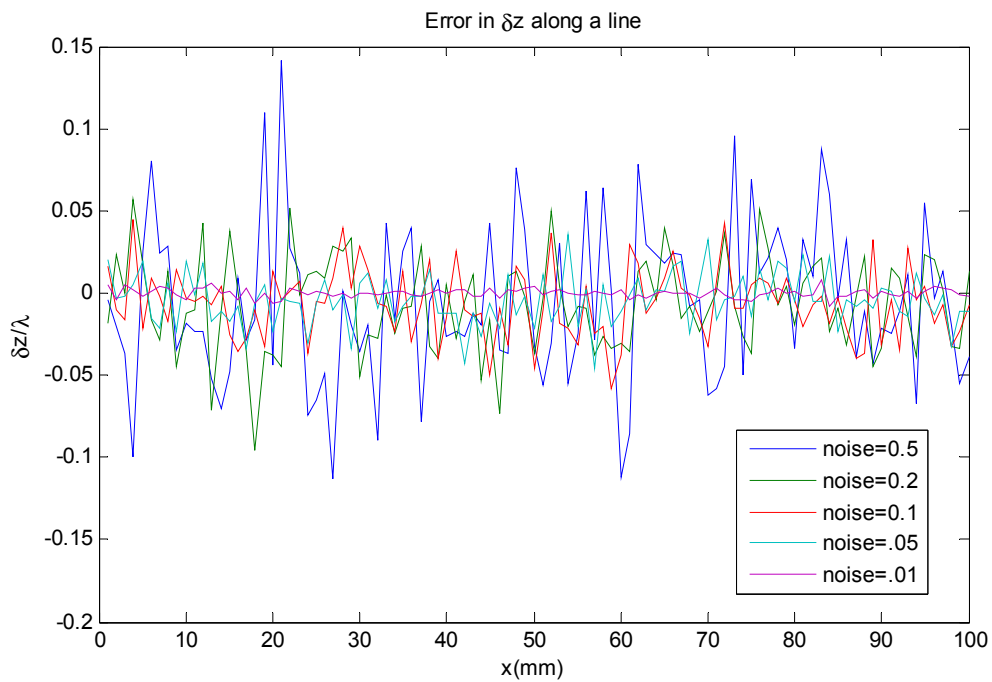


Figure 6-15 Error in Calculated δz along a Sample Line

Figure 6-16 shows the variation in error as a function of the applied noise in the MATLAB simulation, based on the observed noise in the experimental apparatus for realistic levels of added

noise. The measured change in thickness is accurate to better than $\pm 0.001p_e$ or $0.3\mu\text{m}$ for the moiré grid used in the experimental equipment.

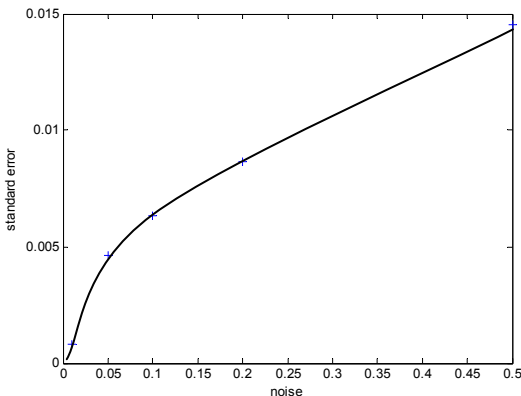


Figure 6-16 Variation in Measurement Error as a Function of Noise

6.1.8 Unwrapping VARTM data

Typical moiré images from infusion of the plain weave and CMF materials are shown in Figure 6-17 below.

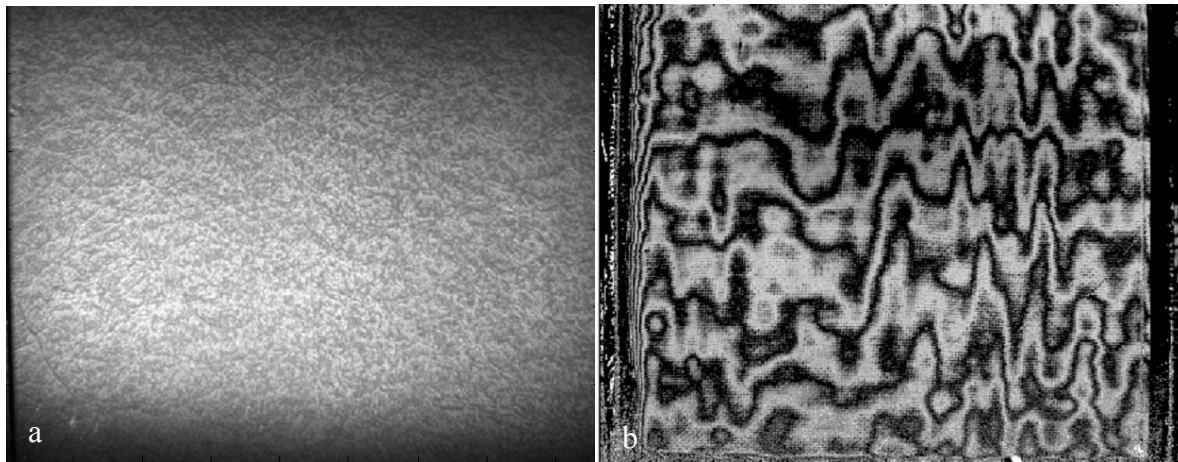


Figure 6-17 Moiré Images of Continuous Filament Mat(a) and Plain Weave Fabric(b)

The experimental VARTM data were obtained from 1-D flow experiments, which allowed for a simple choice of data sets. The thickness change parallel to the flow front in a 1-D flow is

approximately constant, and therefore, for each image a line of pixels parallel to the flow front was taken as the data set. The statistical analysis was then completed for each line, and the change in thickness recorded. Figure 6-18 shows the results of this analysis at three times during the process. One of the most important results found here was that the change in thickness at the flow front (expected to be of the order of $100\mu\text{m}$) was significantly smaller.

VARTM thickness Profile During Infusion

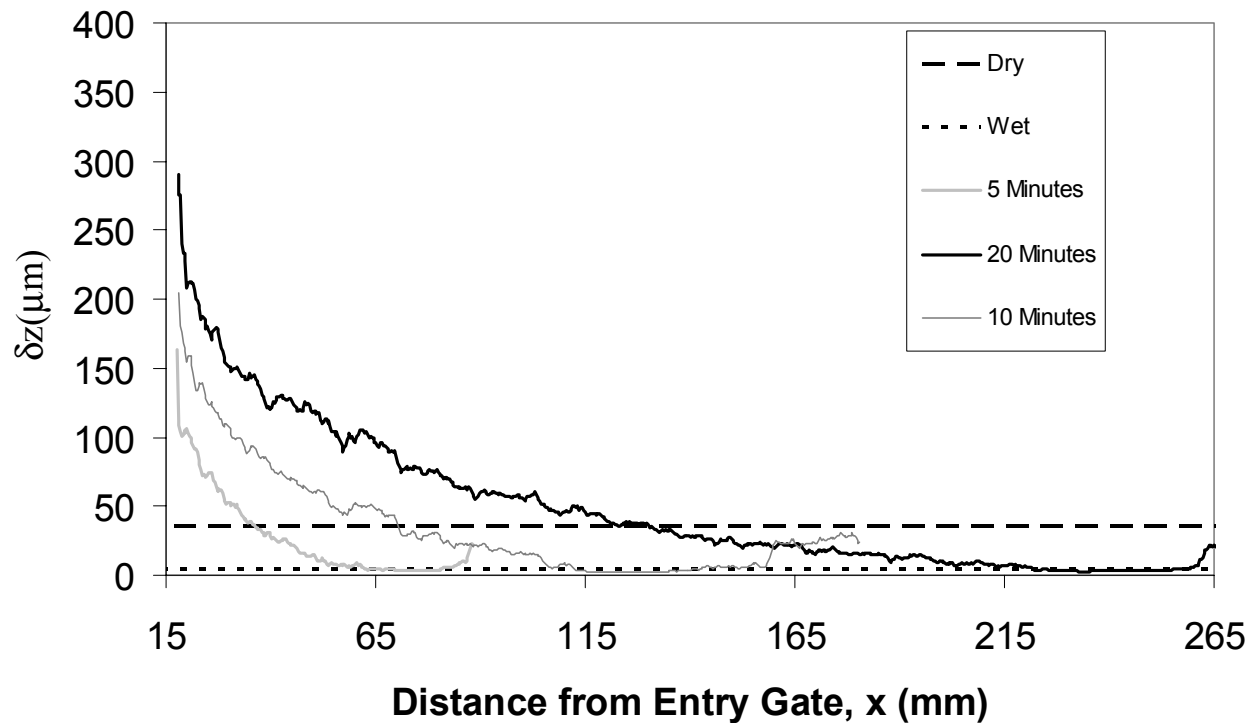


Figure 6-18 Plot of Measured Thickness Change in Preform during VARTM Processing

6.1.9 Effectiveness of the Statistical Technique

The technique described was developed to analyze data from a particular type of experiment in which a surface with an initially high profile is deformed in a consistent manner, and data needs to

be collected during the evolution of the process. The technique has been successfully applied to VARTM to observe the evolution of the process and to gain additional insights into the models which may be appropriate for the process. The technique is also adaptable to other processes with similar problems in 3-D surface measurement. For example, surfaces which do not have distinct surface features and which therefore cannot be easily measured by image correlation, (and assuming that application of a speckle pattern is undesirable) can be monitored using this technique. In addition where the environment is noisy (due to vibration, the difficulties in creating an effective black-out etc.) the use of statistics in the calculation helps eliminate most of the noise.

The major advantage of the algorithm is that it is extremely robust computationally as it does not rely at any point on the computation identification of the fringe peaks and troughs, a task which is very complex for noisy data. Indeed the technique can work in the absence of observable fringes.

6.2 Optical Measurement of Preform Saturation

To measure preform saturation we need to be able to calculate the amount of resin within a small region of the preform. For opaque materials (e.g. carbon fiber) we would need to use some form of penetrating radiation to measure the saturation, however, with glass fibers we have a much simpler option. If we pass light through the preform, the individual fibers will scatter the light, and, provided the preform is thick enough, the effect will be uniform. This scattering attenuates the light intensity transmitted by the preform. If we then infiltrate the preform using a fluid with a refractive index which closely matches that of the glass fibers, the degree of scattering, and hence attenuation, is reduced. We can therefore use the intensity of transmitted light to directly measure

the number of fiber interfaces wetted by the resin in the light path, which is directly proportional to the tow saturation.

6.2.1 Basic Model

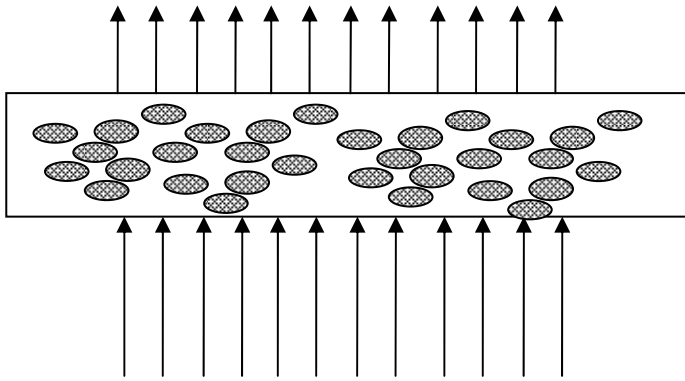


Figure 6-19 Schematic of Light Path through Fiber Preform

A model for the attenuation is proposed based on the following assumptions:

- 1 The light received by the camera is attenuated by dry fibers between the light source and detector.
- 2 The field of view is sufficient to average any effects of non random distribution of fibers.
- 3 The weave style (i.e. morphology of fibers) does not significantly affect attenuation.

The light intensity detected by the camera should be:

$$I = B + I_0 A^n \quad (6.14)$$

where B is the background intensity (i.e. intensity when no light is transmitted), A is the attenuation factor, n is the number of fiber interfaces in the light path, and I_0 is the light intensity measured with no fiber interfaces in the light path.

If we consider two fabrics (7500 style plain weave glass, and 1581 style 5 harness satin glass) both formed from the same type of fibers (E-glass fibers with a diameter between 8.89 μm -10.12 μm), the average number of interfaces in the light path will be proportional to the mass of fibers per unit area in the light path. If we imagine a small circular area of radius R , each fiber crossing the area contributes a mass $\frac{\pi d^2 R \rho}{2}$ to the aerial weight (w). The areal weight is therefore given as

$$w = \frac{Nd^2 \rho}{2R} \quad (6.15)$$

where N is the number of fibers crossing the area. Each fiber crossing the area adds two interfaces over a portion of the area $\frac{2d}{\pi R}$. The average number of interfaces at any point in the area is therefore $\frac{N4d}{\pi R}$ from which the relationship between n and w is obtained as

$$n = w \frac{8}{\pi d \rho} = \frac{w}{w_0} \quad (6.16)$$

This simplified analysis neglects some effects which will alter the value of w_0 but should not affect the linearity of the relationship. We can check that the weave style has a negligible effect on the

attenuation by comparing the light attenuation as a function of areal weight of fiber for two different weave styles. Expressing Eqn (6.14) in decibels gives

$$10 \log_{10} \left(\frac{I-B}{I_0} \right) = 10 \log_{10} \left(A^{\frac{w}{w_0}} \right) = w 10 \log_{10} \left(A^{\frac{1}{w_0}} \right) \quad (6.17)$$

We can see that we expect the areal weight to be proportional to the attenuation. In Figure 6-20 the light attenuation due to two weave styles of glass fabric (7500 and 1581) are shown. Both weave styles use the same type of glass fiber (E-Glass with a fiber diameter of 9-10 μ m) and therefore should have the same attenuation factor. We can then plot the attenuation in decibels

$10 \log_{10} \left(\frac{I-B}{I_0} \right)$ against w and calculate the attenuation factor $10 \log_{10} \left(A^{\frac{1}{w_0}} \right) = 0.015$ dB for w in gm^{-2} . The linearity of this graph, and the fact that the attenuation factor is almost exactly the same validates the assumptions made about the effect of weave style.

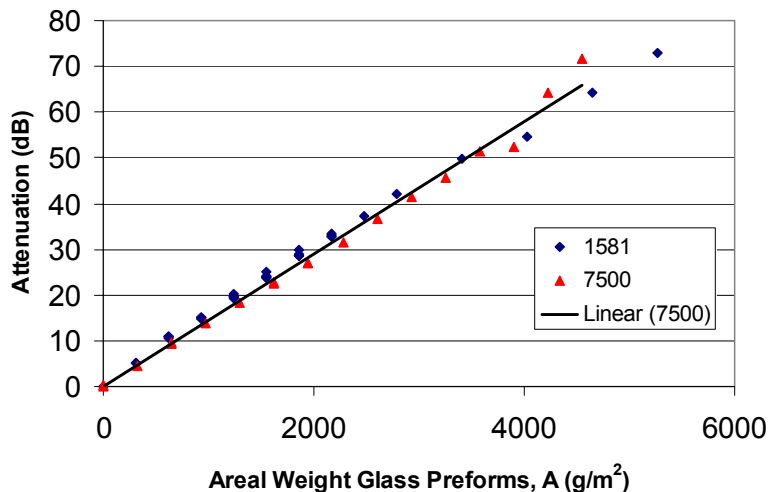


Figure 6-20 Light Attenuation vs Areal Weight of Glass Fibers in Preform

6.2.2 Saturation

For saturation measurement we assume that our total attenuation is due to 3 factors: resin in the intertow region, unsaturated fiber and saturated fiber, acting in series. Each region attenuates the transmitted light by a factor proportional to the areal weight of material in the light path. If we define a tow saturation coefficient V_{sat} then the areal weight of the unsaturated and saturated fiber will be $w_s = wV_{sat}$ and $w_u = w(1 - V_{sat})$ respectively. For each material we can calculate an effective thickness of material in the light path

$$\hat{h} = \frac{w}{\rho} \quad (6.18)$$

$$I - B = I_0 A_u^{h_u} A_s^{h_s} A_r^{h_r} \quad (6.19)$$

Assuming each material attenuates in proportion to the amount of material in the light path, the proportions of the attenuators can be

calculated as a function of tow saturation

$$\begin{aligned} \frac{h_r}{h} &= 1 - \frac{V_f}{V_{flow}} \\ \frac{h_s}{h} &= V_{sat} \left(1 - \frac{h_r}{h} \right) = \frac{V_{sat} V_f}{V_{flow}} \\ \frac{h_u}{h} &= 1 - \frac{h_s}{h} - \frac{h_r}{h} = \frac{(1 - V_{sat}) V_f}{V_{flow}} \end{aligned} \quad (6.20)$$

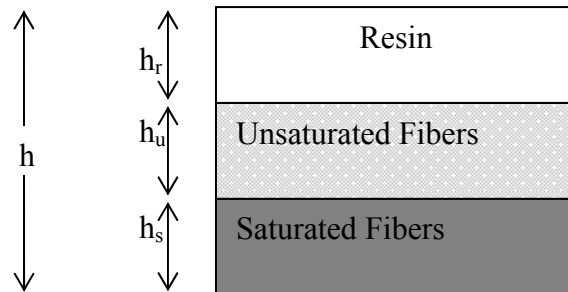


Figure 6-21 Series Model for Light Attenuation

From which

$$\begin{aligned}
 I - B &= I_0 \left(A_u^{(1-V_{sat})V_f} A_s^{V_{sat}V_f} A_r^{V_{flow}-V_f} \right)^{h/V_{flow}} \\
 &= I_0 K_0^{V_{sat}} K_1 \\
 K_0 &= \left(\frac{A_s}{A_u} \right)^{\frac{V_{sat}hV_f}{V_{flow}}} \\
 K_1 &= \left(A_u^{V_f} A_r^{V_{flow}-V_f} \right)^{h/V_{flow}}
 \end{aligned} \tag{6.21}$$

and we can therefore calculate V_{sat} as

$$V_{sat} = \frac{\ln(I - B) - \ln(I_0 K_1)}{\ln K_0} \tag{6.22}$$

6.3 Saturation Measurements

Saturation profiles

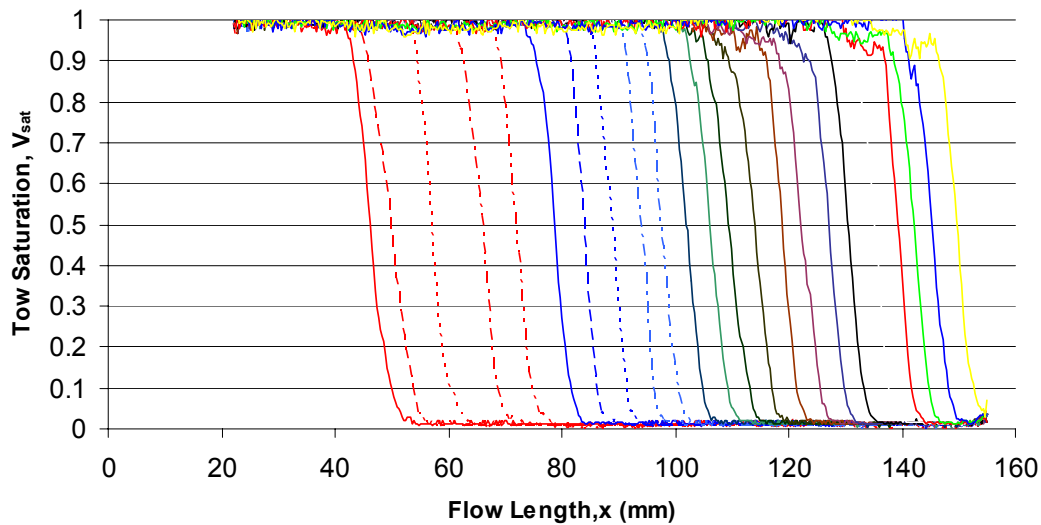


Figure 6-22 Saturation Measurements on Plain Weave Glass.

In the saturation measurement for plain weave glass a 10mm long unsaturated region develops and is consistently maintained across the entire flow.

6.4 Moiré Flow Experiments

For the moiré flow experiments the same procedure was used for both the plain weave and the continuous filament mat. A 100mm square preform was prepared and laid on the aluminum tool. The tool was designed with channels cut at each end to accommodate an expanded steel spring, and with a resin inlet and vent drilled from the edge of the plate to intersect the resin channel. The preform was then covered with a sheet of Kapton bagging film sealed around the edge of the plate with a vacuum sealant tape.

The preform was then evacuated using an oil filled vacuum pump, and held at 29.7inHg. The vacuum seal was then checked and where necessary repaired to ensure that with the system isolated from the vacuum pump a leakage rate of no more than 1/30 inHg/minute was observed on a bourdon type vacuum gage. Once the vacuum bag was satisfactorily sealed, the vacuum bag surface was painted with a titanium dioxide latex paint.

The preform was then mounted on the shadow moiré apparatus described in section 6.1.6 and a moiré grid at 3.94 lines/mm (100 lines/in) placed over the preform. The moiré apparatus software was then used to calibrate the moiré system by capturing a set of 300 images spaced over a vertical movement of the moiré grating of approximately 0.2mm. From the calibration results the effective pitch of the moiré system was calculated, along with the amplitude and background calibration constants.

Following the calibration test the vacuum was gradually released and then gradually reapplied. During this process a series of moiré images was taken and simultaneously the pressure inside the bag measured using a diaphragm pressure gage.

Following the vacuum tests the silicone oil was allowed to flow through the preform. Again moiré images were taken at regular intervals and these images were used to calculate the preform thickness during the infusion. Once the oil reached the exit gallery, the inlet gallery was closed, and from this point onward the preform started to recompact. Once it had fully recompact, a further set of calibration moiré images was taken.

6.4.1 Permeability model

We use a form of the Carman-Kozeny model for the macroscopic flow

$$K = k_0 \frac{(1 - V_f)^2}{V_f^3} \quad (6.23)$$

The fitting parameter k_0 is taken from published data sets for the performs.

Table 9 Permeability Constants for Carman-Kozeny Relationship

Material	k_0
CFM	$1.35 \times 10^{-10} \text{ m}^2$
PW	$2.19 \times 10^{-10} \text{ m}^2$ [66]

For the plain weave the value of k_0 is taken from measurements made by J Opperer [66] as shown in Figure 6-23.

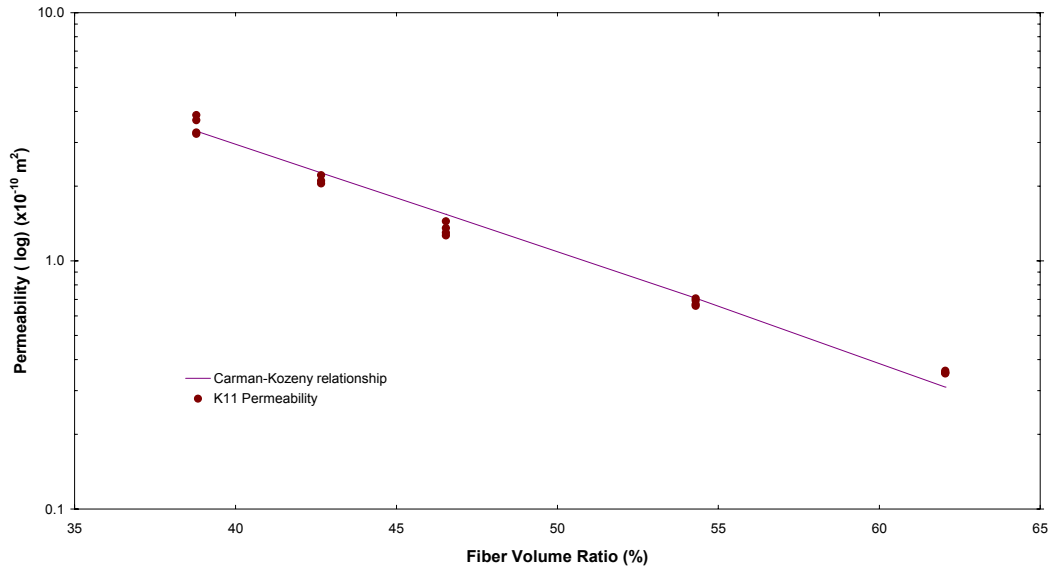


Figure 6-23 Permeability vs Fiber Volume Fraction (reproduced by permission J Opperer[66])

For the CFM, data from J Opperer’s thesis and from Gauvin [67] is combined in Figure 6-24

Continuous Filament Mat Permeability

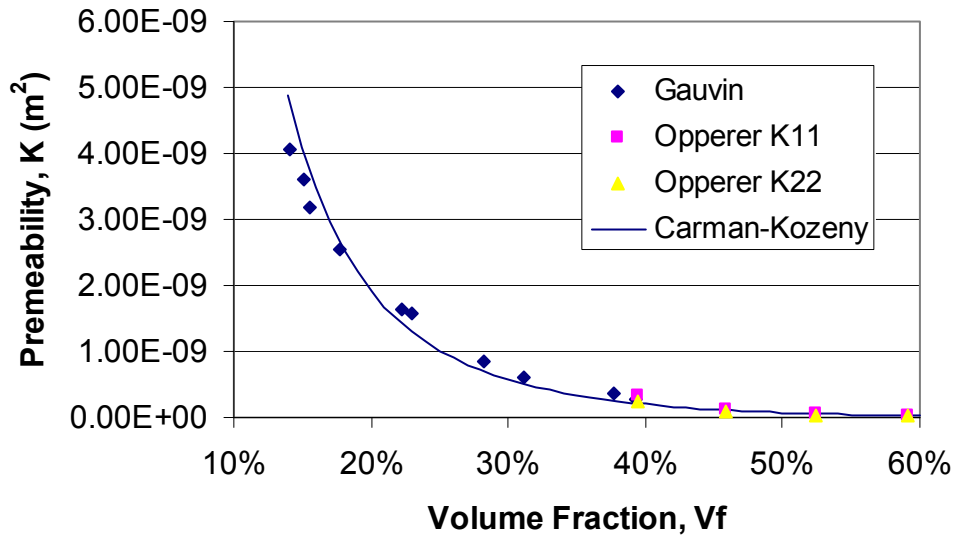


Figure 6-24 Carman-Kozeny Equation Fit for CFM (OCF8610).

For the microscopic permeability within the tows we use Kardos' [68, 69] expression for flow transverse to a bed of aligned fibers.

$$K_r = \frac{r_f^2 \left(\sqrt{\frac{0.8}{V_f}} - 1 \right)^3}{0.8 \frac{0.8}{V_f} + 1} \quad (6.24)$$

The plain weave glass uses ECG-37 tows which contain 816 9 μ m filaments per tow. In the fabrics the tows are 0.22mm in diameter, and the tow volume fraction V_{tow} is therefore 68%. From this the permeability of the tow is $6.37 \times 10^{-15} \text{ m}^2$. This leads to a saturation constant (see Eqn(5.32)) of

$$C_{sat} = \frac{4K_{tow}}{R^2 (1 - V_{tow})} = 6.66 \times 10^{-6} \quad (6.25)$$

6.5 Results

6.5.1 Plain Weave

For the plain weave fabric all the flow rate models from the simplest to most complex provide an adequate description of the fabric flow rates (see Figure 6-25), with the discrepancies between them being of the order of the possible errors in measured permeabilities. This is largely due to the relatively small variation in thickness observed in the preform during the infusion and compaction behavior.

The model provides good agreement for the saturation behavior at the flow front with the modeled saturation showing the development of an unsaturated region of a fixed size behind the flow front.

(This feature was also predicted well by Acheson's model [46], though he was not able to provide equivalent experimental data.)

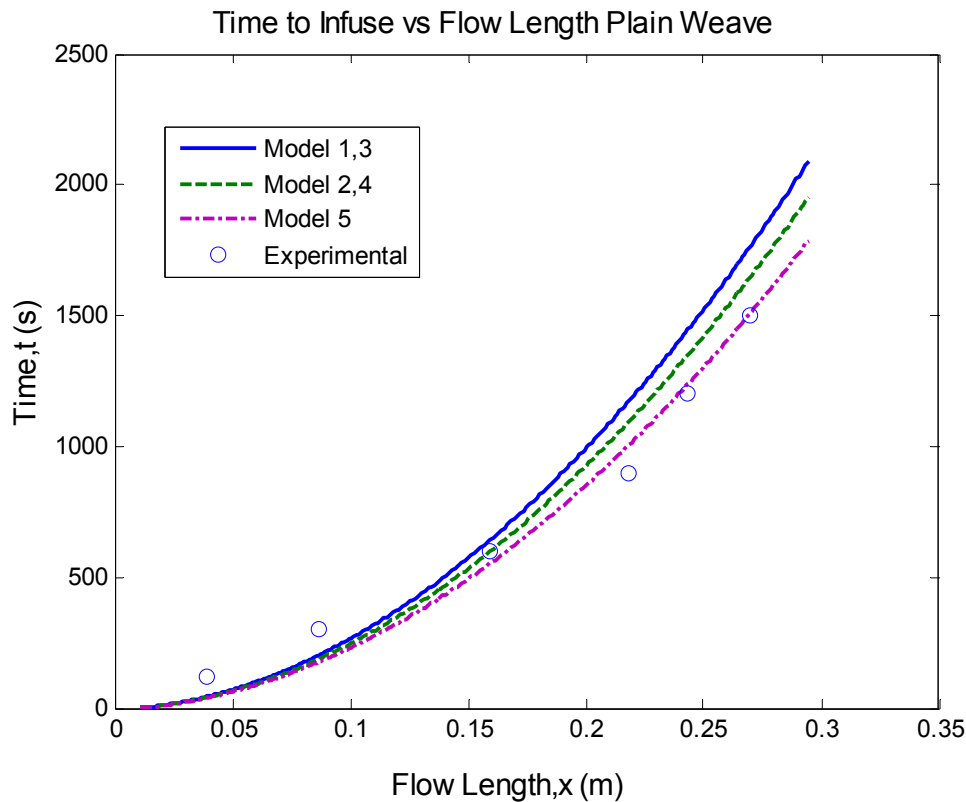


Figure 6-25 Location of Flow Front as a Function of Time Predicted by Using Various Thickness Models, and Measured Experimentally for Plain Weave Glass

In the modeling of the thickness profile however the models all predict a greater reduction in thickness after an initial development period than is found in the measured data. The primary cause for this appears to be the way in which the dry to wet transition is modeled, which in all cases assumes an instantaneous transition from the elastic behavior of the dry preform to the elastic behavior of the wet preform. Typically the models predict a thickness reduction of 0.2mm and the

observed reduction in thickness is of the order of 0.02mm.

6.5.2 Continuous Filament Mat

In the case of the CFM once again all the new models predict a slower infusion than was observed experimentally, and in the measured values it is notable that the preform thickness does not reduce on saturation. In the prediction of the flow front velocity, the best prediction comes from the hysteresis model with saturation effect which predicts the slowest reduction in thickness. To test alternatives an additional model was run in which the change of thickness due to preform saturation was reduced to zero, and the actual measured results lie between this modified model and the hysteresis and saturation models (see Figure 6-26)

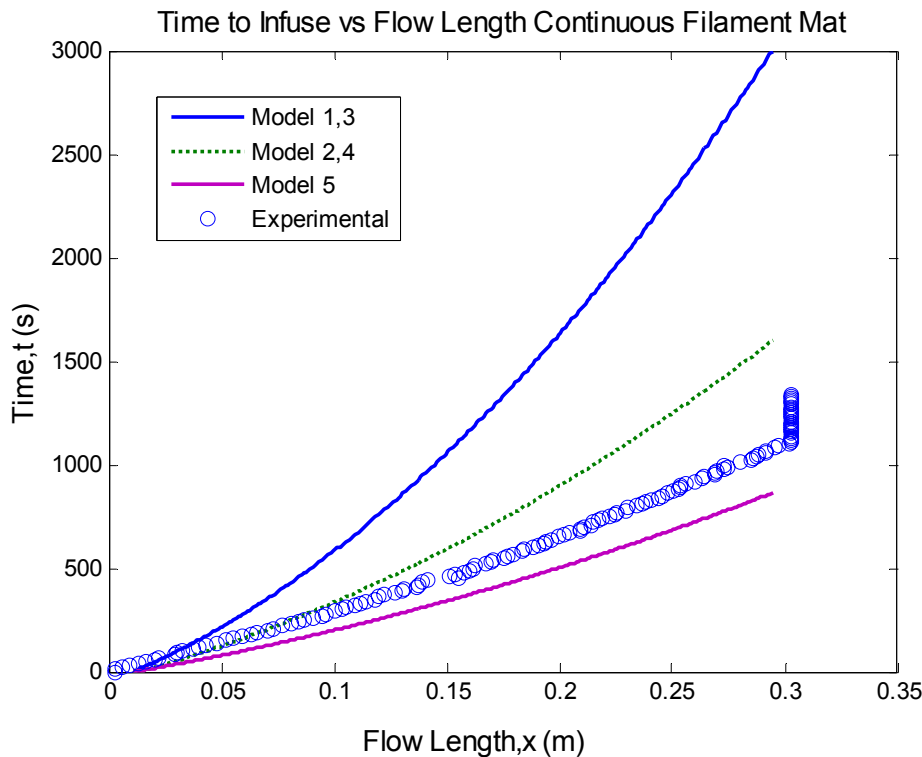


Figure 6-26 Location of Flow Front as a Function of Time Predicted by Using Various Thickness Models, and Measured Experimentally for Continuous Filament Mat

6.5.3 Thickness Change Discrepancy

In both cases the model predicts a greater reduction in thickness on saturation than is observed from the shadow moiré data. This is due to a feature of preform compaction, for which no experimental technique has yet been developed to measure. The key issue is in the way in which the static preform under a fixed compaction load responds to a change in saturation. This behavior is likely to be time dependent, and as the stability of the preform is controlled by the movement of frictional interfaces there may be an initial activation before which no movement takes place. Figure 6-27 shows the changes in thickness profile for the plain weave material, with all the traces modified to have the same minimum thickness. These all show good agreement with the actual data, indicating the effect of pressure on the thickness is adequately modeled in this case, but the effect of saturation (which controls the minimum thickness) is not.

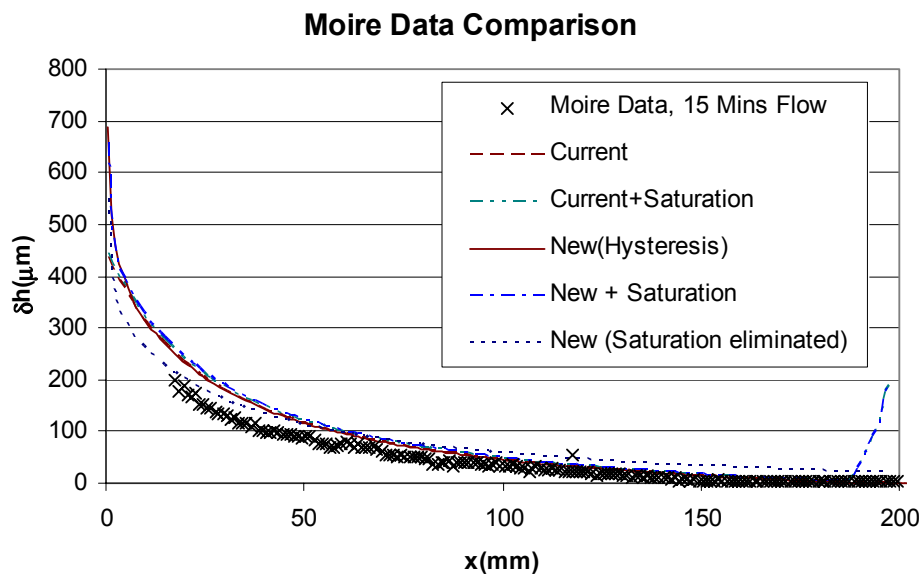


Figure 6-27 Comparison of Thickness Changes to Model Plain Weave

For the CFM material no change in thickness on saturation is observed at all and the thickness after saturation increases monotonically in response to the reduction in compaction pressure (Figure 6-28).

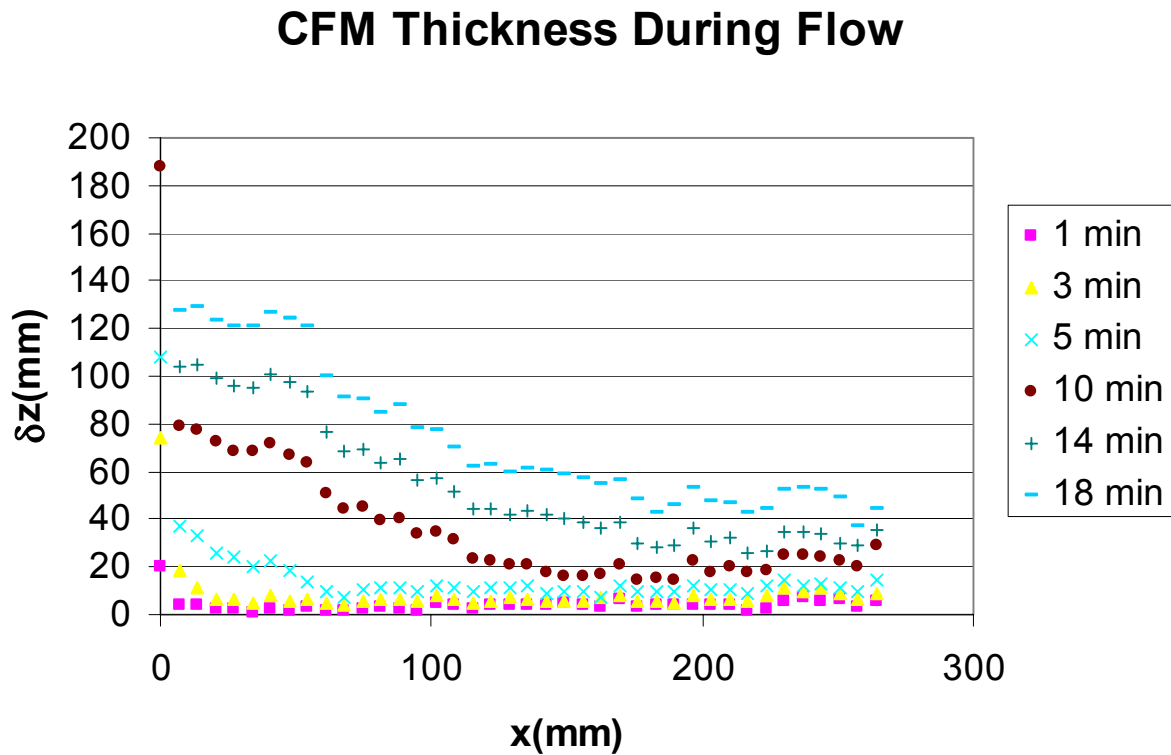


Figure 6-28 Thickness Profiles at Various Times During Infusion of Continuous Filament Mat, Measured by Shadow Moiré.

7 Summary, Conclusions, and Recommendations for Future Work

7.1 *Preform Compaction*

Interpolated models were proposed to describe the behavior of the preform under through thickness compression. These models describe the way the preform responds to reloading after partial unloading and to unloading after partial loading, within an overall envelope of possible behaviors for compaction to a defined maximum pressure. For VARTM this maximum pressure is 101KPa or 1 atmosphere. The models provide a good description of the response of the preform to changes in pressure, and work equally well for wet and dry preforms. The models do not however fully account for the response of the preform to changes in saturation.

7.2 *VARTM Flow Modeling*

Modifications to the current three dimensional continuity equation for dual scale porous flow in VARTM preforms were proposed, and subsequently used in the development of a one dimensional control volume finite element model of the VARTM process. This non-linear model includes the different proposed preform compaction models, and can be used to predict the preform thickness, saturation, and the resin flow rate. Predictions made by the model indicate that while the current state of the art models will provide acceptable results for some materials (including the plain weave fabric studied in this thesis) it is inadequate for other materials, (such as the continuous filament mat studied here). The results of the models also show that the model developed here for the effect of changes in saturation on preform thickness is not sufficient, and a more complex model for this behavior is required.

7.2.1 Experimental Methods

The shadow moiré system built as a part of this thesis allowed the full field measurement of the VARTM preform thickness during infusion and compaction of the preform. These measurements highlighted areas where improvements in the VARTM flow models were required. The statistical data analysis method developed for the shadow moiré system represents a novel approach to the problem and allowed automated calculation of the surface profiles. This method has wider applicability on other areas of surface profile measurement.

7.3 Conclusions

Modeling the VARTM process requires the solution of a complex set of coupled equations linking preform deformation, fluid flow, and pressure gradients. The models developed as part of this thesis provide additional insight into the specific areas of the preform deformation behavior which affect the VARTM flow, and suggest some interesting opportunities for additional research. The primary area where the model proposed in this thesis differs from other models is in the separate inclusion of the effect of saturation and pressure on the preform thickness.

In addition this research highlights where current models can provide adequate description of the infusion behavior, and where such models break down and cease to provide adequate descriptions. The extension of the current state of the art continuum mechanics description of fluid flow in liquid composite molding to properly include the effect of preform deformation as well as dual scales of flow, simplifies the future development of three dimensional models based on this work.

Development of experimental methods for the more detailed study of the VARTM process has also indicated that even in those cases where current models may provide adequate descriptions of the

infusion rate they will not properly describe the thickness profile of the infusion preform and will therefore not provide a good description of the post infusion compaction behavior. The experimental methods developed allowed accurate full field measurement of the preform surface profile during infusion, and largely automatic data reduction schemes. The statistical unwrapping method for shadow moiré represents an entirely novel approach to this problem, and while it is particularly suited to the problem of thickness measurement of VARTM preforms, it has wider applicability to other similar problems.

7.4 Recommendations for Future Work

The primary areas where future work is recommended are in the development of better models for the effect of changes in saturation on the preform thickness. This will need to include development of new experimental methods for both loading the preform and for consistently introducing a saturating fluid to the entire preform being studied. In addition, it would be valuable to study the effect of spatially varying loads on preform deformation behavior; however, additional experimental methods will be required for this.

The flow model developed in this thesis itself provides a good platform for testing the preform deformation models developed, however if a two-dimensional model for the preform thickness is required it may be necessary to extend the current model.

8 References

1. Daniel, I.M. and O. Ishai, *Engineering Mechanics Of Composite Materials*. 2nd ed. 2006, New York: Oxford University Press.
2. Matthews, F.L. and R.D. Rawlings, *Composite Materials, Engineering and Science*. 1994, London: Chapman and Hall.
3. Parnas R, S., *Liquid Composite Molding*. 2000 Munich: Hanser.
4. Pillai, K.M., *Governing equations for unsaturated flow through woven fiber mats. Part 1. Isothermal flows*. Composites Part a-Applied Science and Manufacturing, 2002. **33**(7): p. 1007-1019.
5. Williams, C., J. Summerscales, and S. Grove, *Resin infusion under flexible tooling (RIFT): A review*. Composites Part a-Applied Science and Manufacturing, 1996. **27**(7): p. 517-524.
6. Muskat, I.E., *Method Of Molding*. 1950, Marco Chemicals Inc: United Stated.
7. *Code of Federal Regulations: Occupational Health and Safety Standards*. 1997, OSHA.
8. Juska, T.D., H.B. Dexter, and W.H.I. Seemann. *Pushing the limits of VARTM*. in *Proceedings of the 1998 43rd International SAMPE Symposium and Exhibition. Part 1 (of 2), May 31-Jun 4 1998*. 1998. Anaheim, CA, USA: SAMPE, Covina, CA, USA.
9. Seref Aksu, S.C., Craig Gardiner and Matthew Gudze, *Hull Material Selection for Replacement Patrol Boats-An Overview*, M.P. Division and A.a.M.R. Laboratory, Editors. 2002, Defence Science and Technology Organisation (Australia).
10. Kruckenberg, T. and R. Paton, *Resin Transfer Molding for Aerospace Structures*. 1998, Netherlands Kluwer Academic.
11. Darcy, H., *Les Fontaines Publiques de la Ville de Dijon*, V. Dalmont, Editor. 1985, Corps Imperiaux de Ponts et Chaussees, et des mines: Paris.
12. Carman, P.C., *Fluid Flow Through Granular Beds*. Transactions of the Institute of Chemical Engineers, 1937. **15**: p. 150-166.
13. Slichter, Ninetheeth annual report US geological survey, 1897-8. **2**: p. 305.

14. Terzaghi, *Determination of permeability of clay*. Eng News Record, 1925. **95**(22): p. 832-836.
15. Gray, W., et al., *Mathematical Tools for Changing Spatial Scales in the Analysis of Physical Sciences*. 1993, Boca Raton: CRC Press.
16. Gutowski, T.G., *Advanced Composites Manufacturing*. 1997, New York: John Wiley and Sons.
17. Gutowski, T.G., T. Morigaki, and Z. Cai, *The Consolidation of Laminate Composites*. Journal of Composite Materials, 1987. **21**(2): p. 172-188.
18. Advani, S.G. and M.E. Sozer, *Process Modeling in Composites Manufacturing*. 2002, New York: Marcel Dekker.
19. Um, M.K. and S.K. Lee, *A study on the determination of in-plane permeability of fiber preforms*. Polymer Composites, 1999. **20**(6): p. 771-779.
20. Bruschke, M.V. and S.G. Advani, *A Finite-Element Control Volume Approach to Mold Filling in Anisotropic Porous-Media*. Polymer Composites, 1990. **11**(6): p. 398-405.
21. Lam, R.C. and J.L. Kardos, *The Permeability and Compressibility of Aligned and Cross-Plied Carbon-Fiber Beds during Processing of Composites*. Polymer Engineering and Science, 1991. **31**(14): p. 1064-1070.
22. Kim, S.K., et al., *Determination of in-plane permeability of fiber preforms by the gas flow method using pressure measurements*. Polymer Composites, 2003. **24**(1): p. 34-44.
23. Kim, S.K., J.G. Opperer, and I.M. Daniel, *Gas flow method for detecting local preform defects by inverse estimation of space-varying permeability*. Journal of Composite Materials, 2003. **37**(15): p. 1367-1383.
24. Chen, B.X., E.J. Lang, and T.W. Chou, *Experimental and theoretical studies of fabric compaction behavior in resin transfer molding*. Materials Science and Engineering a-Structural Materials Properties Microstructure and Processing, 2001. **317**(1-2): p. 188-196.
25. Chen, B.X. and T.W. Chou, *Compaction of woven-fabric preforms in liquid composite molding processes: single-layer deformation*. Composites Science and Technology, 1999. **59**(10): p. 1519-1526.

26. Robitaille, F. and R. Gauvin, *Compaction of textile reinforcements for composites manufacturing. I: Review of experimental results*. Polymer Composites, 1998. **19**(2): p. 198-216.
27. Van Wyk, C., *Note on the Compressibility of Wool*. Journal of the Textile Institute, 1946. **37**: p. T285-T292.
28. Robitaille, F. and R. Gauvin, *Compaction of textile reinforcements for composites manufacturing. II: Compaction and relaxation of dry and H₂O-saturated woven reinforcements*. Polymer Composites, 1998. **19**(5): p. 543-557.
29. Robitaille, F. and R. Gauvin, *Compaction of textile reinforcements for composites manufacturing. III. Reorganization of the fiber network*. Polymer Composites, 1999. **20**(1): p. 48-61.
30. Bickerton, S. and M.Z. Abdullah, *Modeling and evaluation of the filling stage of injection/compression moulding*. Composites Science and Technology, 2003. **63**(10): p. 1359-1375.
31. Bickerton, S. and S.G. Advani, *Experimental investigation and flow visualization of the resin-transfer mold-filling process in a non-planar geometry*. Composites Science and Technology, 1997. **57**(1): p. 23-33.
32. Bickerton, S. and S.G. Advani, *Characterization and modeling of race-tracking in liquid composite molding processes*. Composites Science and Technology, 1999. **59**(15): p. 2215-2229.
33. Bickerton, S., et al., *Experimental analysis and numerical modeling of flow channel effects in resin transfer molding*. Polymer Composites, 2000. **21**(1): p. 134-153.
34. Bickerton, S., M.J. Buntain, and A.A. Somashekar, *The viscoelastic compression behavior of liquid composite molding preforms*. Composites Part a-Applied Science and Manufacturing, 2003. **34**(5): p. 431-444.
35. Bickerton, S., et al., *Investigation of draping and its effects on the mold filling process during manufacturing of a compound curved composite part*. Composites Part a-Applied Science and Manufacturing, 1997. **28**(9-10): p. 801-816.
36. Dunlop, J.I., *Characterizing Compression Properties of Fiber Masses*. Journal of the Textile Institute, 1974. **65**(10): p. 532-536.
37. Dunlop, J.I., *The Dynamic Bulk Modulus of Fiber Masses*. Journal of the Textile Institute, 1981. **72**(4): p. 154-161.

38. Beil, N.B. and W.W. Roberts, *Modeling and computer simulation of the compressional Behavior of fiber assemblies - Part II: Hysteresis, crimp, and orientation effects*. Textile Research Journal, 2002. **72**(5): p. 375-382.
39. Beil, N.B. and W.W. Roberts, *Modeling and computer simulation of the compressional behavior of fiber assemblies - I: Comparison to van Wyk's theory*. Textile Research Journal, 2002. **72**(4): p. 341-351.
40. Kuentzer, N., et al., *Permeability characterization of dual scale fibrous porous media*. Composites Part a-Applied Science and Manufacturing, 2006. **37**(11): p. 2057-2068.
41. Zhou, F.P., et al., *Analytic characterization of the permeability of dual-scale fibrous porous media*. Composites Science and Technology, 2006. **66**(15): p. 2795-2803.
42. Kelly, P.A., R. Umer, and S. Bickerton, *Viscoelastic response of dry and wet fibrous materials during infusion processes*. Composites Part a-Applied Science and Manufacturing, 2006. **37**(6): p. 868-873.
43. Pillai, K.M., *Modeling the unsaturated flow in liquid composite molding processes: A review and some thoughts*. Journal of Composite Materials, 2004. **38**(23): p. 2097-2118.
44. Pillai, K.A. and M.S. Munagavalasa, *Governing equations for unsaturated flow through woven fiber mats. Part 2. Non-isothermal reactive flows*. Composites Part a-Applied Science and Manufacturing, 2004. **35**(4): p. 403-415.
45. Patankar , S., *Numerical Heat Transfer and Fluid Flow*. 1980: Taylor and Francis.
46. Acheson, J.A., P. Simacek, and S.G. Advani, *The implications of fiber compaction and saturation on fully coupled VARTM simulation*. Composites Part A: Applied Science and Manufacturing, 2004. **35**(2): p. 159-169.
47. Sciammarella, C.A., *The Moire Method - a Review*. Experimental Mechanics, 1982. **22**(11): p. 418-433.
48. Mulot, M., *Application of the moire to the study of mica deformations*. Revue D'Optique, 1925. **4**: p. 252-259.
49. Takasaki, H., *Moire Topography*. Applied Optics, 1970. **9**(6): p. 1467-&.
50. Meadows, D.M., W.O. Johnson, and J.B. Allen, *Generation of Surface Contours by Moire Patterns*. Applied Optics, 1970. **9**(4): p. 942-&.

51. Sciammar.Ca, *Techniques of Fringe Interpolation in Moire Patterns*. Experimental Mechanics, 1967. **7**(11): p. A19-&.
52. Mauvoisin, G., F. Bremand, and A. Lagarde, *3-Dimensional Shape Reconstruction by Phase-Shifting Shadow Moire*. Applied Optics, 1994. **33**(11): p. 2163-2169.
53. Yoshizawa, T. and T. Tomisawa, *Shadow Moire Topography by Means of the Phase-Shift Method*. Optical Engineering, 1993. **32**(7): p. 1668-1674.
54. Harding, K.G. and L.H. Bieman. *High-speed moire contouring methods analysis*. in *Three-Dimensional Imaging, Optical Metrology, and Inspection IV*. 1998. Boston, MA, USA: SPIE.
55. Fujimoto, J., *Determination of the Vibrating Phase by a Time-Averaged Shadow Moire Method*. Applied Optics, 1982. **21**(23): p. 4373-4376.
56. Huntley, J.M. and H. Saldner, *Temporal Phase-Unwrapping Algorithm for Automated Interferogram Analysis*. Applied Optics, 1993. **32**(17): p. 3047-3052.
57. Joenathan, C., et al., *Nondestructive testing using temporal phase evaluation in speckle interferometry*. Experimental Mechanics, 2000. **40**(1): p. 106-111.
58. Joris, J.J., Dirck, and W.F. Decraemer *Automatic calibration method for phase shift shadow moiré interferometry*. Applied Optics, 1990. **29**(10): p. 1474-1476.
59. Ghiglia, D.C. and L.A. Romero, *Robust 2-Dimensional Weighted and Unweighted Phase Unwrapping That Uses Fast Transforms and Iterative Methods*. Journal of the Optical Society of America a-Optics Image Science and Vision, 1994. **11**(1): p. 107-117.
60. Canabal, H., J.A. Quiroga, and E. Bernabeu, *Improved phase-shifting method for automatic processing of moire deflectograms*. Applied Optics, 1998. **37**(26): p. 6227-6233.
61. Canabal, H., J.A. Quiroga, and E. Bernabeu, *Automatic processing in moire deflectometry by local fringe direction calculation*. Applied Optics, 1998. **37**(25): p. 5894-5901.
62. Kevin Harding, L.B., *High Speed Moire Countouring Methods Analysis*. SPIE 1998. **3520**: p. 27.
63. Sciammarella, C.A., *Overview of optical techniques that measure displacements: Murray lecture*. Experimental Mechanics, 2003. **43**(1): p. 1-19.

64. Sciammarella, C.A., L. Lamberti, and F.M. Sciammarella, *High-accuracy contouring using projection moire*. *Optical Engineering*, 2005. **44**(9): p. -.
65. Tiziani, H.J., et al., *Measurement and description of microstructures with consideration of material-specific characteristics*. *Technisches Messen*, 1999. **66**(11): p. 429-436.
66. Opperer, J., *Permeability Characterization and Quality Control of Reinforcement in Resin Transfer Molding by the Gas Flow Method*, in *Mechanical Engineering*. 2004, Northwestern University: Evanston.
67. Gauvin, R., et al., *Permeability measurement and flow simulation through fiber reinforcement*. *Polymer Composites*, 1996. **17**(1): p. 34-42.
68. Skartsis, L., J.L. Kardos, and B. Khomami, *Resin Flow through Fiber Beds during Composite Manufacturing Processes .1. Review of Newtonian Flow through Fiber Beds*. *Polymer Engineering and Science*, 1992. **32**(4): p. 221-230.
69. Skartsis, L., B. Khomami, and J.L. Kardos, *Resin Flow through Fiber Beds during Composite Manufacturing Processes .2. Numerical and Experimental Studies of Newtonian Flow through Ideal and Actual Fiber Beds*. *Polymer Engineering and Science*, 1992. **32**(4): p. 231-239.